QUANTUM TRANSPORT PHENOMENA OF TWO-DIMENSIONAL MESOSCOPIC STRUCTURES

Quantum Transport Phenomena Of Two-Dimensional Mesoscopic Structures

PhD Thesis

written by
Viktor Szaszkó-Bogár

Co-supervisor:
Dr. Péter Földi

Doctoral School of Physics
Department of Theoretical Physics
Faculty of Science and Informatics
University of Szeged
Szeged, Hungary

Co-supervisor:
Prof. Dr. François M. Peeters

Doctoraatschool
Departement Fysica
Faculteit Wetenschappen
Universiteit Antwerpen
Antwerpen, Belgium

Szeged, 2015

Contents

Part I

Part II

List of Figures

Part I

Introduction

Nowadays we can often hear terms as "Mesoscopic Systems", "Mesoscopic Physics", or "Mesoscopic World". The prefix "meso-" originates from the Greek word $\mu\epsilon\sigma o\zeta$ meaning "middle" or "intermediate". It occurs in various aspects of different sciences, e.g. in meteorology (mesosphere), in geology (mesozoic era) and also in physics of elementary particles (meson). Mesoscopic as an attribute appeared first in a paper by van Kampen [1] to characterize systems which are situated between the macroscopic and the microscopic world. According to our present knowledge, classical physics (quantum theory) can offer efficient tools for the description of phenomena in the macroscopic (microscopic) regime. The mesoscopic world exists on the (imaginary) borderline between quantum and classical physics. Although the precise definition of the size of the objects that can be called mesoscopic is difficult or even impossible, as a rule of thumb, systems the extension of which is expressed most conveniently in nanometers ("nanoscale systems") belong to this family.

Miniaturization, as a consequence of the continuous technological advances, determines the development in electronics industry even today, essentially in agreement with the famous Moore's law. At the beginning of microelectronics, transistors, diodes and digital integrated circuits which were typically made from semiconductor materials, emerged. Later on, nanoelectronics, nanotechnology and related disciplines have also appeared. The current study focuses on semiconductor nanostructures and their spin-dependent electron transport properties that have outstanding significance despite meaning only a small section of nanosciences. The physical behavior of these nanoscale objects is mainly determined by quantum mechanics, but thermal fluctuations, defects, etc., lead to the emergence of classical properties. The idea that the spin degree of freedom can be used as a source of information – that can be realized most probably in nanoscale systems – opened a new field of research, called *spintronics* or *spin electronics*.

Advances in spintronics are significant also in the past few years. The key question of this multidisciplinary field is how spin degrees of freedom can be manipulated in condensed matter systems. The most relevant spin-transformation mechanisms including spin-polarized transport, spin injection, spin relaxation, spin dephasing, spin-orbit fields, etc., are discussed in Ref. [2]. An important aspect of spintronic devices and applications

is their close relation to quantum mechanical information processing [3]. The first spintronic device that gained a wide interest is the spin-polarized field effect transistor (SFET) that was introduced in Ref. [4]. (It is also called Datta-Das spin field-effect transistor.)

Spintronics with semiconductors is currently developed along several different directions.

First, by considering hybrid structures that combine ferromagnetic metals with nonmagnetic semiconductors. A remarkable problem in this approach is the injection of a spin-polarized current from a magnetic metal into a semiconductor. At the time being, theoretical solutions have been proposed [5]. Spin injection and extraction through a tunnel contact has also been demonstrated in spin LEDs and magneto-optical experiments [6].

A different approach to semiconductor based spintronics relies on the fabrication of ferromagnetic semiconductors. Specifically, the material $Ga_{1-x}Mn_xAs$ (x is not larger than a few percent) has been discovered by the group of Ohno in 1996 [7]. They observed the possibility of controlling the ferromagnetic properties with a gate voltage, and also demonstrated large tunneling magnetoresistance (TMR) and tunneling anisotropic magnetoresistance (TAMR) effects.

The third way (to be studied also in the current work) exploits spin-polarized currents that are induced by spin-orbit effects like the spin Hall, Bychkov-Rashba, or Dresselhaus effects [8, 9, 10]. Considering e.g. the spin Hall effect (SHE), spin-orbit interactions deflect the currents of the spin up and spin down channels in opposite transverse directions, thereby inducing a transverse spin current, even in a nonmagnetic conductor. This could be used to create spin currents in structures composed of only nonmagnetic semiconductors.

In the last twenty years semiconductor nanostructures have proven to allow the realization of nearly ideal quantum systems. The development of semiconductor engineering has enabled to fabricate diverse nanostructures. Some of them is of importance from the viewpoint of both fundamental research and applications. These are *quantum wells*, *quantum wire* and *quantum dot* structures.

A quantum well can be realized using crystal- or layer by layer growth techniques [11], such as molecular-beam epitaxy (MBE) and vapor-phase epitaxy (VPE). In this kind of nanosystems, the energy bandgap is engineered to vary with position in a specified manner, leading to materials with unique electronic and optical properties [12, 13]. For instance, a multi-quantum-well (MQW) consists of ultrathin ($2 - 15\,\mathrm{nm}$) layers of GaAs alternating with thin ($20\,\mathrm{nm}$) layers of AlGaAs. The AlGaAs barrier regions can also be made ultrathin ($< 1\,\mathrm{nm}$), in which case the electrons in adjacent wells can readily couple to each other via quantum-mechanical tunneling and the discrete energy levels broaden

into miniature bands called minibands. The structure is then called a superlattice, because the minibands arise from a periodic structure the lattice constant of which is considerably larger than the natural atomic separation. Consequently, the energy minibands mean an additional "fine structure" of the energy-level diagram for electrons and holes.

More generally, quantum wells – in contrast to bulk materials – can be considered as two-dimensional objects in which quantization of motion of the electrons occurs in one direction, while they can propagate as free particles in the other two directions [14].

A semiconductor layer having the form of a thin channel surrounded by a material of wider bandgap is called a quantum wire. This type of nano-scaled system can be considered as a one-dimensional structure. Free movement of charge carriers is allowed along only one direction, while they are confined in the remaining two directions. The effective confinement potential is determined by the geometry of the quantum channel itself. Quantum wires can be fabricated by various techniques. One of them is the MBE-growth on prepatterned substrates, like the realization of quantum wires on a (100) GaAs substrate. A different method, called cleaved-edge overgrowth (CEO), was developed at the beginning of the 1990s at Bell Labs. It allows the fabrication of very high quality quantum wires and quantum dots [15]. The effects of a longitudinal periodic potential on a parabolic quantum wire defined in a two-dimensional electron gas with Rashba spin-orbit interaction were studied in Ref. [16].

As a special case, quantum wires can form closed loops that can serve as (spin) interference devices. Mesoscopic rings (quantum rings) with a small diameter ($d \approx 1\,\mu\mathrm{m}$) are intensely studied due to their ability to show various types of fundamental quantum mechanical phenomena, such as the Aharonov-Bohm (AB) effect [17, 18], when the wave function of a charged particle passing around a magnetic flux experiences a phase shift. The dual of this effect is called Aharonov-Casher (AC) phenomenon [19]. In this case a particle with magnetic moment acquires a phase shift in an electric field. It has already been demonstrated in different nanosystems [20, 21, 22]. Control of the spin geometric phase in semiconductor quantum rings has also been demonstrated [23, 24].

Nanocrystals, quantum boxes and quantum dots are semiconductor systems whose spatial extension usually ranges from $1\,\mathrm{nm}$ to $10\,\mathrm{nm}$. They can be fabricated from many different kinds of semiconductors and in many geometrical shapes (e.g., cubes and spheres). For example, a GaAs/AlGaAs heterostructure with a two-dimensional electron gas below the surface and a split-gate define a quantum dot. Negative voltages applied to the gate electrodes deplete the underlying electron gas such that electrons are localized on the island between the two central gate fingers [15]. The sizes of quantum dots, and thus the number of atoms they contain, can be varied over a broad range. The number of electrons

can be as small as just a few or as large as millions. In this structure, the electrons are narrowly confined in all three directions. The allowed energy levels are discrete and well separated so that the density of states is represented by a sequence of delta functions at the allowed energies. Quantum dots are also referred to as artificial atoms. The effects of spin-orbit coupling on the electronic structure of quantum dots is presented in Ref. [25].

The present dissertation consists of three main parts. The first one is the introductory part in which we summarize preliminary concepts of quantum mechanical electronic transport in mesoscopic systems. We focus on quantum interference phenomena and the Landauer-Büttiker formalism [26, 27, 28]. We also deal with basic principles of spin-obit interaction and related effects. The backbone of the dissertation is Parts II and III. They contain models, applied methods and the results we obtained during our investigation of the quantum transport phenomena of two-dimensional (2D) superlattices and certain loop geometries in the presence of stationary and oscillating Rashba-type spin-orbit interaction. Finally, our results are summarized in English, Flemish and in Hungarian.

Chapter 1

Transport in mesoscopic structures

During the 1980s, an important question arose, namely, what new effects emerge when the dimension of a small conductor is between microscopic and macroscopic sizes? One of these effects is the quantization of conductance meaning that Ohm's law does not hold for sufficiently small conductors.

An example of conductance quantization that is related to quantum point contacts (QPCs) is shown in Fig. 1.1. In this experiment, the conductance of the QPC is measured as a function of its (negative) gate voltage. Referring to the behavior shown in the inset, as the gate voltage gets below $\sim -0.5\,\mathrm{V},$ a sudden drop in the conductance is observed, indicating the full depletion of the 2-DEG directly underneath the gates and, thus, the formation of the QPC. As the gate voltage is made even more negative, a slower decrease of the conductance occurs and it is clear from the behavior in the main panel that it develops into a steplike behavior. In fact, the conductance in this figure is plotted in units of $2e^2/h$ and it is clear that each step in the conductance corresponds to a change by this amount. The h/e^2 is referred to as the von Klitzing constant [29]. This remarkable behavior was first observed, independently, by Wharam et al. [30] and van Wees et al. [31] and has been confirmed in numerous experiments [32].

The purpose of the current chapter is to recall the fundamental ideas and properties of semiconductor nanostructures and quantum transport effects.

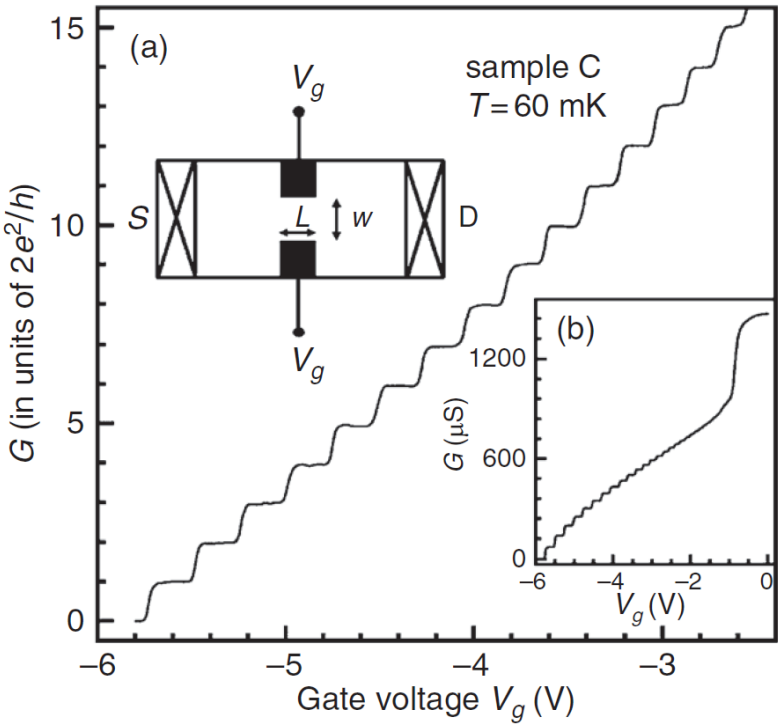

Figure 1.1: The conductance G of a QPC measured as function of the gate voltage V_g at low temperature. The quantum mechanical phenomenon is expressed by the steplike behavior of G. Adapted from Ref. [33].

1.1 Two-dimensional electron gas in semiconductor heterostructures

In this section we summarize some basic concepts related to two-dimensional electron gas systems. As an example, we discuss the gallium arsenide (GaAs) / aluminium gallium arsenide (AlGaAs) material system which provides a very high quality two-dimensional transport channel and has been widely used in artificial nanostructures [28]. These systems opened a new research area, namely, the physics of the electronic properties of two-dimensional structures.

In order to understand the importance of semiconductor heterostructures in mesoscopic systems, let us take a look at the band scheme of an AlGaAs and GaAs heterojunction shown in Fig. 1.2. As it is known, the n-type AlGaAs can be doped with donor impurities. As we can see, the Fermi energy E_F in the widegap AlGaAs layer is higher than in the narrowgap GaAs layer. Consequently electrons move away from the n-AlGaAs part of the sample leaving positively charged donors behind. Because of the positive excess charge, an electrostatic potential arises that causes the bands to bend as shown in Fig. 1.2. At equilibrium and in the absence of bias, the Fermi energy becomes constant in the whole semiconductor structure. However, the electron density is sharply peaked close to the GaAs–AlGaAs interface (where the Fermi energy is inside the conduction band). It is forming a thin conducting layer which is usually referred to as a two-dimensional electron gas (2-DEG).

The carrier mobility of semiconductor heterostructures can be considerably larger than that of the corresponding bulk semiconductor; this is achieved by a technique generally referred to as "modulation doping". Modulation-doped heterostructures are obtained by introducing n-type dopant impurities (e.g., Si) into the wide-band-gap AlGaAs at some distance from the interface (the undoped AlGaAs is called the spacer), whereas the narrow-band-gap material (GaAs) remains free from intentional doping, as shown in Fig. 1.2(a). Due to modulation doping [36], the mobile carriers in the heterostructure are spatially separated from their parent impurities [38], which leads to a reduction of scattering. Thus, high carrier mobilities can be obtained [34].

The charge carrier concentration in a 2-DEG generally ranges from $2 \cdot 10^{11}\,\mathrm{cm}^{-2}$ to $2 \cdot 10^{12}\,\mathrm{cm}^{-2}$ and can be depleted by applying a negative voltage on a metallic gate deposited on the surface. The practical importance of this structure lies in its use as a field effect transistor (FET).

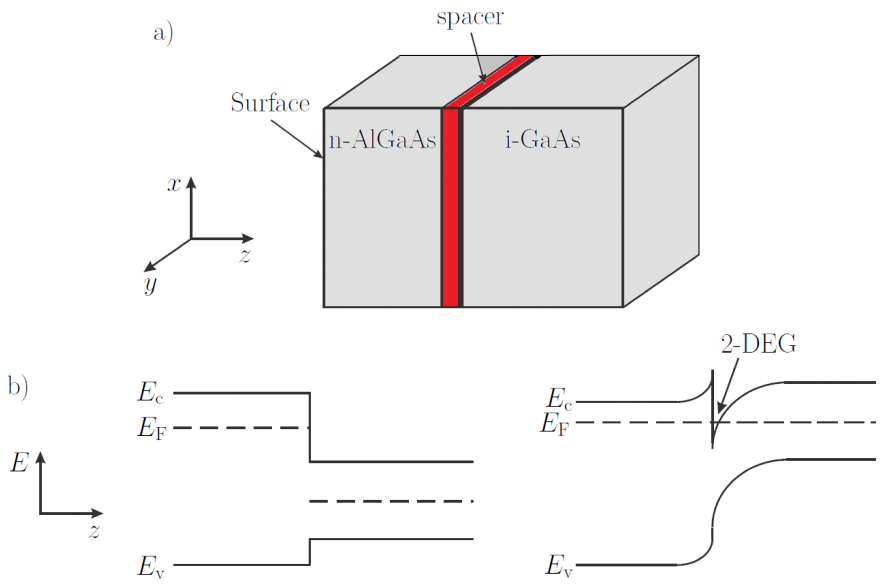

Figure 1.2: Conduction and valence band line-up at a junction between an n-type AlGaAs and intrinsic GaAs, (a) before and (b) after charge transfer has taken place. Note that this is a cross-sectional view [34, 35].

1.2 Effective mass approximation

The dispersion relation of Bloch electrons can be approximated by the quadratic expression of wavenumber vectors $\mathbf{k}$ close to the minima of the bands. In a crystal which has a cubic unit cell, if the minimum is located at $\mathbf{k}_0$, due to the high symmetry, we can write

$$\varepsilon_{\mathbf{k}} \approx \varepsilon_{\mathbf{k}_0} + A(\mathbf{k} - \mathbf{k}_0)^2, \tag{1.1}$$

where $\varepsilon_{\mathbf{k}}$ denotes the $\mathbf{k}$-dependent energy and the coefficient A equals $\frac{\hbar^2}{2m^*}$. As an interpretation, one can argue that in the dispersion relation of the Bloch electrons, instead of ordinary electron mass m_e, a modified "mass" m^* has appeared. m^* is called the *effective mass* [37], and it is given by

$$\frac{1}{m^*} = \frac{1}{\hbar^2}\frac{\partial^2 \varepsilon_{\mathbf{k}}}{\partial \mathbf{k}^2}. \tag{1.2}$$

The effective mass depends on the periodic potential of the crystal lattice.

In a more general case, the effective mass tensor should be introduced instead of the scalar effective mass (1.2):

$$\left(\frac{1}{m^*}\right)_{ij} = \frac{1}{\hbar^2}\frac{\partial^2 \varepsilon_{\mathbf{k}}}{\partial k_i \partial k_j}, \quad i,j = x,y,z. \tag{1.3}$$

Now we can write the electron energy in the following form

$$\varepsilon_{\mathbf{k}} \approx \varepsilon_{\mathbf{k}_0} + \frac{\hbar^2}{2} \sum_{ij} \left(\frac{1}{m^*} \right)_{ij} (k_i - k_{0i})(k_j - k_{0j}). \tag{1.4}$$

As it is known, there are several methods which can be used for the derivation of the effective-mass approximation. One of the possible ways is to use Wannier functions [38, 39]. However, considering our aims, a Schrödinger-like equation is more suitable.

Within the framework of the effective mass approximation, the dynamics of the electrons in the conduction band is governed by the following equation:

$$H_{eff}\Psi(\mathbf{r}) = \left[E_c + \frac{1}{2m^*}(i\hbar\nabla + e\mathbf{A})^2 + U(\mathbf{r}) \right] \Psi(\mathbf{r}) = E\Psi(\mathbf{r}), \tag{1.5}$$

where the conduction band edge is denoted by E_c and the potential term $U(\mathbf{r})$ appears owing to space-charges and confinement. When an external electromagnetic field interacts with the electronic system, one uses the transformation $i\hbar\nabla \rightarrow i\hbar\nabla + e\mathbf{A}$. It is called minimal or Peierls substitution [40] that has several different aspects in the theory of Bloch electrons as well as in more general quantum mechanical problems [41, 42].

Let us emphasize, that the effective mass m^* is distinct in different bands. Thus the relation (1.5) is valid inside a given band. The lattice potential does not appear explicitly in the effective Hamiltonian H_{eff}, its effect is manifested in the effective mass m^* which we will assume to be spatially independent. Any band discontinuity ΔE_c at the heterojunction is incorporated by letting E_c be position-dependent. According to these, Eq. (1.5) is usually referred to as the *single-band effective mass equation*.

1.3 Transverse modes and subband structure

Our aim is to understand the quantum mechanical behavior of electrons which are confined in a narrow channel. To this end, we consider a simple model of an ideal quantum channel with *transverse modes*. Such a rectangular conductor is shown schematically in Fig. 1.3 (a). We assume the horizontal length of the wire in x-direction to be very long compared to its cross-sectional area. The motion of charge carriers (in the present case, electrons) in a narrow quantum channel is described by the effective mass equation

$$\left[E_c + \frac{1}{2m^*}(i\hbar\nabla + e\mathbf{A}) + U(y) \right] \Psi(x,y) = E\Psi(x,y). \tag{1.6}$$

The solutions to Eq. (1.6) can be expressed in the form of plane waves (L: length of conductor over which the wavefunction is normalized)

$$\Psi(x,y) = \frac{1}{\sqrt{L}} \exp[ikx]\chi(y), \tag{1.7}$$

where the function $\chi(y)$ describes the *transverse mode*.

Let us consider the case of zero magnetic field ($\mathbf{B} = \mathbf{0}$, which is valid also for our results to be discussed in Parts II and III). The details of the confinement potential $U(y)$ has not been given yet. Obviously, for arbitrary $U(y)$ there are hardly any analytical solutions.

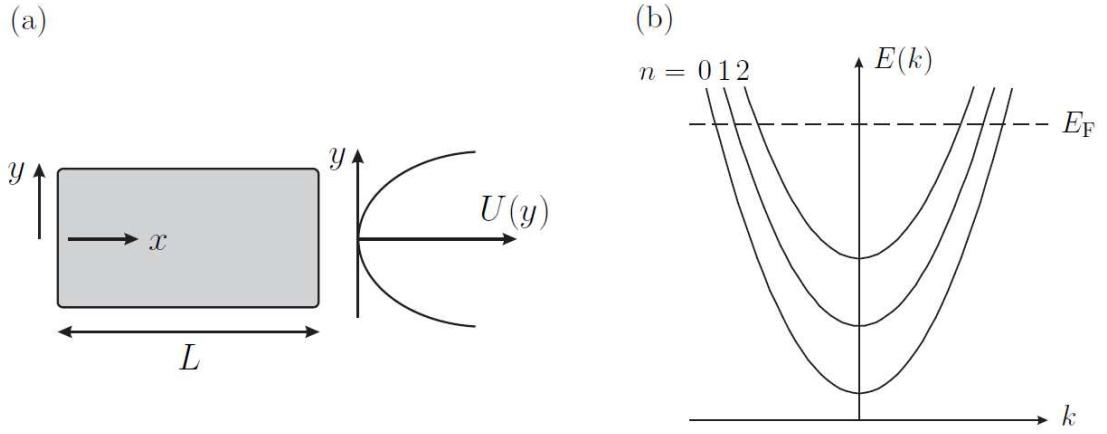

Figure 1.3: Panel (a) shows a rectangular conductor assumed to be uniform in the x-direction. It has a transverse confining potential $U(y)$. Panel (b): Dispersion relation, $E(k)$ for electric subbands arising from parabolic confinement. The different subbands are indexed by n [34].

However, we can find an adequate description of various physical problems [43, 44] if $U(y)$ can be approximated by a quadratic potential

$$U(y) = \frac{1}{2} m\omega_0^2 y^2. \tag{1.8}$$

In this case, the mode functions $\chi_{n,k}(y)$ and the corresponding eigenenergies $E(n,k)$ can be obtained using the theory of the quantum linear harmonic oscillator [45]. They are given by

$$\chi_{n,k}(y) = u_n(q) \quad \text{where} \quad q = y\sqrt{\frac{m\omega_0}{\hbar}}, \tag{1.9}$$

$$E(n,k) = E_c + \frac{\hbar^2 k^2}{2m} + \left(n + \frac{1}{2}\right)\hbar\omega_0, \quad n = 0, 1, 2, \cdots, \tag{1.10}$$

where

$$u_n(q) = \exp\left[-\frac{q^2}{2}\right] H_n(q), \tag{1.11}$$

with $H_n(q)$ being the nth Hermite polynomial [46], and different values of the integer n label the different subbands.

The most remarkable consequence of the subband structure is the lifting of the band edge energy by $\varepsilon_n = \left(n + \frac{1}{2}\right)\hbar\omega$. This effect is general, appears for any confining potential, although the values of ε_n obviously depend on the choice of $U(y)$. In the following we consider quasi one-dimensional samples, where no other transversal modes are assumed to be excited than the ground state ($n = 0$). This leads to a modification of the effective mass equation:

$$\left[E_s + \frac{1}{2m^*}(i\hbar\nabla + e\mathbf{A})^2 + U(x,y)\right]\Psi(x,y) = E\Psi(x,y), \tag{1.12}$$

where $E_s = E_c + \varepsilon_0$. This simplification is applied throughout the dissertation when discussing semiconductor nanostructures.

1.4 Ballistic electron transport

There are essentially two qualitatively different regimes of transport: diffusive (ohmic) and ballistic. We can determine which regime is relevant for a given sample by using certain characteristic lengths: the linear size of the sample, the mean free path, and the phase-relaxation length.

We consider a realistic condensed matter model which can include impurity effects, lattice vibrations (phonons) or additional 'collision' mechanisms that scatter the electron from one state to another thereby changing their momenta. The momentum relaxation time τ_m is related to the collision time τ_c by a relation of the form

$$\frac{1}{\tau_m} \propto \alpha_m \frac{1}{\tau_c}, \tag{1.13}$$

where the dimensionless coefficient α_m (its possible values are in the interval $[0, 1]$) denotes the 'effectiveness' of an individual collision in destroying momentum. Accordingly, we can provide the definition of the mean free path L_m: it is the distance that an electron travels before its initial momentum is destroyed. That is,

$$L_m = v_F \tau_m, \tag{1.14}$$

where $v_F = \hbar k_F/m$ is the Fermi velocity. L_m is usually referred to as the momentum relaxation length.

Analogously, we can define the phase-relaxation time (τ_φ) and length (L_φ) by

$$\frac{1}{\tau_\varphi} \propto \alpha_\varphi \frac{1}{\tau_c}, \tag{1.15}$$

where the factor α_φ denotes the effectiveness of an individual collision in destroying the phase. One way to visualize the destruction of phase is in terms of a thought experiment

involving interference [28]. Let us consider a device which can split a beam of electrons into two paths and then recombine them. Actually, it is an interferometer. In a perfect crystal the two arms would be identical resulting in constructive interference. By applying a magnetic field perpendicular to the plane containing the paths, one can change their relative phase thereby changing the interference from constructive to destructive (and vice versa). Now we take into account a real crystal in which some kind of scattering effects can arise due to impurities, defects, phonons etc. We would expect the interference amplitude to be reduced by a factor

$$\exp\left[-\frac{\tau_t}{\tau_\varphi}\right], \tag{1.16}$$

where τ_t is the transit time that the electron spends in the interferometer.

Now we can provide the relation between the phase-relaxation time (τ_φ) and the phase-relaxation length (L_φ). It can be written as

$$L_\varphi = v_F \tau_\varphi. \tag{1.17}$$

This is valid if the phase-relaxation time is of the same order or shorter than the momentum relaxation time, that is, if $\tau_\varphi \sim \tau_m$, which is often the case in a high-mobility semiconductors.

Having recalled basic concepts, the two distinct regimes of transport can be distinguished in an intuitive way: If the length L of the sample is much larger than the phase-relaxation length L_φ, then quantum interference phenomena disappear. That is, when $L_\varphi, L_m \ll L$, the description of transport should be based on classical models. This is the *ohmic regime*. On the other hand, when $L_\varphi, L_m > L$, the transport properties are determined by quantum interference effects. This is the *ballistic regime*.

1.4.1 Scattering mechanisms in heterostructures

In this section we provide a short overview of the most relevant scattering mechanisms (without claim of completeness) that are present in semiconductor heterostructure samples. We focus on two-dimensional electron gases in which the following scattering mechanisms arise:

- optical phonon scattering (dominant at high temperatures)
- acoustic phonon scattering (deformation potential and piezoelectric effects)
- magnetic impurity scattering

- ionized donor scattering (remote impurity)
- scattering from neutral defects or impurities.

As a reference, Fig. (1.4) shows the influence of different scattering mechanisms on the temperature dependent mobility of a bulk GaAs sample. The role of the scattering mechanisms which are relevant in an optimized 2-DEG in a Ga[Al]As heterojunction can be seen in Fig. (1.5).

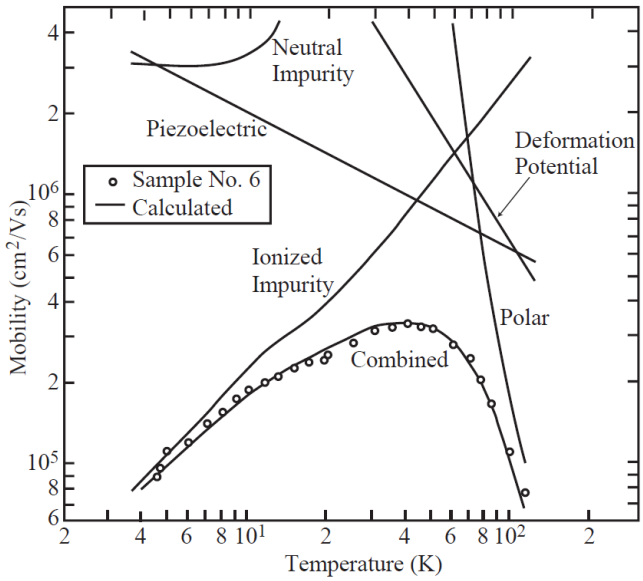

Figure 1.4: Influence of various scattering phenomena on the temperature dependence of the mobility of a three-dimensional GaAs sample [47].

As we can see, scattering effects can strongly limit the mobility of electrons in a 2-DEG. This fact may lead to the disappearance of ballistic electron transport, thus taking them into account is inevitable in realistic calculations. As a model, we are going to discuss effects related to point-like scatterers.

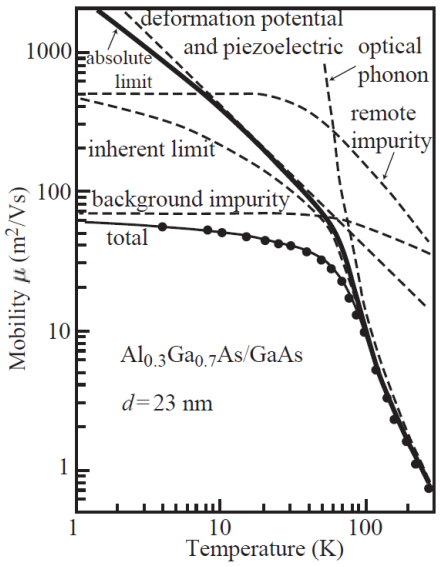

Figure 1.5: Influence of different scattering mechanisms on the mobility of a GaAs/AlGaAs heterostructure. The spacer layer thickness is denoted by d [36].

1.5 Conductance: Landauer-Büttiker approach

1.5.1 Landauer formula

Let us consider a ballistic conductor which is connected to two electron reservoirs ("Contact 1" and "Contact 2"). They are characterized by the electrochemical potentials μ_1 and μ_2 (see Fig. 1.6 (a)). When the dimensions of the nanodevice is large enough, the conductance can be written as $G = \sigma W/L$. Here, the length and the width are denoted by L and W, and the conductivity σ is a material constant which does not depend on the size of the sample. Let us investigate the behavior of G when $L \to 0$. Naively, one could expect the conductance to increase indefinitely. However, on the basis of experimental observations, G approaches a limiting value G_C when $L \leq L_m$, i.e., the conductor is much shorter than the mean free path.

Our goal is to determine the *contact resistance* G_C^{-1} by calculating the current flowing through a ballistic sample for given bias $\mu_1 - \mu_2$. We assume that the contacts are *reflectionless*. That is, the electrons can enter the contacts from the sample without reflections. In this case right propagating ($+k$) states in the conductor are occupied only by electrons originating from the left contact while $-k$ states are occupied only by electrons that originate from the right contact. (This holds because charge carriers that enter from the right contact populate the $-k$ states and empty without reflection into the left contact,

while the ones that enter from the left contact populate the $+k$ states and empty without reflection into the right contact.) Note that the wavenumber component in the x direction is denoted by k.

We argue that the quasi-Fermi level F^+ for the $+k$ states is always equal to μ_1 even when a bias $\mu_1 - \mu_2$ is applied (see Fig. 1.6 (b)). If we generate an electrochemical potential difference between left and right contacts, it can have no effect on the quasi-Fermi level F^+ for the $+k$ states since there is no causal relationship between the right contact and the $+k$ states. No electron originating in the right contact ever makes its way to a $+k$ state. Similarly we can argue that the quasi-Fermi level F^- for the $-k$ states in the right lead is always equal to μ_2. Hence at low temperatures the current is equal to that carried by all the $+k$ states lying between μ_1 and μ_2 [28].

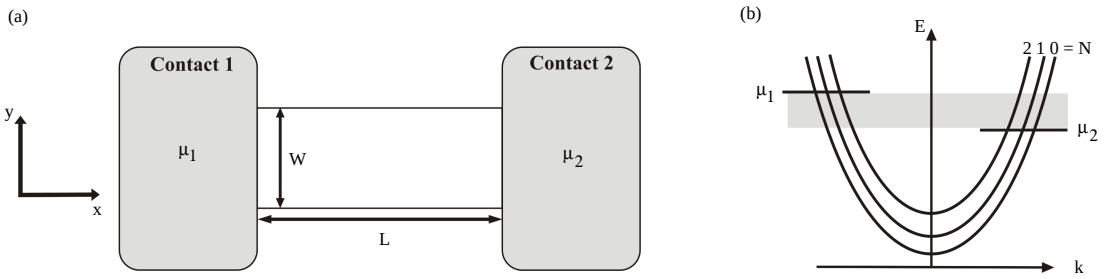

Figure 1.6: (a) Quantum wire connected to left and right electron reservoirs (gray). The electrochemical potentials of the reservoirs are μ_1 and μ_2. (b) Dispersion relation in the quantum channel. The gray-shaded energy interval is determined by the applied voltage between left and right reservoirs (bias window) [28].

Before we calculate the current there is an important statement corresponding to different transverse modes, see Fig. 1.6. The dispersion relation $E(N, k_x)$ related to the subband N (Fig. 1.6 (b)) has a cut-off energy

$$\varepsilon_N = E(N, k_x = 0) \tag{1.18}$$

below which no waves can propagate. The number of subbands that play a role in the conductance at an energy E is obtained by counting the number of modes having cut-off energies smaller than E:

$$M(E) = \sum_N \theta(E - \varepsilon_N). \tag{1.19}$$

We can evaluate the current carried by each transverse mode (labelled by subscript N in Fig. 1.6 b) separately and add them up.

First, we take into account a single transverse mode whose $+k$ states are occupied according to the function $f^+(E)$. Let us recognize that if a uniform electron gas with n

electrons per unit length move with a velocity of v, it carries a current is equal to env. The electron density is associated with a single k-state in a conductor of length L is given by $1/L$. The corresponding current I^+ can be written as

$$I^+ = \frac{e}{L}\sum_k v f^+(E) = \frac{e}{L}\sum_k \frac{1}{\hbar}\frac{\partial E}{\partial k} f^+(E). \tag{1.20}$$

Assuming periodic boundary conditions and converting the sum over k into an integral according to the usual prescription

$$\sum_k \quad \rightarrow \quad 2(\text{for spin}) \times \frac{L}{2\pi}\int \mathrm{d}k \tag{1.21}$$

we find

$$I^+ = \frac{2e}{h}\int_{\varepsilon}^{\infty} f^+(E)\mathrm{d}E, \tag{1.22}$$

where ε is the cut-off energy of the waveguide mode. If we consider a multi-mode channel, the formula for the current I^+ reads

$$I^+ = \frac{2e}{h}\int_{-\infty}^{\infty} f^+(E)M(E)\mathrm{d}E, \tag{1.23}$$

where the function $M(E)$ provides us the number of modes that are below the cut-off energy E. Then, we assume that the number of modes M is constant over the energy range $\mu_1 > E > \mu_2$, and at low temperature we find that

$$I = \frac{2e^2}{h}M\frac{(\mu_1 - \mu_2)}{e}, \tag{1.24}$$

where $(\mu_1 - \mu_2)/e$ is the bias voltage. Thus the contact resistance is given by $G_C^{-1} = h/2e^2M$. This is the resistance of a ballistic conductor.

As a generalization, the Landauer formula reads [26, 28]:

$$G = \frac{2e^2}{h}MT, \tag{1.25}$$

where the average transmission probability is denoted by T and M is the number of modes. Obviously, when the transmission probability equals unity, we recover the case discussed earlier.

1.5.2 Linear response

The way we recalled the derivation of the Landauer formula in the previous subsection relied on several assumptions. We used a simplified picture which is valid at zero

temperature and transport occurred only from the left contact to the right one. We also assumed that the current was carried by a narrow energy channel around the Fermi-level. This allowed us to write the current as

$$I = \frac{2e}{h}\overline{T}\left(\mu_1 - \mu_2\right), \tag{1.26}$$

where $\overline{T}$ denotes the product of the number of modes M and the transmission probability per mode T at the Fermi energy (assumed to be constant over the range $\mu_1 > E > \mu_2$).

Now we consider a more general case where transport takes place in the energy range

$$\mu_1 + nk_BT > E > \mu_2 - nk_BT, \tag{1.27}$$

where n is a small integer and k_B is the Boltzmann constant. Each energy value may correspond to a different transmission $\overline{T}$. At this point we include injection from both contacts. The influx of electrons per unit energy from lead 1 is given by

$$i_1^+(E) = \frac{2e}{h}Mf_1(E) \tag{1.28}$$

while the influx from lead 2 is given by

$$i_2^-(E) = \frac{2e}{h}M'f_2(E), \tag{1.29}$$

where the number of modes in lead 2 is denoted by M' and $f_1(E)$ ($f_2(E)$) is the energy distribution in lead 1 (lead 2) at non-zero temperatures. The outflux from lead 2 can be written as

$$i_2^+(E) = Ti_1^+(E) + (1-T')i_2^-(E) \tag{1.30}$$

while the outflux from lead 1 is written as

$$i_1^-(E) = (1-T)i_1^+(E) + T'i_2^-(E). \tag{1.31}$$

The current $i(E)$ flowing through the nanostructure is given by

$$\begin{aligned} i(E) &= i_1^+ - i_1^- = i_2^+ - i_2^- \\ &= Ti_1^+ - T'i_2^- = \frac{2e}{h}\left[M(E)T(E)f_1(E) - M'(E)T'(E)f_2(E)\right]. \end{aligned} \tag{1.32}$$

If we define the transmission function as $\overline{T} = M(E)T(E)$, Eq.(1.32) can be reformulated as

$$i(E) = \frac{2e}{h}\left[\overline{T}(E)f_1(E) - \overline{T}'(E)f_2(E)\right]. \tag{1.33}$$

Assuming $\overline{T}(E) = \overline{T}'(E)$, the total current is given by

$$I = \int i(E)\,\mathrm{d}E = \frac{2e}{h}\int \overline{T}(E)\left[f_1(E) - f_2(E)\right]\,\mathrm{d}E. \tag{1.34}$$

Why should the transmission function from 1 to 2 be equal to that from 2 to 1 ($\overline{T}(E) = \overline{T}'(E)$)? One could argue that they ought to be equal in order to ensure that there is no current at equilibrium ($i(E) = 0$ when $f_1(E) = f_2(E)$). Nevertheless, this argument only proves that $\overline{T}(E)$ should equal $\overline{T}'$ at equilibrium. When the investigated system is far from equilibrium, the applied bias could change the two transmission functions and could lead to $\overline{T}(E) \neq \overline{T}'(E)$. However, if we assume that there is no inelastic scattering (from one energy to another) inside the device, then it can be shown that $\overline{T}(E)$ is always equal to $\overline{T}'(E)$ for a two-terminal device even in the presence of a magnetic field.[28]

When both contacts of the investigated nanodevice are held at the same potential, $\mu_1 = \mu_2$, according to Eq. (1.34), $f_1(E) = f_2(E) \rightarrow I = 0$. If the state is shifted slightly from equilibrium, the current is proportional to the applied bias. The current form Eq. (1.34) can be written as

$$\delta I = \frac{2e}{h} \int \left([\overline{T}(E)]_{eq} \delta[f_1 - f_2] + [f_1 - f_2]_{eq} \delta[\overline{T}(E)] \right) \mathrm{d}E. \tag{1.35}$$

Naturally, we recognize that the second term vanishes. We can provide an expansion of the first term as

$$\delta[f_1 - f_2] \approx [\mu_1 - \mu_2] \left(\frac{\partial f}{\partial \mu} \right)_{eq} = \left(\frac{\partial f_0}{\partial E} \right) [\mu_1 - \mu_2], \tag{1.36}$$

where $f_0(E)$ is the equilibrium Fermi function which is given by

$$f_0(E) = \left[\frac{1}{1 + \exp[(E - \mu)/k_B T]} \right]_{\mu = E_f}. \tag{1.37}$$

At non-zero temperature, the *linear response formula* is written as follows

$$G = \frac{e \cdot \delta I}{(\mu_1 - \mu_2)} = \frac{2e^2}{h} \int \overline{T}(E) \left(-\frac{\partial f_0}{\partial E} \right) \mathrm{d}E. \tag{1.38}$$

In the low temperature limit we can write

$$f_0(E) \approx \theta(E_f - E) \quad \rightarrow \quad -\frac{\partial f_0}{\partial E} \approx \delta(E_f - E). \tag{1.39}$$

Then we reach the expression for the conductance within linear response at zero temperature:

$$G = \frac{2e^2}{h} \overline{T}(E_f). \tag{1.40}$$

Each quantity is evaluated in equilibrium and thus linear response refers to an equilibrium property of the system.

Chapter 2

Spin-orbit interaction, spin density operator

Spin-dependent transport processes play a central role in our investigations, therefore it is important to summarize the most important reasons why the spin degrees of freedom can be controlled in solid state systems. In the current chapter we start with the Dirac equation, perform a systematic power expansion to see the physical origin of the spin-orbit interaction.

2.1 Large and small component

The Dirac equation in the form originally proposed by Dirac [48] reads:

$$\left[\frac{1}{c}\frac{\partial}{\partial t}+\sum_{k=1}^{3}\hat{\alpha}_k\frac{\partial}{\partial x_k}+\frac{imc}{\hbar}\hat{\beta}\right]\mid\Psi\rangle=0, \tag{2.1}$$

where $\hat{\alpha}_k$ ($k=1,2,3$) and $\hat{\beta}$ are independent Hermitian matrices satisfying the following anticommutation relations:

$$\left\{\hat{\alpha}_k,\hat{\beta}\right\}=\hat{0},\quad \{\hat{\alpha}_k,\hat{\alpha}_l\}=2\delta_{kl}\hat{I}. \tag{2.2}$$

One of the possible choices for these matrices is the following:

$$\hat{\alpha}_k=\begin{pmatrix}\hat{0} & \hat{\sigma}_k\\ \hat{\sigma}_k & \hat{0}\end{pmatrix},\quad k=1,2,3,\quad \hat{\beta}=\begin{pmatrix}\hat{I} & \hat{0}\\ \hat{0} & -\hat{I}\end{pmatrix}, \tag{2.3}$$

where the blocks are the 2×2 Hermitian *Pauli* or *spin* matrices[49, 50]:

$$\hat{\sigma}_1=\begin{pmatrix}0 & 1\\ 1 & 0\end{pmatrix},\quad \hat{\sigma}_2=\begin{pmatrix}\hat{0} & -i\\ i & \hat{0}\end{pmatrix},\quad \hat{\sigma}_3=\begin{pmatrix}1 & 0\\ 0 & -1\end{pmatrix}, \tag{2.4}$$

and

$$\hat{I}=\begin{pmatrix}1 & 0\\ 0 & 1\end{pmatrix},\quad \hat{0}=\begin{pmatrix}0 & 0\\ 0 & 0\end{pmatrix}. \tag{2.5}$$

Since $\hat{\alpha}_k$ and $\hat{\beta}$ are 4×4 Hermitian matrices, each wavefunction $\mid \Psi\rangle$ appearing in Eq. (2.1) has four components and they can be written as a column vector:

$$\mid \Psi\rangle = \begin{pmatrix} \psi_1 \\ \psi_2 \\ \psi_3 \\ \psi_4 \end{pmatrix}. \tag{2.6}$$

These four-component vectors are called *Dirac spinors*.

Let us overview the free motion of particles described by the Dirac equation. The matrix equation (2.1) can be written in the form of the Schrödinger equation:

$$i\hbar \frac{\partial}{\partial t} \mid \Psi\rangle = \hat{H}_D \mid \Psi\rangle \tag{2.7}$$

with the Dirac Hamiltonian which – in this case – does not contain the potential term:

$$\hat{H}_D = c\left(\hat{\boldsymbol{\alpha}} \cdot \hat{\mathbf{P}}\right) + mc^2\hat{\beta}. \tag{2.8}$$

Let us study a stationary state, the time evolution of which is given by

$$\Psi(\mathbf{r}, t) = \Psi(\mathbf{r}) e^{-\frac{i}{\hbar}\varepsilon t}. \tag{2.9}$$

Accordingly, the amplitudes $\Psi(\mathbf{r})$ carry the spatial dependence. By substituting (2.9) into (2.7), we obtain the eigenvalue equation

$$\hat{H}_D \Psi(\mathbf{r}) = \varepsilon \Psi(\mathbf{r}). \tag{2.10}$$

The spectrum of $\hat{H}_D$ determines the time-dependence of the complete wavefunction (2.9) in stationary states. For many applications, it is useful to express the four-component spinor (2.6) in terms of two-component functions

$$\varphi = \begin{pmatrix} \psi_1 \\ \psi_2 \end{pmatrix}, \quad \chi = \begin{pmatrix} \psi_3 \\ \psi_4 \end{pmatrix} \tag{2.11}$$

by writing $\Psi(\mathbf{r})$ in a form of a *bispinor*

$$\Psi(\mathbf{r}) = \begin{pmatrix} \varphi \\ \chi \end{pmatrix}. \tag{2.12}$$

We can write (2.10) in the form of two matrix equations with use of $\hat{\boldsymbol{\alpha}}$ and $\hat{\beta}$ matrices

$$\begin{aligned} \varepsilon\varphi &= c\left(\hat{\boldsymbol{\sigma}} \cdot \hat{\mathbf{P}}\right)\chi + mc^2\varphi, \\ \varepsilon\chi &= c\left(\hat{\boldsymbol{\sigma}} \cdot \hat{\mathbf{P}}\right)\varphi - mc^2\chi. \end{aligned} \tag{2.13}$$

States with a well-defined value of the momentum (when $\hat{\mathbf{P}}$ can be replaced by its eigenvalue $\mathbf{p}$) will be described by the equations

$$\begin{aligned} (mc^2 - \varepsilon)\,\varphi + c\,(\hat{\boldsymbol{\sigma}} \cdot \mathbf{p})\,\chi = 0, \\ c\,(\hat{\boldsymbol{\sigma}} \cdot \mathbf{p})\,\varphi - (mc^2 + \varepsilon)\,\chi = 0. \end{aligned} \tag{2.14}$$

Naturally, this system of homogeneous and linear equations has non-trivial solution only if the determinant of the coefficients vanishes, that is,

$$\begin{vmatrix} mc^2 - \varepsilon & c\,(\hat{\boldsymbol{\sigma}} \cdot \mathbf{p}) \\ -c\,(\hat{\boldsymbol{\sigma}} \cdot \mathbf{p}) & mc^2 + \varepsilon \end{vmatrix} = 0. \tag{2.15}$$

We can calculate the determinant (2.15) easily with the following useful operator identity

$$\left(\hat{\boldsymbol{\sigma}} \cdot \hat{\mathbf{A}}\right)\left(\hat{\boldsymbol{\sigma}} \cdot \hat{\mathbf{B}}\right) = \left(\hat{\mathbf{A}} \cdot \hat{\mathbf{B}}\right) + i\left(\hat{\boldsymbol{\sigma}} \cdot \left[\hat{\mathbf{A}} \times \hat{\mathbf{B}}\right]\right), \tag{2.16}$$

which follows from the commutation and anticommutation relations of the Pauli matrices and which is valid for arbitrary two operators $\hat{\mathbf{A}}$ and $\hat{\mathbf{B}}$ that commute with $\hat{\boldsymbol{\sigma}}$. Then we obtain a quadratic equation for ε:

$$m^2c^4 - \varepsilon^2 + c^2p^2 = 0, \tag{2.17}$$

which provides two real solutions

$$\varepsilon_{1,2} = \pm E_p, \tag{2.18}$$

where $E_p = c\sqrt{p^2 + m^2c^2}$ can be called the particle energy. We use the term positive (negative) solution for $\Psi(\mathbf{r})$ when $\varepsilon = E_p$ $(-E_p)$.

If ε is determined by Eq. (2.18), we can use Eq. (2.14) to express one of the two-component functions in terms of the other. E.g.:

$$\chi = \frac{c\,(\hat{\boldsymbol{\sigma}} \cdot \mathbf{p})}{mc^2 + \varepsilon}\varphi. \tag{2.19}$$

Now we turn to the non-relativistic ($v/c \ll 1$) limit and consider the solutions with positive energies

$$\varepsilon = E_p = mc^2 + E', \quad \text{where} \quad E' \ll mc^2. \tag{2.20}$$

Then it follows from (2.19) that

$$\chi = \frac{c\,(\boldsymbol{\sigma} \cdot \mathbf{p})}{2mc^2 + E'}\varphi \approx \frac{(\boldsymbol{\sigma} \cdot \mathbf{p})}{2mc}\varphi \ll \varphi. \tag{2.21}$$

If the particle velocity is small compared to the velocity of light, we see that two of the four components of the wavefunction are small compared to the other two. In non-relativistic approximation ψ_1 and ψ_2 are often called the *large components*, ψ_3 and ψ_4 the *small components*. If we investigate the case of states with $\varepsilon = -E_p$ (that is, negative solutions), the functions ψ_1 and ψ_2 are small and the functions ψ_3 and ψ_4 are large [50].

2.2 Expansion of the Dirac equation: the spin-orbit interaction term

In the previous subsection we have introduced the large and the small components of the Dirac spinor in the non-relativistic limit, i.e., when the investigated particle propagates slowly in comparison to the speed of light, and the relation (2.21) is valid. As we shall see, this approximation leads to a new equation involving only the large component φ. Moreover, we shall obtain a formal expansion of the spinor valued wave function in powers of $1/c$.

To this end, we start with a more general physical problem, i.e., we consider an electron moving in an electromagnetic external field. The corresponding Dirac equation can be written

$$i\hbar\frac{\partial\Psi}{\partial t} = \left\{c\hat{\boldsymbol{\alpha}}\left(\hat{\mathbf{P}} - \frac{e}{c}\mathbf{A}\right) + mc^2\hat{\beta} + e\Phi\right\}\Psi, \tag{2.22}$$

where $\mathbf{A}$ and Φ are the vector and scalar potential and Ψ is the Dirac bispinor that is given by Eq. (2.12). The relativistic energy of the particle includes also its rest energy mc^2. In the non-relativistic limit, we omit this term, and introduce a spinor Ψ':

$$\Psi' = \Psi e^{\frac{i}{\hbar}mc^2 t}. \tag{2.23}$$

Then

$$\left(i\hbar\frac{\partial}{\partial t} + mc^2\right)\Psi' = \left\{c\hat{\boldsymbol{\alpha}}\left(\hat{\mathbf{P}} - \frac{e}{c}\mathbf{A}\right) + mc^2\hat{\beta} + e\Phi\right\}\Psi'. \tag{2.24}$$

The spinor Ψ' can also be written in the following form

$$\Psi' = \begin{pmatrix}\varphi'\\ \chi'\end{pmatrix}. \tag{2.25}$$

This leads to

$$\left(i\hbar\frac{\partial}{\partial t} - e\Phi\right)\varphi' = c\hat{\boldsymbol{\sigma}}\left(\hat{\mathbf{P}} - \frac{e}{c}\mathbf{A}\right)\chi', \tag{2.26}$$

$$\left(i\hbar\frac{\partial}{\partial t} - e\Phi + 2mc^2\right)\chi' = c\hat{\boldsymbol{\sigma}}\left(\hat{\mathbf{P}} - \frac{e}{c}\mathbf{A}\right)\varphi'. \tag{2.27}$$

In the following, the functions φ and χ will be used without primes. In the first approximation, only the term $2mc^2\chi$ is kept on the left-hand side of Eq.(2.27), which provides

$$\chi = \frac{1}{2mc}\boldsymbol{\sigma}\left(\mathbf{P} - \frac{e}{c}\mathbf{A}\right)\varphi. \tag{2.28}$$

If we substitute $\chi(\varphi)$ function in Eq. (2.26), we find that

$$\left(i\hbar\frac{\partial}{\partial t} - e\Phi\right)\varphi = \frac{1}{2m}\left(\hat{\boldsymbol{\sigma}}\left(\hat{\mathbf{P}} - \frac{e}{c}\mathbf{A}\right)\right)^2\varphi. \tag{2.29}$$

The operator identity (2.16) is used for Eq. (2.29) to find a new equation for φ :

$$i\hbar\frac{\partial\varphi}{\partial t} = H\varphi = \left[\frac{1}{2m}\left(\mathbf{P} - \frac{e}{c}\mathbf{A}\right)^2 + e\Phi - \frac{e\hbar}{2mc}\boldsymbol{\sigma}\cdot\mathbf{B}\right]\varphi. \tag{2.30}$$

This is the Pauli equation [51].

We can continue the expansion to include terms of order $1/c^2$. Assuming that there is no external magnetic field ($\mathbf{A} = \mathbf{0}$) and inserting $\mathbf{E} = -\nabla\Phi$, we obtain

$$H = \frac{\mathbf{P}^2}{2m} + e\Phi - \frac{\mathbf{P}^4}{8m^3c^2} - \frac{e\hbar}{4m^2c^2}\boldsymbol{\sigma}\cdot(\mathbf{E}\times\mathbf{P}) - \frac{e\hbar^2}{8m^2c^2}\nabla\mathbf{E}. \tag{2.31}$$

On the right hand side, the last three terms are the corrections of order $1/c^2$ [52]. Now, the relevant term for us is the second of them. It is called *spin-orbit interaction*.

If the electric field has central symmetry, we can write

$$\mathbf{E} = -\hat{\mathbf{r}}\frac{\mathrm{d}\Phi}{\mathrm{d}r}, \tag{2.32}$$

and the spin-orbit interaction operator can be expressed in the following form

$$H_{SO} = \frac{\hbar^2}{2m^2c^2r}\frac{\mathrm{d}V}{\mathrm{d}r}\mathbf{L}\cdot\mathbf{S}, \tag{2.33}$$

where $\mathbf{L}$ is the orbital angular momentum operator, $\mathbf{S} = \frac{1}{2}\boldsymbol{\sigma}$ denotes the electron spin operator and $V = e\Phi$ is the electric potential.

We shall use the abbreviation SOI for spin-orbit interaction in this dissertation.

2.3 Dresselhaus and Rashba spin-orbit interaction

Our work focuses on the electronic states in 2-DEG. In certain semiconductors, the effect of spin degeneracy arise, which is the result of the combination of spatial inversion symmetry of the crystal lattice and time-reversal symmetry. Both symmetry operations replace the wavenumber vector $\mathbf{k}$ by $-\mathbf{k}$. Time inversion also inverts the orientation of the spin. Hence the inversion symmetry manifests itself in space and time as well. If we combine both effects, we have a twofold degeneracy of the single particle energies: $E_\uparrow(\mathbf{k}) = E_\downarrow(\mathbf{k})$. In the absence of an external field $\mathbf{B}$, spin degeneracy is due to the combined effect of inversion symmetry:

$$\text{space inversion symmetry:} \quad E_\uparrow(\mathbf{k}) = E_\uparrow(-\mathbf{k}) \tag{2.34}$$

and

$$\text{time inversion symmetry:} \quad E_\uparrow(\mathbf{k}) = E_\downarrow(-\mathbf{k}). \tag{2.35}$$

When the space inversion symmetry of the crystal is broken, for instance, in zinc blende semiconductors (GaAs, InAs or InSb), the degeneracy $E_\uparrow(\mathbf{k}) = E_\downarrow(\mathbf{k})$ disappears. Indeed, the dispersion relations have two branches, $E_\uparrow(\mathbf{k})$ and $E_\downarrow(\mathbf{k})$. This is the so-called *bulk inversion asymmetry* (it is often abbreviated BIA) giving rise to *Dresselhaus*-type SOI term in the Hamiltonian [10, 53]. On the other hand, an epitaxially grown structure can create a confinement potential without spatial inversion symmetry [54, 55]. This is the phenomenon of *structure inversion asymmetry* (SIA), giving rise to the *Rashba*-type SOI term in the Hamiltonian [9]. It has been demonstrated in asymmetric semiconductor quantum wells [56]. We can write the operator H for two-dimensional electron gases as

$$H = H_0 + \beta_D(\sigma_x k_x - \sigma_y k_y) + \alpha_R(\sigma_x k_y - \sigma_y k_x). \tag{2.36}$$

The first term H_0 provides the energy of the electrons without spin-orbit coupling. The second one is the Dresselhaus term describing the lack of inversion symmetry of the crystal structure. The Dresselhaus coefficient β_D is given by the band structure parameters of the material and the thickness of the electron gas in the growth directions.

As the Dresselhaus spin-orbit coupling is strongly related to bulk properties of the semiconductor, β_D is fixed and cannot be tuned. Let us mention that ab initio calculations reveal unexpected spin structure also for centrosymmetric crystals (where inversion is a symmetry) [57, 58].

The third term on the right hand side of Eq. (2.36) is called Rashba spin-orbit interaction term. Its coefficient α_R incorporates an electric field. In other words, it can be modified by an external gate voltage [59, 60, 61] which is characterized by E_z, which is normal to the plane of 2-DEG and

$$\alpha_R = \alpha\langle E_z\rangle, \tag{2.37}$$

with α being a constant (for a given material) and $\langle E_z\rangle$ is the electric field averaged in the z-direction. Typical values for electric fields in heterostructures are a few $\mathrm{mV/Å}$ [15]. We can see the dispersion relations in the conduction band in the presence of both types of spin-orbit couplings in Fig. 2.1.

Values of Rashba and Dresselhaus coefficients for certain materials can be found in Ref. [53].

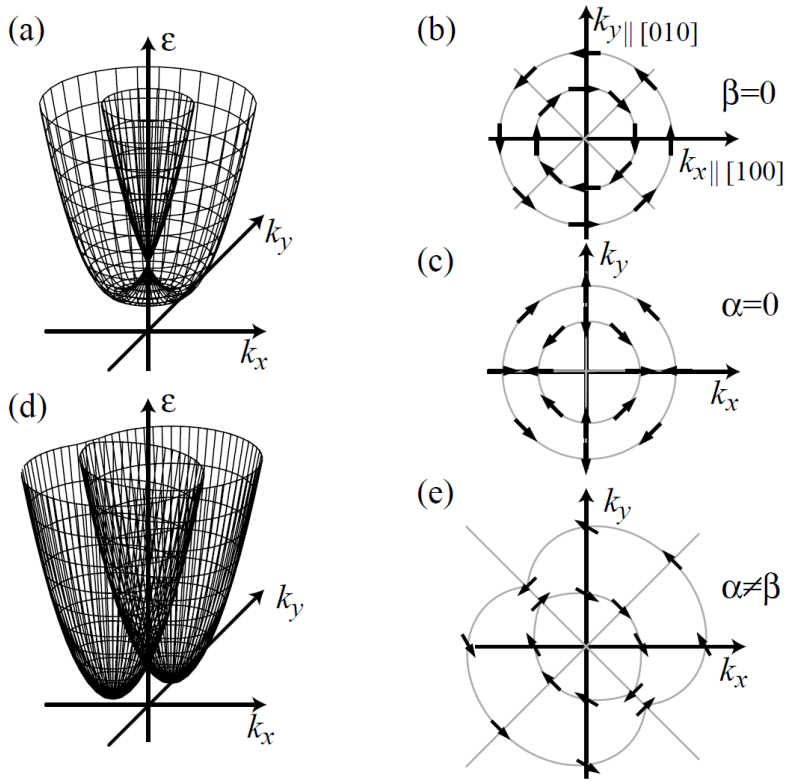

Figure 2.1: Schematic view of the dispersion relations in the conduction band in the presence of SOI. (a) The case considering either only the Rashba term or only the Dresselhaus term. (b) For the Rashba term ($\beta = 0$), Fermi circles and spin orientations are shown. (c) For the Dresselhaus term ($\alpha = 0$), we can also see Fermi contours and spin orientations. (d) Dispersion relation in the case of $\alpha \neq 0$ and $\beta \neq 0$, i.e., both terms are present. (e) Fermi contours and spin orientations for comparable Rashba and Dresselhaus terms. (Adapted from Ref. [62, 15].)

2.4 Density operator and spin-polarization

Mixed states in quantum mechanics or quantum statistics can be used to describe the behavior of an ensemble. Let us consider a quantum system which consists of N individual sub-systems, which are labelled by $\lambda = 1, 2, 3, \cdots, N$. We assume that each of them is in a pure state, i.e., it can be described by a state vector $\psi^{(\lambda)}$, or, using Dirac bra-ket notation $|\lambda\rangle$. We also assume that these states are normalized,

$$\langle\lambda|\lambda\rangle = 1, \tag{2.38}$$

but we shall not require orthogonality.

For our investigation a complete set of basis vectors $|n\rangle$ is chosen. These basis vectors are equivalent to orthonormal eigenvectors of some complete set of operators which implies

$$\langle n|m\rangle = \delta_{nm}. \tag{2.39}$$

Since the chosen basis is also complete, we can write

$$\sum_n |n\rangle\langle n| = \hat{I}. \tag{2.40}$$

Any pure state $|\ \lambda\rangle$ can be expanded in basis vectors $|\ n\rangle$, so thus

$$|\lambda\rangle = \sum_n c_n^{(\lambda)} |n\rangle. \tag{2.41}$$

For arbitrary $|\lambda\rangle$ the corollary of (2.38) and (2.39) is

$$\sum_n |c_n^{(\lambda)}|^2 = \sum_n |\langle n|\lambda\rangle|^2 = 1. \tag{2.42}$$

Let us consider an observable represented by an operator $\hat{A}$. The expectation value (or first moment in probability theory) of this operator in the pure state $|\lambda\rangle$ is

$$\langle\hat{A}\rangle_{|\lambda\rangle} = \langle\lambda|\hat{A}|\lambda\rangle = \sum_n \sum_{n'} c_{n'}^{(\lambda)*} c_n^{(\lambda)} \langle n'|\hat{A}|n\rangle = \sum_n \sum_{n'} \langle n|\lambda\rangle\langle\lambda|n'\rangle\langle n'|\hat{A}|n\rangle. \tag{2.43}$$

The average value of $\hat{A}$ over the ensemble, called the *ensemble* (or statistical) average of $\hat{A}$ is given by

$$\langle\hat{A}\rangle = \sum_\lambda^N W_\lambda \langle\hat{A}\rangle_{|\lambda\rangle}, \tag{2.44}$$

where W_λ is the *statistical weight* of the pure state $|\lambda\rangle$. Note that W_λ is equal to the probability of finding the system in state $|\lambda\rangle$. According to probability theory, the statistical weights obey the following inequality:

$$0 \leq W_\lambda \leq 1 \tag{2.45}$$

and

$$\sum_{\lambda=1}^{N} W_\lambda = 1. \tag{2.46}$$

Using the definition of the ensemble average of $\hat{A}$ and the expression for $\langle \hat{A} \rangle_{|\lambda\rangle}$, we can write:

$$\langle \hat{A} \rangle = \sum_{\lambda=1}^{N} \sum_{n} \sum_{n'} \langle n|\lambda\rangle W_\lambda \langle \lambda|n'\rangle \langle n'|\hat{A}|n\rangle. \tag{2.47}$$

At this point, we introduce the *density operator*

$$\hat{\varrho} = \sum_{\lambda=1}^{N} W_\lambda |\lambda\rangle\langle\lambda|. \tag{2.48}$$

The ensemble average of $\hat{A}$ can be expressed using the density operator as follows

$$\langle \hat{A} \rangle = \sum_{\lambda=1}^{N} \sum_{n} \sum_{n'} \langle n|\hat{\varrho}|n'\rangle \langle n'|\hat{A}|n\rangle = \sum_{n} \langle n|\hat{\varrho}\hat{A}|n\rangle = Tr(\hat{\varrho}\hat{A}). \tag{2.49}$$

We also note that if we take $\hat{A}$ to be the identity operator $\hat{I}$ and use the fact that the pure states $|\lambda\rangle$ are normalized to unity, we obtain the normalization condition

$$Tr(\hat{\varrho}) = 1. \tag{2.50}$$

If the pure states $|\lambda\rangle$ are not normalized, the ensemble average of $\hat{A}$ is given by

$$\langle \hat{A} \rangle = \frac{Tr(\hat{\varrho}\hat{A})}{Tr(\hat{\varrho})}. \tag{2.51}$$

Naturally, the density operator is a self-adjoint operator (that is, $\hat{\varrho} = \hat{\varrho}^\dagger$) [63, 64].

In the following, we shall provide the density operator for a spin-$1/2$ system and introduce the polarization. As it is known, the 2×2 unit matrix $\hat{I}$ and the three Pauli spin matrices form a complete set of 2×2 matrices. Therefore we can write the density matrix $\hat{\varrho}$ as

$$\hat{\varrho} = a_0 \hat{I} + \sum_{i=1}^{3} a_i \hat{\sigma}_i = a_0 \hat{I} + \mathbf{a} \cdot \hat{\boldsymbol{\sigma}}, \tag{2.52}$$

where a_0, a_x, a_y and a_z are four complex parameters. If we take the trace of both sides of this equation then the value of the parameter a_0 can easily be obtained. observing that $Tr(\hat{\varrho}) = 1$, $Tr(\hat{I}) = 2$ and $Tr(\sigma_k) = 0$ (with $k = x, y, z$), we find that

$$a_0 = \frac{1}{2}. \tag{2.53}$$

Now, we calculate the average value of $\hat{\sigma}_i$ to obtain the meaning of the coefficients a_k ($k = x, y, z$). As we have seen previously, the ensemble average of an arbitrary operator $\hat{A}$ can be expressed in terms of the density operator. Therefore, we have

$$\langle \hat{\sigma}_k \rangle = Tr(\hat{\varrho}\hat{\sigma}_k). \tag{2.54}$$

From (2.52) together with the fact that $Tr(\hat{\sigma}_k\hat{\sigma}_l) = 2\delta_{kl}$, we can write

$$\langle \hat{\sigma_k} \rangle = 2a_k, \tag{2.55}$$

where $k = x, y, z$. Using the relations obtained above, we can rewrite (2.52) in the form of

$$\varrho = \frac{1}{2}\left(I + \boldsymbol{\sigma} \cdot \mathbf{P}\right), \tag{2.56}$$

where we have introduced the *polarization vector*

$$\mathbf{P} = \langle \boldsymbol{\sigma} \rangle. \tag{2.57}$$

Making use of the Pauli matrices (2.1), we can write the density operator ϱ in the form

$$\varrho = \frac{1}{2}\begin{pmatrix} 1 + P_z & P_x - iP_y \\ P_x + iP_y & 1 - P_z \end{pmatrix}. \tag{2.58}$$

Our goal is to give a simple physical interpretation to the polarization vector $\mathbf{P}$. We can diagonalize ϱ. So that

$$\varrho = \frac{1}{2}\begin{pmatrix} 1 + P & 0 \\ 0 & 1 - P \end{pmatrix}, \tag{2.59}$$

where the function $P = \pm|\mathbf{P}| = \pm(P_x^2 + P_y^2 + P_z^2)^{1/2}$.

In the case of $P = 0$, the density operator equals to $\frac{1}{2}I$ and $Tr(\varrho^2) = \frac{1}{2}$. The system is said to be completely *unpolarized* or in a completely *random state*. Otherwise, there are two *pure* states corresponding to the values $P = +1$ and $P = -1$, respectively. The system is *totally polarized* in the direction of the polarization vector (when $P = +1$) or in the opposite direction (when $P = -1$). The density matrices of pure systems are

$$\varrho_+ = \begin{pmatrix} 1 & 0 \\ 0 & 0 \end{pmatrix}, \quad \text{for} \quad P = +1, \tag{2.60}$$

and

$$\varrho_- = \begin{pmatrix} 0 & 0 \\ 0 & 1 \end{pmatrix}, \quad \text{for} \quad P = -1. \tag{2.61}$$

An important remark is that an unpolarized system of spin-$1/2$ particles can be considered as a mixture of two pure systems. Namely

$$\varrho_{unp} = \frac{1}{2}I = \frac{1}{2}(\varrho_+ + \varrho_-). \tag{2.62}$$

The system is often called *partially polarized* when $0 < |P| < 1$. We can write

$$\frac{1}{2}Tr(\varrho^2) = \frac{1}{2}(1 + P^2) < 1. \tag{2.63}$$

Owing to this property of $|P|$, it is referred to the *degree of polarization* of the system. Let us note additionally, that $Tr(\varrho^2)$ is an increasing function of $|P|$.

Chapter 3

Time-dependent quantum systems and Floquet theory

In this chapter we review the most important theorems and concepts of Floquet theory, in order to investigate quantum systems that are described by a time-dependent Hamiltonian. In this case, we focus on time-periodic Hamiltonians and their spectra and eigenfunctions. The Floquet theory proves oneself to be a useful mathematical toolkit to calculate the solutions of the Schrödinger equation which includes the relevant time-periodic Hamiltonian.

First of all, let us recall the purely mathematical aspects of Floquet's theory, which corresponds to *ODE*s (*O*rdinary *D*ifferential *E*quations), more precisely, to the class of solutions to periodic linear differential equations of the form

$$\dot{x} = A(t)x. \tag{3.1}$$

Here is $A(t)$ a piecewise continuous periodic function with period T. Floquet's theorem [Gaston Floquet (1883)] gives a canonical form for each fundamental matrix solution of this common linear system.[65]

In the following, we delineate this theorem without proof.

Theorem. *If $\Phi(t)$ is a fundamental matrix solution of the linear periodic system $\dot{x} = A(t)x$, where $x(t)$ is a column vector of length n and $A(t)$ is an $n \times n$ periodic matrix with period T, then the same holds for $\Phi(t+T)$. Moreover, there exists an invertible $n \times n$ matrix $P(t)$ which is also periodic $(P(t+T) = P(t))$, such that*

$$\Phi(t) = P(t)\exp(Bt), \tag{3.2}$$

where B is also an $n \times n$ matrix.

After the general mathematical concepts, let us consider a time-dependent, time-periodic Hamiltonian, for which

$$H(t+T) = H(t), \tag{3.3}$$

for all values of t. We calculate the solution of the Schrödinger equation:

$$i\hbar\frac{\partial}{\partial t}|\Psi(t)\rangle = H(t)|\Psi(t)\rangle. \tag{3.4}$$

The time-dependent state can be written as $|\Psi(t)\rangle = U(t,t_0)|\Psi(t_0)\rangle$. The unitary time-evolution operator $U(t,t_0)$ propagates the system from the initial state $|\Psi(t_0)\rangle$ to $|\Psi(t)\rangle$. Generally, it can be written as

$$U(t,t_0) = \mathcal{T}\exp\left[-\frac{i}{\hbar}\int_{t_0}^{t} H(\tau)\mathrm{d}\tau\right], \tag{3.5}$$

where $\mathcal{T}$ is the time-ordering operator [66]. At this point, we introduce the Floquet Hamiltonian with the help of the Schrödinger equation

$$\mathcal{H}(t) = H(t) - i\hbar\frac{\partial}{\partial t}. \tag{3.6}$$

It is also time-periodic with period T. The commutator of the Floquet Hamiltonian and the period-shift operator $U(t+T,t)$ vanishes. Thus we can obtain a system of simultaneous eigenstates for $\mathcal{H}(t)$ and $U(t+T,t)$. Since the period-shift operator is unitary, its eigenvalue equation has to be of the form

$$U(t+T,t)|\Psi(t)\rangle = e^{i\varphi}|\Psi(t)\rangle. \tag{3.7}$$

To find the dependence of φ on T, we use the compositional property of the time evolution operator and exploit periodicity to reach

$$\begin{aligned} U(t+nT,t) &= U[t+nT,t+(n-1)T]U[t+(n-1)T,t+(n-2)T]\cdots U(t+T,t) \\ &= U^n(t+T,t), \end{aligned} \tag{3.8}$$

where n is a positive integer. Let us apply the relation (3.8) to the eigenvalue equation:

$$e^{i\varphi(nT)}|\Psi(t)\rangle = U(t+nT,t)|\Psi(t)\rangle = U^n(t+T,t)|\Psi(t)\rangle = \left(e^{i\varphi(T)}\right)^n|\Psi(t)\rangle. \tag{3.9}$$

We can write the function φ in the form of $\varphi = -(\varepsilon/\hbar)T$, were the 'Floquet exponent' ε is yet undetermined. The simultaneous eigenstates of $\mathcal{H}(t)$ and $U(t+T,t)$ satisfy

$$U(t+T,t)|\Psi(t)\rangle = e^{-\frac{i}{\hbar}\varepsilon T}|\Psi(t)\rangle, \tag{3.10}$$

leading to

$$|\Psi(t)\rangle = e^{-\frac{i}{\hbar}\varepsilon(t-t_0)}|\phi(t)\rangle. \tag{3.11}$$

Let us see why $|\phi(t)\rangle$ is time-periodic:

$$|\phi(t+T)\rangle = e^{\frac{i}{\hbar}\varepsilon(t+T-t_0)}|\Psi(t+T)\rangle = e^{\frac{i}{\hbar}\varepsilon(t+T-t_0)}U(t+T,t)|\Psi(t)\rangle = e^{\frac{i}{\hbar}\varepsilon(t+T-t_0)}e^{-\frac{i}{\hbar}\varepsilon T}|\Psi(t)\rangle = |\phi(t)\rangle. \tag{3.12}$$

By inserting the Floquet solution into the Schrödinger equation, we obtain

$$\mathcal{H}(t)|\Psi(t)\rangle = \left[H - i\hbar\frac{\partial}{\partial t}\right] e^{-\frac{i}{\hbar}\varepsilon t}|\phi(t)\rangle = e^{-\frac{i}{\hbar}\varepsilon t}\left[\mathcal{H}(t) - \varepsilon\right]|\phi(t)\rangle = 0. \tag{3.13}$$

We can see that the Floquet states are eigenstates of the Floquet Hamiltonian,

$$\mathcal{H}(t)|\phi(t)\rangle = \varepsilon|\phi(t)\rangle. \tag{3.14}$$

The following theorem summarizes our observations.

Theorem. *The basic solutions to the time-dependent Schrödinger equation with time-periodic Hamiltonian $\hat{H} = \hat{H}(t+T)$ can be given in the form*

$$|\Psi_\alpha(t)\rangle = e^{-\frac{i}{\hbar}\varepsilon_\alpha(t-t_0)}|\phi_\alpha(t)\rangle, \tag{3.15}$$

where ε_α are the Floquet exponents and $|\phi_\alpha(t)\rangle$ are the time-periodic Floquet states, which are solutions of the Floquet-type Schrödinger equation

$$\mathcal{H}(t)|\phi(t)_\alpha\rangle = \varepsilon_\alpha|\phi(t)_\alpha\rangle. \tag{3.16}$$

ε_α and $|\phi(t)_\alpha\rangle$ are called quasi-eigenenergies and quasi-eigenstates.

An arbitrary solution of the Floquet-type Schrödinger equation can then be expressed in terms of the non-redundant Floquet states:

$$|\Psi(t)\rangle = \sum_\alpha c_\alpha e^{-\frac{i}{\hbar}\varepsilon_\alpha(t-t_0)}|\phi_\alpha(t)\rangle, \tag{3.17}$$

where the coefficients c_α are given by the inner product $\langle\phi_\alpha(t_0)|\Psi(t_0)\rangle$.

Part II

Chapter 4

Stationary spin-orbit interaction controlled properties of 2D superlattices

Our theoretical investigation focuses on a model of two-dimensional (2D) superlattices. They can be fabricated from, e.g., InAlAs/InGaAs based heterostructures [67] or HgTe/HgCdTe quantum wells [68], where the propagation of electrons is described by a Hamiltonian which includes the Rashba-type [9] spin-orbit interaction term. This effect, which is essentially the same as the one which causes the fine structure of atomic spectra, results in spin-dependent transport phenomena. The practical importance of Rashba-type SOI is that its strength can be modulated by external gate voltages [69, 60]. Finite periodic structures such as quantum ring arrays have already been realized experimentally [21] and have also been described theoretically [70, 71, 72, 73]. The spin-transformation properties of finite networks suggest various possible spintronic applications as well [72, 73, 74]. The electronic spin separation effect has been observed in an InGaAs based heterostructure (with Rashba SOI) [75]. The Rashba Hamiltonian was proven to be able to describe the splitting of the conduction band as a result of spin-orbit coupling in the presence of an external field and is commonly used to model the electronic structure of confined narrow-gap semiconductors [76].

This part of the dissertation contains two chapters. First, we discuss the spin-dependent band scheme of infinite superlattices and the conductance properties of finite nano networks as well as their relation to several possible spintronic applications. In Chap. 5, the quantum mechanical conductance is investigated at "high" temperatures.

4.1 Spin-dependent Hamiltonian of quantum superlattices

The two-dimensional superlattice model that we consider is shown in Fig. 4.1. For conventional bulk material, the interatomic distances are not higher than several Å . E.g., for sodium chloride crystal the lattice constant is equal to $5,63$ Å [77]. On the other hand, the lattice constants of these artificial superlattices are of the order of $10\,\mathrm{nm}$, giving rise to characteristic energies orders of magnitude below band-related bulk energy values.

In our numerical calculations the characteristic parameters of the lattice, for instance the lattice constant and the angle between the wires can be modified. Therefore we can investigate the effects of these parameters on various band structures.

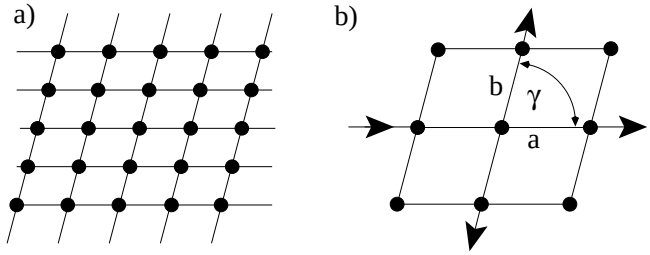

Figure 4.1: A two-dimensional parallelogram lattice (a) and a finite array (b). The relevant parameters are the lattice constants (a,b) and the angle γ as well. Electrons can propagate along the leads connecting the junctions (full circles) [78].

When an electron is propagating in a 2D mesoscopic system in the presence of Rashba spin-orbit interaction and a magnetic field $\mathbf{B}$, we can write the two-dimensional Hamiltonian in the following form:

$$H = \frac{1}{2m^*}(\mathbf{P} - e\mathbf{A})^2 + \alpha\sigma \cdot \mathbf{E} \times (\mathbf{P} - e\mathbf{A}) + \mu\sigma \cdot \mathbf{B}, \tag{4.1}$$

where $\mathbf{A}$ is the vector potential, α is the Rashba-type spin-orbit interaction (SOI) constant, $\mathbf{E}$ and $\mathbf{B}$ are pointing in the $\mathbf{e}_z$ direction (perpendicular to the plane in which carriers propagate) [79].

In the current study, the perpendicular magnetic field $\mathbf{B}$ is zero, thus the Zeeman term [the last one in (4.1)] is missing. We can choose $\mathbf{A} = 0$, since $\mathbf{B} = \nabla \times \mathbf{A}$ holds trivially in this case. Thus the new Hamiltonian reads

$$H = H_{kin} + H_{SO} = \frac{1}{2m^*}\mathbf{P}^2 + \alpha\sigma \cdot (\mathbf{E} \times \mathbf{P}). \tag{4.2}$$

This operator contains the kinetic (H_{kin}) and the spin-orbit interaction (H_{SO}) terms.

The general form of spin-dependent and dimensionless Hamiltonian which describes electrons in a narrow quantum wire in the $x-y$ plane can be written as

$$\widetilde{H} = \frac{H}{\hbar\Omega} = \left(-i\frac{\partial}{\partial s} + \frac{\omega}{2\Omega}\mathbf{n}(\sigma \times \mathbf{e}_z)\right)^2 - \frac{\omega^2}{4\Omega^2}, \tag{4.3}$$

where the unit vector $\mathbf{n} = (\cos(\gamma), \sin(\gamma), 0)$ points to the chosen positive direction along the wire and we defined the characteristic kinetic energy $\hbar\Omega = \hbar^2/2m^*a^2$ (with a being one of the lattice constants, see Fig. 4.1). The strength of the SOI is given by $\omega/\Omega = \alpha/a\Omega$, where the Rashba parameter α is function of E_z [79], and s denotes the dimensionless length variable along the lead measured in units of a [78].

We shall use the spin-operator σ_γ that is given by

$$\sigma_\gamma = \mathbf{n}(\sigma \times \mathbf{e}_z) = \begin{pmatrix} 0 & -ie^{-i\gamma} \\ ie^{i\gamma} & 0 \end{pmatrix}. \tag{4.4}$$

The Rashba spin-orbit coupling term can be transformed into $\frac{\omega}{2\Omega}\sigma_\gamma$. We use the following useful form of the Hamiltonian during the derivation of the probability current density:

$$\begin{aligned} \widetilde{H} &= {\mathcal{P}_s}^2 + \frac{\omega}{2\Omega}\mathcal{P}_s\sigma_\gamma + \frac{\omega}{2\Omega}\sigma_\gamma\mathcal{P}_s \\ &= \left(-i\frac{\partial}{\partial s}\right)^2 + \frac{\omega}{2\Omega}\left(-i\frac{\partial}{\partial s}\right)\sigma_\gamma + \frac{\omega}{2\Omega}\sigma_\gamma\left(-i\frac{\partial}{\partial s}\right). \end{aligned} \tag{4.5}$$

As one can check easily, the operators $\mathcal{P}_s$ and σ_γ are Hermitian.

4.2 Spectrum and eigenspinors of Hamiltonian with SOI term

The description of the motion of an electron which can propagate in a quantum wire requires the knowledge of the spectrum and eigenstates of the single electron Hamiltonian (4.3). Due to the spin dependence, this Hamiltonian can be written in a matrix form:

$$\widetilde{H} = \begin{pmatrix} -\frac{\partial^2}{\partial s^2} & -\frac{\omega}{\Omega} e^{-i\gamma} \frac{\partial}{\partial s} \\ \frac{\omega}{\Omega} e^{i\gamma} \frac{\partial}{\partial s} & -\frac{\partial^2}{\partial s^2} \end{pmatrix}. \tag{4.6}$$

A simple plane-wave basis can be used to reformulate the new matrix elements of $\widetilde{H}$. The chosen basis can be written in column vector form as follows

$$|+\rangle = \begin{pmatrix} e^{iks} \\ 0 \end{pmatrix}, \quad |-\rangle = \begin{pmatrix} 0 \\ e^{iks} \end{pmatrix}. \tag{4.7}$$

Let us note that this basis is complete and orthonormal in the spinor sense. If we calculate the matrix elements, we obtain

$$\widetilde{H} = \begin{pmatrix} k^2 & -i\frac{\omega}{\Omega} e^{-i\gamma} k \\ i\frac{\omega}{\Omega} e^{i\gamma} k & k^2 \end{pmatrix}. \tag{4.8}$$

Now solve the so called characteristic (or secular) equation. The resulting eigenenergies of $\widetilde{H}$ are

$$\varepsilon_{\pm} = k^2 \pm \frac{\omega}{\Omega}|k|. \tag{4.9}$$

Clearly, when the strength of the SOI equals zero, we reobtain the case of a free quantum particle. Having obtained the eigenvalues, the calculation of the eigenspinors is an easy problem. We should solve the following system of linear equations:

$$\left(\widetilde{H} - \varepsilon_{\pm} I\right) |\psi^{\pm}\rangle = \underline{0}, \tag{4.10}$$

where $\underline{0}$ is the zero column vector of length 2. The normalized eigenspinors $|\psi^{+}\rangle$ and $|\psi^{-}\rangle$ which correspond to the eigenenergies ε_{+} and ε_{-} are

$$|\psi^{\pm}\rangle = \frac{1}{\sqrt{2}} e^{iks} \begin{pmatrix} 1 \\ \pm i e^{i\gamma} \end{pmatrix} = e^{iks} |\gamma^{\pm}\rangle, \tag{4.11}$$

where the wave number k is measured in units of $1/a$ and the azimuthal angle γ corresponds to the direction of the unit vector $\mathbf{n}$ (see Fig. 4.1). Additionally, as we can check,

$$\sigma_{\gamma} |\gamma^{\pm}\rangle = \pm |\gamma^{\pm}\rangle. \tag{4.12}$$

Note that the spectrum of $\widetilde{H}$ forms a continuum independently from the direction of the wire. Owing to the SOI term in the Hamiltonian the spin direction of the eigenspinors depend on the spin-orbit coupling strength. For given energy the eigenvalue is fourfold degenerate due to the two possible propagation and spin directions.

4.3 Spinor valued wavefunction

In order to describe quantum mechanical properties, we consider the low temperature range. At low temperatures, the conductance is determined entirely by electrons with energy close to the Fermi level [28]. Therefore we are to determine the spinor valued wavefunction of an electron corresponding to the Fermi energy.

In the previous section, we have already calculated the eigenenergies $\varepsilon_\pm$ of the Hamiltonian (4.3). The next step is to solve the quadratic equations for wavenumbers

$$\varepsilon_\pm = k_F^2, \tag{4.13}$$

where the dimensionless Fermi energy is denoted by k_F^2. Here the equation $\varepsilon_+ - k_F^2 = 0$ will be discussed in detail; the second case $\varepsilon_- - k_F^2 = 0$ can be treated in a similar way.

By expanding the absolute vale, we can write

$$0 = k^2 + |k|\frac{\omega}{\Omega} - k_F^2 = \begin{cases} (+): & k^2 + k\frac{\omega}{\Omega} - k_F^2 = 0 \qquad \text{if } k \geq 0 \\ (-): & k^2 - k\frac{\omega}{\Omega} - k_F^2 = 0 \qquad \text{if } k < 0. \end{cases} \tag{4.14}$$

The solutions of the first equation are

$$k_{1,2}^{++} = -\frac{\omega}{2\Omega} \pm \sqrt{\frac{\omega^2}{4\Omega^2} + k_F^2}, \tag{4.15}$$

where the first superscript $+$ corresponds to the energy ε_+, while the second one shows which equation is solved from the system (4.14). In the following, we shall use the positive wavenumber

$$\kappa = -\frac{\omega}{2\Omega} + \sqrt{\frac{\omega^2}{4\Omega^2} + k_F^2}. \tag{4.16}$$

In a similar way we obtain

$$k_{1,2}^{+-} = \frac{\omega}{2\Omega} \pm \sqrt{\frac{\omega^2}{4\Omega^2} + k_F^2}. \tag{4.17}$$

For the sake of simplicity of formulas, we introduce

$$\widetilde{\kappa} = \frac{\omega}{2\Omega} + \sqrt{\frac{\omega^2}{4\Omega^2} + k_F^2}. \tag{4.18}$$

Using the notation above, we have the four eigenspinors that correspond to the degenerate eigenvalue k_F^2 :

$$|\psi_1\rangle = e^{i\kappa s}|\gamma^+\rangle, \tag{4.19}$$

$$|\psi_2\rangle = e^{-i\widetilde{\kappa} s}|\gamma^+\rangle, \tag{4.20}$$

$$|\psi_3\rangle = e^{-i\kappa s}|\gamma^-\rangle, \tag{4.21}$$

$$|\psi_4\rangle = e^{i\widetilde{\kappa} s}|\gamma^-\rangle. \tag{4.22}$$

That is, at the Fermi energy, an arbitrary spinor valued wave function can be written as

$$|\Psi\rangle(s) = \sum_{n=1}^{4} a_n|\psi_n\rangle, \tag{4.23}$$

where the coefficients a_n are complex probability amplitudes.

4.4 Derivation of spin-dependent probability current density

In this section we shall recall definitions and equations related to the probability density and also to the probability density current. Normalization of a state $\mid \Psi(t_0)\rangle$ means:

$$\langle \Psi(t_0) \mid \Psi(t_0)\rangle = \int |\Psi(\mathbf{r}, t_0)|^2 \, \mathrm{d}^3 r = 1, \tag{4.24}$$

where $\Psi(\mathbf{r}, t_0) = \langle \mathbf{r} \mid \Psi(t_0)\rangle$ is the wave function which is associated to the abstract state vector $\mid \Psi(t_0)\rangle$. Equation (4.24) means that the probability of finding the particle on the whole available domain is equal to 1. Conservation of the norm is expressed by the equation:

$$\langle \Psi(t) \mid \Psi(t)\rangle = \int |\Psi(\mathbf{r}, t)|^2 \, \mathrm{d}^3 r = \langle \Psi(t_0) \mid \Psi(t_0)\rangle = 1, \tag{4.25}$$

where $\mid \Psi(t)\rangle$ is the solution of the Schrödinger equation which corresponds to he initial state $\mid \Psi(t_0)\rangle$. As a consequence, the time evolution does not change the global probability of finding the particle all over the whole domain, which always remains equal to unity. Thus the quantity $|\Psi(\mathbf{r}, t)|^2$ is interpreted as the probability density [45]:

$$\rho(\mathbf{r}, t) = |\Psi(\mathbf{r}, t)|^2 . \tag{4.26}$$

Note that we use the character ρ in order to distinguish the probability density and the density operator, which is denoted by ϱ.

Although the integral of $\rho(\mathbf{r},t)$ over all the available spatial domain is unity, this does not mean that the probability density is independent of time and space. This situation is analogous to the one encountered in electrodynamics. Let us consider an isolated physical system, where charges are distributed in space according to the volume density of $\tilde{\rho}(\mathbf{r},t)$. The integral of $\tilde{\rho}(\mathbf{r},t)$ over all space is equal to the total charge. Conservation of electrical charge is valid, which is expressed locally by the continuity equation:

$$\frac{\partial}{\partial t}\rho(\mathbf{r},t)+\nabla\cdot\mathbf{J}(\mathbf{r},t)=0. \tag{4.27}$$

Global conversation of electrical charge is based on this equation: if the charge Q is contained in a fixed volume V varies over time, integration of (4.27) over V tells us that the closed surface F which confines V must be traversed by an electric current.

The analogous continuity equation in quantum mechanics states the conservation of probability. This can be written in dimensionless form as

$$\Omega\frac{\partial}{\partial\tau}\rho(s,\tau)+\frac{1}{a}\frac{\partial}{\partial s}J(s,\tau)=0, \tag{4.28}$$

where $\tau=\Omega t$. The probability current density without the presence of SOI can be found in textbooks. Our aim is to obtain it for the Hamiltonian given by Eq. (4.3).

The time derivative of the probability density can be written as

$$\frac{\partial}{\partial\tau}\rho=\left\langle\frac{\partial}{\partial\tau}\Psi\middle|\Psi\right\rangle+\left\langle\Psi\middle|\frac{\partial}{\partial\tau}\Psi\right\rangle. \tag{4.29}$$

The Schrödinger equation leads to

$$\left\langle\frac{\partial}{\partial\tau}\Psi\middle|\Psi\right\rangle=i\langle\widetilde{H}\Psi|\Psi\rangle, \tag{4.30a}$$

$$\left\langle\Psi\middle|\frac{\partial}{\partial\tau}\Psi\right\rangle=-i\langle\Psi|\widetilde{H}|\Psi\rangle. \tag{4.30b}$$

By inserting $\widetilde{H}$ we obtain

$$i\langle\widetilde{H}\Psi|\Psi\rangle=i\left\langle\left(-i\frac{\partial}{\partial s}\right)^2\Psi+\frac{\omega}{2\Omega}\left(-i\frac{\partial}{\partial s}\right)\sigma_\gamma\Psi+\frac{\omega}{2\Omega}\sigma_\gamma\left(-i\frac{\partial}{\partial s}\right)\Psi\middle|\Psi\right\rangle, \tag{4.31a}$$

$$-i\langle\Psi|\widetilde{H}|\Psi\rangle=-i\left\langle\Psi\middle|\left(-i\frac{\partial}{\partial s}\right)^2+\frac{\omega}{2\Omega}\left(-i\frac{\partial}{\partial s}\right)\sigma_\gamma+\frac{\omega}{2\Omega}\sigma_\gamma\left(-i\frac{\partial}{\partial s}\right)\middle|\Psi\right\rangle. \tag{4.31b}$$

Now let us transform the terms in the above equation. First, we study products which include the operator $\left(-i\frac{\partial}{\partial s}\right)^2=(-i\partial_s)^2$. We have

$$i\langle\mathcal{P}_s^2\Psi|\Psi\rangle-i\langle\Psi|\mathcal{P}_s^2|\Psi\rangle=-i\langle\partial_s^2\Psi|\Psi\rangle+i\langle\Psi|\partial_s^2|\Psi\rangle, \tag{4.32}$$

Since

$$\langle \partial_s^2 \Psi | \Psi \rangle = \partial_s \langle \partial_s \Psi | \Psi \rangle - |\partial_s \Psi|^2, \tag{4.33a}$$

$$\langle \Psi | \partial_s^2 | \Psi \rangle = \partial_s \langle \Psi | \partial_s | \Psi \rangle - |\partial_s \Psi|^2, \tag{4.33b}$$

Eq. (4.32) has been transformed into a form that will turn out to be useful in the following:

$$i\langle \mathcal{P}_s^2 \Psi | \Psi \rangle - i\langle \Psi | \mathcal{P}_s^2 | \Psi \rangle = -\frac{\partial}{\partial s} \left[\langle \mathcal{P}_s \Psi | \Psi \rangle + \langle \Psi | \mathcal{P}_s | \Psi \rangle \right] = -2\partial_s \, \mathrm{Re}(\langle \mathcal{P}_s \rangle_\Psi). \tag{4.34}$$

Now let us focus on terms containing the spin operator σ_γ. This is not a difficult problem because the previous method can also be used in this case. Let us recognize the following relations using Eqs. (4.31a,4.31b):

$$-\left\langle \frac{\omega}{2\Omega} \partial_s \sigma_\gamma \Psi + \frac{\omega}{2\Omega} \sigma_\gamma \partial_s \Psi \middle| \Psi \right\rangle = -\partial_s \left\langle \frac{\omega}{2\Omega} \sigma_\gamma \Psi \middle| \Psi \right\rangle + \left\langle \frac{\omega}{2\Omega} \sigma_\gamma \Psi \middle| \partial_s \Psi \right\rangle, \tag{4.35a}$$

$$-\left\langle \Psi \middle| \frac{\omega}{2\Omega} \partial_s \sigma_\gamma + \frac{\omega}{2\Omega} \sigma_\gamma \partial_s \middle| \Psi \right\rangle = -\partial_s \left\langle \Psi \middle| \frac{\omega}{2\Omega} \sigma_\gamma \middle| \Psi \right\rangle + \left\langle \partial_s \Psi \middle| \frac{\omega}{2\Omega} \sigma_\gamma \middle| \Psi \right\rangle. \tag{4.35b}$$

Note that the scalar products which include $|\partial_s \Psi\rangle$ or its adjoint, give a complex number whose real part is equal to zero. That is,

$$\left\langle \frac{\omega}{2\Omega} \sigma_\gamma \Psi \middle| \partial_s \Psi \right\rangle + \left\langle \partial_s \Psi \middle| \frac{\omega}{2\Omega} \sigma_\gamma \middle| \Psi \right\rangle = 2 \, \mathrm{Re} \left(\left\langle \partial_s \Psi \middle| \frac{\omega}{2\Omega} \sigma_\gamma \middle| \Psi \right\rangle \right) = 0. \tag{4.36}$$

Furthermore,

$$-\partial_s \left[\left\langle \frac{\omega}{2\Omega} \sigma_\gamma \Psi \middle| \Psi \right\rangle + \left\langle \Psi \middle| \frac{\omega}{2\Omega} \sigma_\gamma \middle| \Psi \right\rangle \right] = -2\partial_s \, \mathrm{Re} \left(\left\langle \frac{\omega}{2\Omega} \sigma_\gamma \right\rangle_\Psi \right). \tag{4.37}$$

At this point of our calculation, the function $-a\Omega \frac{\partial}{\partial \tau} \rho$ can be given as follows

$$-a\Omega \frac{\partial}{\partial \tau} \rho = 2a\Omega \partial_s \, \mathrm{Re} \left(\left\langle \mathcal{P}_s + \frac{\omega}{2\Omega} \sigma_\gamma \right\rangle_\Psi \right). \tag{4.38}$$

Recalling the continuity equation, we see that the form of the dimensionless probability current density in the presence of Rashba spin-orbit interaction is

$$\widetilde{J}_\gamma = \frac{m^* a}{\hbar} J_\gamma = \langle j_\gamma \rangle_\Psi, \tag{4.39}$$

where the operator j_γ is defined by

$$j_\gamma = j_s + j_{SOI} = \mathcal{P}_s + \frac{\omega}{2\Omega} \sigma_\gamma. \tag{4.40}$$

Note that $J_\gamma(s)$ is often called *spin-dependent* probability current density. Clearly, if the strength of the SOI, ω/Ω, equals zero, we reobtain the case of a free particle.

Some useful properties of j_γ should also be emphasized in this section. First of all, since $\mathcal{P}_s = \mathcal{P}_s^\dagger$ and $\sigma_\gamma = \sigma_\gamma^\dagger$, j_γ is also a self-adjoint operator. In addition, we can also calculate the action of $j_\gamma|\psi_k\rangle$ on the eigenstates given by (4.19)-(4.22):

$$j_\gamma|\psi_1\rangle = \left(\kappa + \frac{\omega}{2\Omega}\right)|\psi_1\rangle = \sqrt{\frac{\omega^2}{4\Omega^2} + k_F^2}\,|\psi_1\rangle, \tag{4.41}$$

$$j_\gamma|\psi_2\rangle = \left(-\widetilde{\kappa} + \frac{\omega}{2\Omega}\right)|\psi_2\rangle = -\sqrt{\frac{\omega^2}{4\Omega^2} + k_F^2}\,|\psi_2\rangle, \tag{4.42}$$

$$j_\gamma|\psi_3\rangle = \left(\widetilde{\kappa} - \frac{\omega}{2\Omega}\right)|\psi_3\rangle = \sqrt{\frac{\omega^2}{4\Omega^2} + k_F^2}\,|\psi_3\rangle, \tag{4.43}$$

$$j_\gamma|\psi_4\rangle = \left(-\kappa - \frac{\omega}{2\Omega}\right)|\psi_4\rangle = -\sqrt{\frac{\omega^2}{4\Omega^2} + k_F^2}\,|\psi_4\rangle. \tag{4.44}$$

That is, the states $|\psi_k\rangle$ are eigenspinors also of the operator j_γ with eigenvalues $\pm\sqrt{\frac{\omega^2}{4\Omega^2} + k_F^2}$.

4.5 Band structure of an infinite superlattice

In order to find an eigenstate for the whole geometry, the solutions have to satisfy the Griffith's boundary conditions [80]. In short, the wavefunctions have to be continuous at the junctions. Additionally, in accordance with the principle of conservation of probability, we also require the net spin current density to be zero at these points.

As we can see in Fig. (4.1), the building blocks of our nanoscale structure are narrow quantum wires. The properties of the arrays are determined by geometrical parameters (lattice constants a, b and azimuthal angle γ). The whole system is a periodic lattice structure. The form of the eigenfunctions of the spin-dependent Hamiltonian (4.3) can be given as

$$\Psi_{n,\mathbf{k}}(\mathbf{r}) = u_{n,\mathbf{k}}(\mathbf{r})\exp(i\mathbf{k}\mathbf{r}), \tag{4.45}$$

where the quantum number n is called the band index and the functions $u_{n,\mathbf{k}}(\mathbf{r})$ are lattice-periodic, $u_{n,\mathbf{k}}(\mathbf{r}+\mathbf{R}) = u_{n,\mathbf{k}}(\mathbf{r})$ ($\mathbf{R}$ denotes an arbitrary lattice vector). This kind of wavefunctions (4.45) is referred to as spinor valued Bloch waves [81]. Keeping in mind that we are considering an infinite superlattice, we have to use periodic (Born - von Kármán) boundary conditions.

The consequence of the periodicity is an energy spectrum with a specific structure: e.g., there will be no solutions in certain energy ranges. To determine the band structure we should calculate the triplets $\{E(\mathbf{k}), k_1, k_2\}$ that correspond to Bloch-wave eigenspinors of the problem. As usually, we find that the dispersion relation $E(\mathbf{k})$ is a multivalued function of the two-dimensional wave vector $\mathbf{k} = (k_1, k_2)$, and we can identify

infinitely many surfaces in this function. These surfaces (bands) do not overlap unless there is a symmetry induced degeneracy.

During our work we assumed that the motion of electrons corresponds to single mode propagation, which is a reasonable approximation for narrow conducting wires. Taking the finite width of these electron waveguide into account leads to qualitatively the same results, with considerably increased computational costs. Additionally, the subbands related to the transversal modes have already been analyzed in detail (see, e.g., Ref. [28]), thus using the current model we can focus on the band structure induced by the periodicity of the lattice.

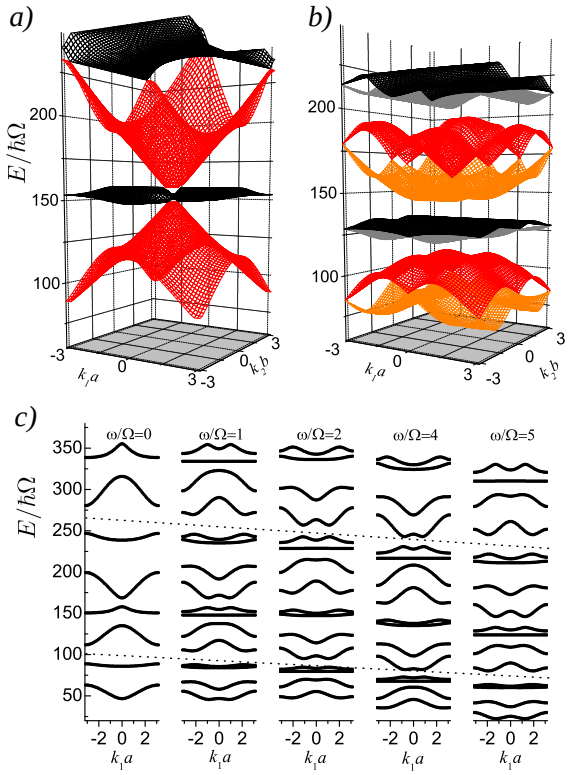

Figure 4.2: Band structure of a rectangular lattice ($\gamma = \pi/2$ and $b/a = 1.03$) for different SOI strength values: $\omega/\Omega = 0.0$ in panel a), $\omega/\Omega = 5.0$ for panel b). Cross sections at $k_2 b = 1.0$ are shown for several additional values of the SOI strengths in panel c). The thin dotted lines guide the eyes by showing the energy range for which the bands are "essentially the same," i.e., they continuously transform into each other when the SOI strength is changed. Note that the levels between the dotted lines correspond to the two dimensional plots in panels a) and b) [78].

For a given two-dimensional wave vector $\mathbf{k} = (k_1, k_2)$ the energy eigenvalues can be written as $E_{n,m}(\mathbf{k})$, where the band indices n and m are related to the spatial periodicity of the plane waves $\exp(\mathbf{k} \cdot \mathbf{r})$ in the unit cell along the two lattice directions. According to the dispersion relation, the energies scale essentially with the square of n/a and m/b. The same phase relations at the boundaries can hold with, e.g., n and $n+1$ waves along the direction of one of the lattice vectors in the unit cell, and the dominant contribution (omitting SOI corrections) of these solutions to the energy is proportional to n^2/a^2 and $(n+1)^2/a^2$. Consequently, the bands have in general a double quasiperiodic structure. In the case of $a \approx b$, a repetition of a small number of $E_{n,m}(\mathbf{k})$ surfaces provides the complete band structure.

We can see four bands for a rectangular infinite lattice structure with $b/a = 1.03$ and the SOI strength is equal to zero in panel a) of Fig. 4.2. The energy is measured in units of $\hbar\Omega$, which, for $a = 10\,\mathrm{nm}$ in InAlAs/InGaAs based heterostructures [82, 83] is on the order of meV. The four bands seen in this figure are quasiperiodically repeated. The lattices shown in Fig. 4.1 have unit cells with four distinct boundary points, namely, four leads connect them to the neighboring cells. The oppositely situated boundary points are equivalent in a crystal, thus any measurable physical quantity has to have the same value at these points. Particularly, the currents carried by the opposite leads should be the same. That is, the sign of the currents at the four leads can be written schematically as $++++$, $+-+-$, $-+-+$, $----$ (where the leads that correspond to the $\pm$ signs follow each other in a clockwise order). The four bands seen in Fig. 4.2 a) correspond to these four possible current configurations. For nonzero SOI, all these bands split into two due to the spin dependence of the interaction and as it is shown in Fig. 4.2, the strength of the SOI modifies considerably both the position and the width of the allowed/forbidden bands (bandgaps).

In Fig. 4.2 c) cross sections of the band structure are plotted for different values of the SOI which clearly shows the gradual splitting of the levels as the SOI gets stronger. Additionally, when we identify the bands that continuously evolve from/into each other when the strength of the SOI (characterized by the parameter ω in Eq. 4.3) is changed, we notice an overall decrease in the energies (see the dotted lines in Fig. 4.2(c)). This is due to the SOI induced splitting of the lowest band, resulting in a decrease in the lowest possible energy when ω increases.

The band structure strongly depends on the underlying geometry as illustrated in Fig. 4.3. This emphasizes that besides the tunability of the band structure by external gate voltages (that modify the strength of the SOI), the geometry is also an important additional degree of freedom.

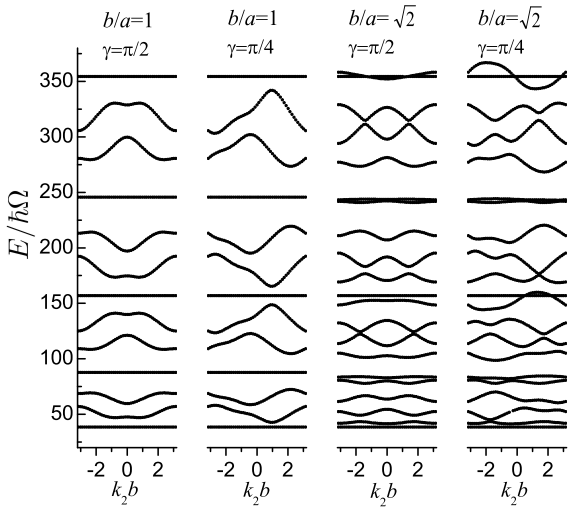

Figure 4.3: The texture of the bands for different lattice geometry parameters. The relevant parameters are $\omega/\Omega = 1.0$, $k_1 a = 1.0$ [78].

4.6 Conductance of finite systems

Results based on infinite structures usually have implications also on large but finite systems. Now we calculate the conductance of arrays consisting of $N \times N$ unit cells (see Fig. 4.1(b)) using the Landauer-Büttiker formula [26, 28]

$$G(E) = \frac{e^2}{h} \sum_n \left[T_\uparrow^n(E) + T_\uparrow^n(E) \right], \tag{4.46}$$

where the sum runs over the possible outputs. $T_\uparrow^n(E)$ ($T_\downarrow^n(E)$) refers to the transmission probability at the relevant output for spin-up (spin-down) input in the chosen quantization direction. These probabilities are calculated by solving the eigenvalue problem for the whole network at a given energy E imposing the appropriate boundary conditions, e.g., at the input we have a spin-up (or spin down) incoming wave and a possible reflected one while at the outputs only outgoing waves appear.

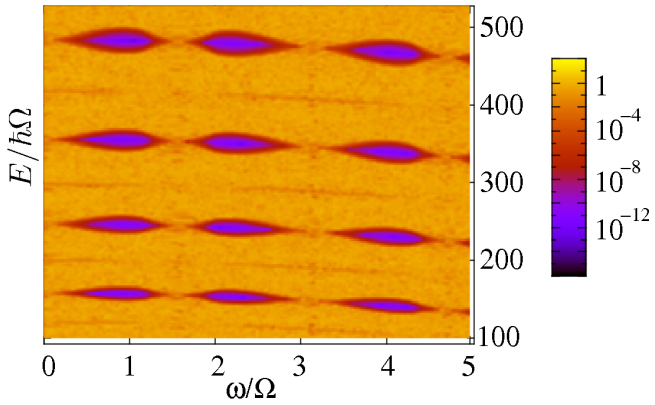

Figure 4.4: Contour plot of the conductance measured in units of $G_0 = e^2/h$ for a 15×15 array with $b/a = 2$, $\gamma = \pi/2$ as a function of the energy and the SOI strength. We can observe non-conducting almond-shaped domains [78].

Figure (4.4) shows a contour plot of the conductance as a function of the energy and the SOI strength for a rectangular 15×15 array. We clearly notice the appearance of stripes (the position and width of which depend on the SOI strength) of zero conductance. In these regions the array is completely opaque for the electrons. Additionally, for the 15×15 array, these nonconducting stripes [84] coincide with the bandgaps obtained from a calculation assuming an infinite structure with the same local geometry. In order to visualize this fact, we projected the band structure on the energy axis to obtain the limits between allowed and forbidden energy regions (see the gray areas in Fig. (4.5)). Already for a 3×3 network, we can see some signatures in $G(E)$ of the band structure but for a 7×7 array the positions of the zero-conductance energy ranges are practically the same as the bandgaps. Having introduced random, spin-dependent scattering centers as it is discussed in Refs. [84] and [85] (see also Eqs. 5.4, 5.5), we observed that the widths of the bandgaps decrease only by 10%, even when dephasing is so strong, that 100% degree of spin-polarization (input) drops to 20% (outputs).

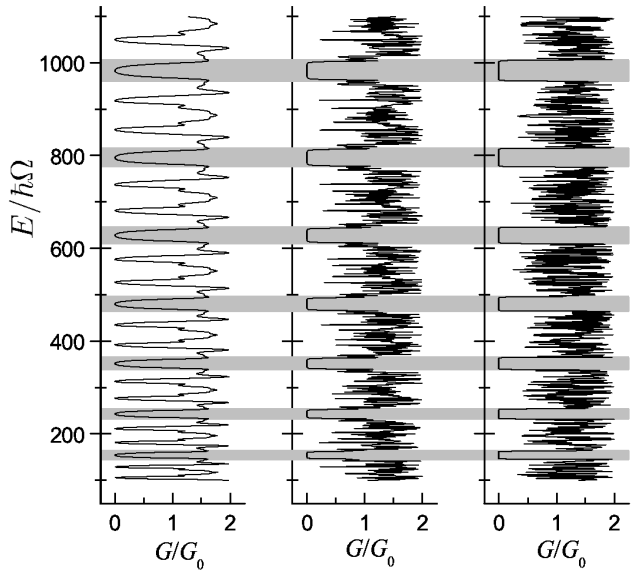

Figure 4.5: The conductance of 3×3, 7×7, 15×15 arrays, where the light gray shading indicates the energy gaps in the corresponding infinite superlattice [78].

Chapter 5

SOI-controlled modulation of finite temperature conductance

Now let us extend the calculation of the conductance of finite arrays to the case of finite temperature. That is, we assume, that the superlattice is connected to thermal reservoirs and the incoming electrons are described by a mixed state. Thus, the input wavefunction is not monoenergetic. It follows that the (unnormalized) output spinor valued wavefunction is related to the input energy E, in thermal equilibrium at temperature T, the output density operator can be written in the following form:

$$\varrho_{out}(T) = \int p(E,T)|\Psi_{out}(E)\rangle\langle\Psi_{out}(E)|\mathrm{d}E, \tag{5.1}$$

where the output spinor is denoted by $|\Psi_{out}(E)\rangle$ and $p(E,T)$ is equal to $-\frac{\partial f(E)}{\partial E}$. Obviously, for electrons

$$f(E) = \frac{1}{e^{\frac{(E-E_F)}{kT}}+1}. \tag{5.2}$$

Note that this expression corresponds to the Landauer-Büttiker formula for the conductance at finite temperature and low bias [28]. Consequently, the conductance measured in units of e^2/h is equal to the sum of the trace of $\varrho_{out}(T)$ for two oppositely polarized inputs.

Conductance as a function of temperature is shown in Fig. 5.2 for a 7×7 array and for values of the SOI strength where bandgaps have maximal and minimal widths (the latter is zero, see Fig. 5.1). In order to see the most important low temperature effect, the size of the network is chosen such that E_F is situated in the middle of a bandgap for nonzero SOI. (For $\omega = 0$, when there are no bandgaps at all, we use the same value of E_F, which is now obviously an allowed energy in the conduction band.) For nonzero SOI, until the width of the temperature broadened input is below that of the bandgap, conductance is practically zero. (See the left-hand side inset in Fig. 5.2).

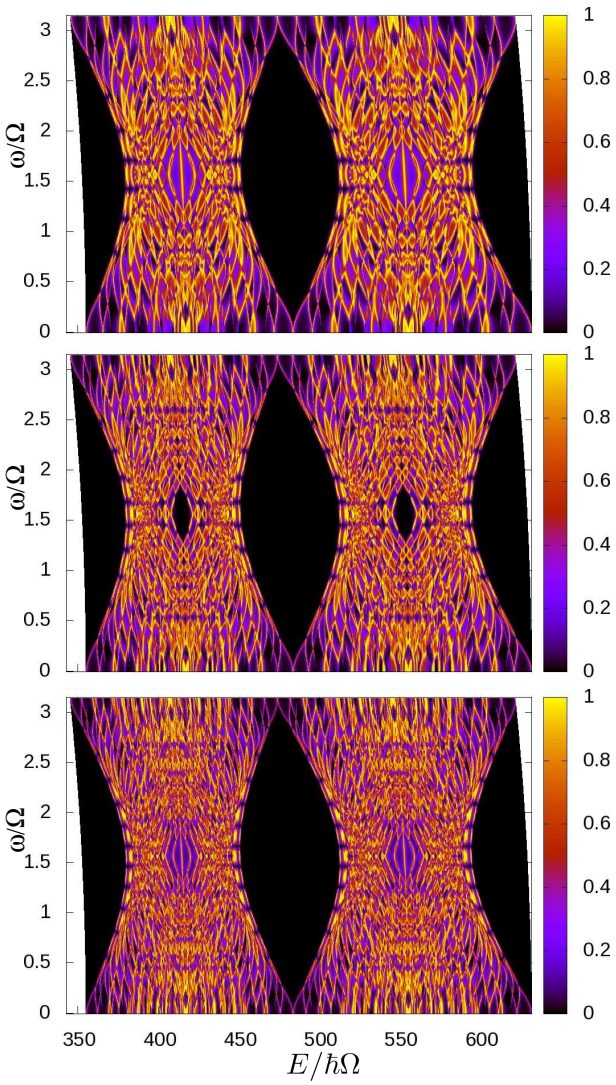

Figure 5.1: The set of these figures shows the conductance (in units of $2e^2/h$) of rectangular arrays of different sizes (from top to bottom: $N = 9, 11, 13$) as a function of the input energy and the strength of the SOI. Note the SOI-dependent, large almond shaped minima that are directly related to the bandgaps [86].

This low temperature effect is not particularly surprising, the most important issue here is that in contrast to smaller interference devices (like single quantum rings, where zero conductance appears only at discrete points), in the current case we have finite energy ranges with negligible transmission probabilities. Consequently, conductance modulations are still observable at finite (but low) temperatures as well.

The most remarkable feature seen in Fig. 5.2 is the constant high temperature conductance for the two different SOI strength values. Let us note that this high temperature limit is found to be independent from the value of E_F, it is determined solely by the SOI strength. In the following we use the term 'high temperature conductance' for this limit, which is well defined in the framework of the model. To be concrete, we note that for InAlAs/InGaAs based heterostructures with $a = 50\,\mathrm{nm}$, the value $kT/\hbar\Omega = 100$ corresponds to $T = 40\,\mathrm{K}$.

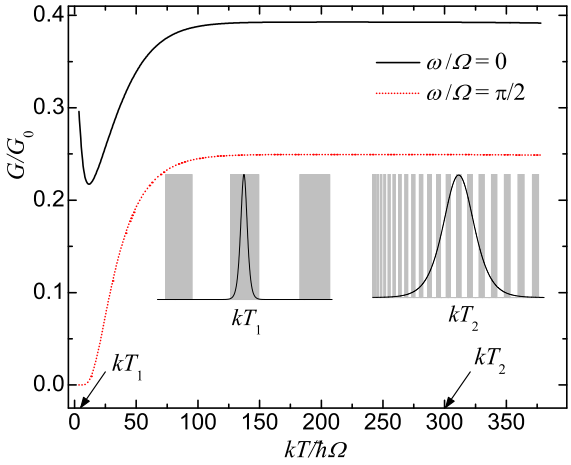

Figure 5.2: Temperature dependent conductance (measured in units of $G_0 = 2e^2/h$) of a 7×7 rectangular array for two different values of the spin-orbit interaction (SOI) strength. The insets show the temperature broadened input and the band scheme (for $\omega/\Omega = \pi/2$) where gray shading corresponds to the bandgaps. In the absence of SOI, when $\omega/\Omega = 0$, there are no bandgaps. For InAlAs/InGaAs based heterostructure with $a = 50\,\mathrm{nm}$, $kT/\hbar\Omega = 100$ is equivalent with a temperature of $40\,\mathrm{K}$ [86].

In order to see the physical reasons for the appearance of a constant high temperature conductance, first we recall the quasiperiodicity (as a function of energy) of the band scheme. More precisely, energy bands are periodic as a function of $\sqrt{E}$, which is proportional to the input wave number. For high enough temperatures (see the right-hand side inset in Fig. 5.2), the distribution $p(E,T)$ in Eq. (5.1) is a slowly varying function within a single period of the allowed/forbidden energy ranges. Therefore we may split

the integral appearing in Eq. (5.1) into an infinite sum over the consecutive periods in the band structure

$$\varrho_{out}(T) \approx \sum_n p(E_n, T) \int_{E_{n1}}^{E_{n2}} |\Psi_{out}(E)\rangle\langle\Psi_{out}(E)| \mathrm{d}E, \tag{5.3}$$

where E_{n1} (E_{n2}) is the beginning (end) of the nth period of the band scheme. Note that the slowly varying distribution has been moved in front of the integral, and we may take $E_n = (E_{n1} + E_{n2})/2$. This approximation is valid only for high temperatures. Conductance in this limit is not related to the fine structure of the band scheme, it is rather an overall property. Additionally, due to the periodicity of the band scheme, it is found to be sufficient to focus on a single period, evaluate the corresponding integral in the sum given by Eq. (5.3) and finally renormalize properly. According to our calculations, the choice of the one period long part of the band scheme to be investigated is indeed irrelevant here, and the approximation above leads to the numerically exact high temperature limit within a relative error below 5%.

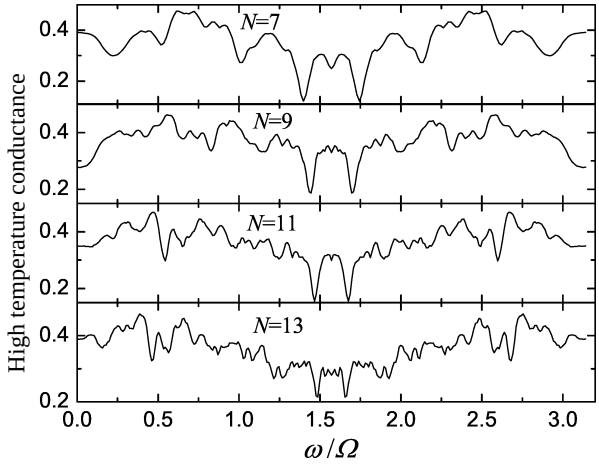

Figure 5.3: High temperature conductance (see Fig. 5.2) of $N \times N$ arrays as a function of the SOI strength. (Conductance is measured in units of $G_0 = 2e^2/h$.) [86]

The results of the calculations based on this approximation are shown in Fig. (5.3). The general behavior we expect is that for zero SOI, when there are no bandgaps at all, conductance is considerably higher in the high temperature limit than for cases when SOI induced bandgaps are present. As we can see, although the minima and maxima of the high temperature conductance do not correspond precisely to the widths of the bandgaps (e.g., conductance minima are not at $\omega/\Omega = \pi/2$), i.e., there are size dependent interference effects, the overall trend is the same as discussed above. As we shall see

in the next section, dephasing effects average out the interference related fringes in this graph, but leave the band scheme controlled phenomena practically unchanged.

5.1 Dephasing effect: scatterers in nanowires

There are several dephasing effects which change the coherent behavior of a quantum system and quantum interference phenomena are extremely sensitive to these dephasing mechanisms. Promising spintronic [3] devices can be fabricated from, for example InAlAs/InGaAs based semiconductor heterostructures [67]. We have already discussed that the 2-DEG has high mobility of charge carriers which is an important parameter from the viewpoint of ballistic transport. As we have seen, the mobility in a 2-DEG is decreasing significantly with the concentration of different impurities. Consequently, quantum transport phenomena can die out in the presence of scattering centers which are realized as impurities.

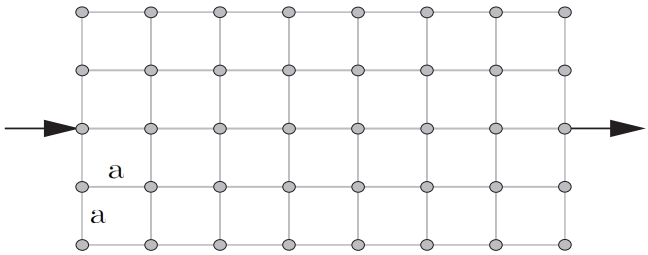

Figure 5.4: Two-dimensional rectangular array with a lattice constant denoted by a. The electrons can propagate freely in the input and output leads. Wires in which spin-orbit interaction (SOI) is present, are indicated by gray color.

In the current section, we shall introduce random scatterers with tuneable strength. We take their effect into account by an additional potential

$$U^{(2)}_{scatt}(\mathbf{r}) = \sum_n \mathbf{U}_n(D)\delta(\mathbf{r} - \mathbf{r}_n), \tag{5.4}$$

where $\mathbf{U}_n(D)$ denotes a 2×2 diagonal matrix. It has two independent random diagonal elements $U_{n1}(D)$ and $U_{n2}(D)$. Figure 5.4 shows the investigated nanoscale system in which the junctions are denoted by full circles. The Dirac-δ scatterers are situated at these junctions. Details of tunneling through a single delta-barrier can be found in Ref. [15]. The probability for the diagonal elements of matrix $\mathbf{U}_n(D)$ to have a value in a small interval around u is given by $p(u)\mathrm{d}u$, where $p(u)$ represents a normal distribution:

$$p(u) = \frac{1}{D\sqrt{2\pi}} \exp\left(-\frac{u^2}{2D^2}\right), \tag{5.5}$$

where D corresponds to root-mean-square deviation. Let us note that we can interpret this model also as dephasing due to random magnetic impurities at the junctions.

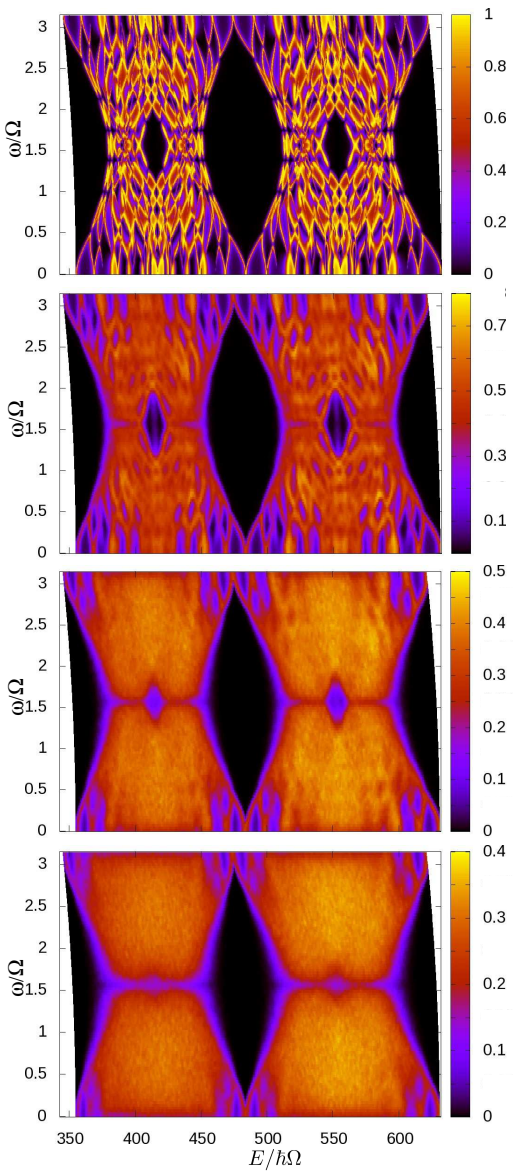

Figure 5.5: Conductance of a 7×7 rectangular array for different dephasing strengths. From top to bottom: $D/\hbar\Omega = 0, 10, 20, 30$, and the conductance is measured in units of $G_0 = 2e^2/h$ [86].

In this way, by tuning D we can model weak disturbances (small D) as well as frequent scattering events which will completely change the character of the transport process (corresponding to large values of D). Additionally, even in the presence of the spin-dependent Dirac-δ peaks, we can use Griffith's boundary conditions at the junctions, and the resulting equations are still linear. When, after M_c computational runs, the estimated

output density operator $\varrho_{out}(D)$ converges for a given input, we have all the possible information needed to describe the effects resulting from the disturbances characterized by the variable D. Similarly to the temperature dependent case, $\varrho_{out}(D)$ is not normalized, we can consider it as a conditional density operator that describes the state of the electron if it is transmitted at all. Using the transmission probability T, we have $Tr[\varrho_{out}(D)] = T$.

As a first application of the above method, we calculate the conductance of a given array as a function of the input energy and the SOI strength for different values of D. As we can see in Fig. 5.5, when dephasing gets stronger, the interference patterns gradually disappear, but the large, almond-shaped minima (seen already in Fig. 5.1), that are related to the bandgaps, survive. It is worth mentioning, that the average conductance decreases for larger values of D, in accordance with our expectations.

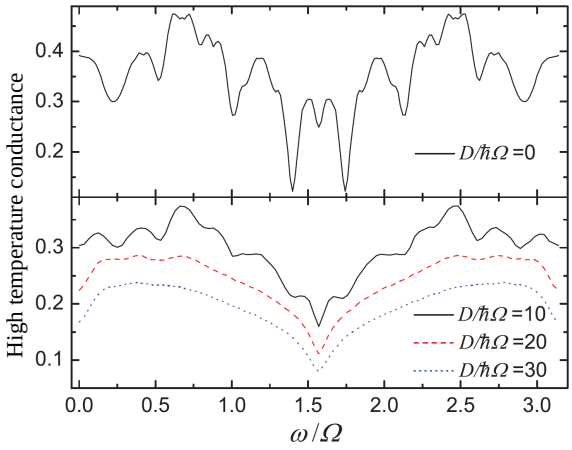

Figure 5.6: SOI strength dependence of the high temperature conductance (in units of $G_0 = 2e^2/h$) of a 7×7 array for different dephasing strengths [86].

Combining dephasing effects with the method described in the previous section, high temperature conductance can be calculated also in the presence of scatterers with different strengths. A representative set of results is shown in Fig. 5.6. As we can see, due to the fact that bandgap related conductance minima, shown in Fig. 5.5, are more stable against dephasing than finite size related interference patterns, high temperature conductance is still strongly modulated in the presence of moderate dephasing. In order to quantify this modulation, let us introduce the visibility

$$I = \frac{G_{max} - G_{min}}{G_{max} + G_{min}}, \tag{5.6}$$

where G_{max} and G_{min} are identical with maximal and minimal spin-dependent high temperature conductance. Evidently, the function I depends on the dephasing strength D

through G_{max} and G_{min}. This dependence is shown in Fig. 5.7, which can be considered as a visual summary of the current part.

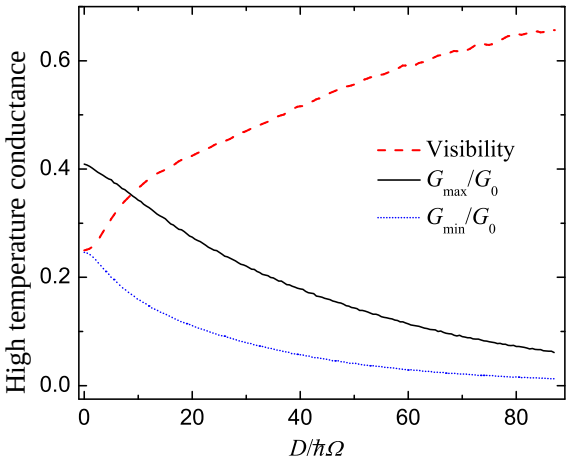

Figure 5.7: Maximal and minimal high temperature conductance is shown for a 7×7 array and different dephasing strengths. The corresponding visibility of the band scheme related conductance modulation ($G_0 = 2e^2/h$) [86] is also shown.

As we have seen in Fig. 5.7, the spin-orbit interaction induced high temperature conductance modulation is still visible for relatively high values of dephasing strength, even when the G_{max} drops below 25% of its value at $D = 0$. Moreover, we can also see, increasing visibility has small practical relevance when the conductance has actually vanished. However, it is remarkable and promising from the viewpoint of practical applications that even in the presence of moderate dephasing and strong thermal fluctuations, the experimentally tunable SOI strength can control the conductance properties.

5.2 Possible spintronic applications

We identified possible applications which can be useful for spintronic nanodevices. For example, when $a \approx b$ there are very narrow bands, the width and position of which can be controlled by the SOI strength. For InAlAs/InGaAs based heterostructures and a 9×9 network with $\gamma = \pi/2$, $a = 10\,\mathrm{nm}$, and $b/a = 1.01$, an energy range around $2\,\mathrm{meV}$ is transmitted in the middle of a $20\,\mathrm{meV}$ wide bandgap.

Conductance of finite arrays at nonzero temperatures has also been calculated using the appropriate Landauer-Büttiker formula. The most interesting effect in this context is related to the positions of the almond-shaped minima in Fig. 4.4 and Fig. 5.1: as we can see, the width of all the bandgaps can be controlled simultaneously by the SOI strength. Therefore even when the input has a broad energy distribution (high temperature limit), conductance is still modulated by the SOI. The conductance changes with 20% of its average value when the SOI strength is varied in an experimentally achievable range. For a 13×13 square network the modulation is around 40%. (Note that in the framework of our model, at "high temperatures" transversal modes other than the ground state should not be excited. However, the physical reasons for the above result are valid also for multimode propagation.)

For non-square lattices the geometrical anisotropy leads to anisotropy in the band structure (see Fig. 4.3), and consequently also in the conductance properties. For a 9×9 lattice with $b/a = 2$, $\gamma = \pi/4$, the difference of the transmission probabilities in the x and y directions – depending on the SOI strength – can be zero, or as large as ± 0.8, so that the higher one is above 0.95.

Besides the SOI controlled phenomena discussed above, finite arrays can also perform various spin transformations. Apart from spin rotations that can also be done with smaller devices, the arrays considered here are also versatile spintronic devices: e.g., according to our calculations, the network described in the previous paragraph can deliver oppositely spin-polarized outputs from a completely unpolarized input, when the output leads are situated at the middle of the sides of the network (see Fig. 4.1(b)). Additionally, the spin-polarizing property can be combined with energy filtering, for the 9×9 network we discussed earlier ($\gamma = \pi/2,\ b/a = 1.01$) the degree of polarization at the output can be above 85%. Note that some of these spintronic properties are similar to that of ring arrays [73] and although in the current case the transmission probabilities are lower than unity (but still around 50%), now there is no need for a local modulation of the SOI strength, which is promising from the viewpoint of possible applications.

5.3 Conclusions

We have investigated the conductance properties of two-dimensional superlattices. The geometry of the structures and Rashba-type SOI play a crucial role in transport phenomena. We calculated the band structure of these artificial crystals, and showed that by changing the SOI strength in the experimentally achievable range, the band scheme can be modified qualitatively, e.g., forbidden energy ranges can become allowed and vice versa. Comparing the band structure with the conductance properties of finite systems, we found that already for relatively small arrays, forbidden bands are clearly seen in the conductance. Several possible applications were given, including strong modulation of the conductance at moderate temperatures, and a device that can deliver partially spin-polarized electrons with narrow energy distribution.

We have also studied high temperature conductance of finite size two-dimensional arrays in which the propagation of the electrons is determined by the interplay of the geometry and the spin-orbit interaction (SOI). It was shown that the SOI can strongly modulate the finite temperature conductance, and this effect is still present at high temperatures. We investigated how dephasing effects modify this result, and found it to be valid even when conductance is strongly suppressed due to scattering events.

Part III

Chapter 6

Effects of oscillating spin-orbit interaction

The main goal of this chapter is to give an overview of our results related to time-dependent phenomena. Specifically, we consider a time-dependent (oscillating) Rashba-type spin-orbit field that determines the conductance properties of nanostructures. As we shall see, the physical processes we observe in this system have analogies in atomic and molecular multiphoton and very high-order nonlinear optical processes, like high harmonic generation (HHG) [87, 88].

The most relevant theoretical question related to this topic is which kind of effective treatment we can find for the time-dependent Schrödinger equation (TDSE). Floquet theory [65] (reviewed in Chap. 3) is related to the class of periodic linear differential equations. Various generalized versions of the Floquet formalism are used in several different disciplines of physics, e.g.: multiphoton excitation (MPE) of two-level, multi-level atomic and molecular systems or multiple quantum (MQ) NMR transitions in spin-systems. Floquet's theory was proven to provide a robust mathematical background for the investigation of time-dependent transport in various materials [89, 90]. We will use the conventional Floquet theorem and discuss the general properties of Floquet quasi-energy states.

6.1 Model of loop geometries

The spintronic properties of various loop geometries and various polygon structures have already been investigated both experimentally and theoretically [91, 92]. Koga *et al.* have fabricated a square loop geometry which is made of InAlAs/InAlAs/InAlAs quantum wells. They have carried out spin interferometry experiments using the nanodevice in the ballistic transport regime [93]. A model for regular-polygon conductors which are connected by single-channel ballistic quantum wires with Rashba SOI, have been consid-

ered in Ref. [94].

In Ref. [95] and the current study as well, we consider a simple narrow quantum wire and a triangle-shaped nanostructure (see Fig. 6.1). Let us note that the role of the upper "dead-end" arms is to eliminate the sharp curvature of structure as well as the effect of spin rotation.

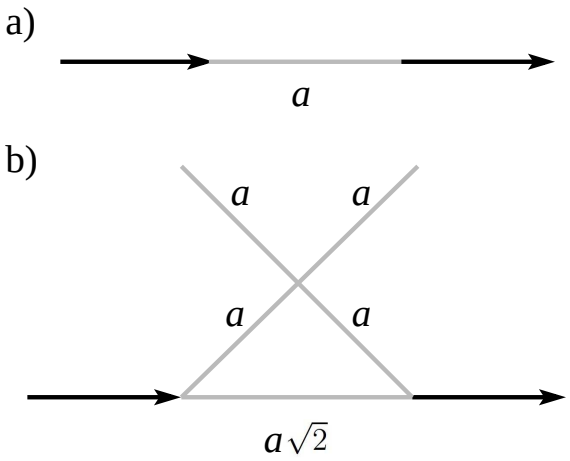

Figure 6.1: The geometry of the devices we investigated. The wires in which oscillating SOI is present are indicated by gray lines. We assume no spin-orbit interaction in the input/output leads that are represented by the black arrows [95].

6.2 Oscillating spin-orbit interaction and Floquet quasi-energies

The nanoscale devices we investigate are shown in Fig. 6.1. Their elementary building blocks – similarly to the case of the superlattices we discussed in Part II – are straight, narrow quantum wires. The relevant time-dependent Hamiltonian can be written [96] as

$$\tilde{H}(t) = \hbar\Omega \left[\left(-i\frac{\partial}{\partial s} + \frac{\omega(t)}{2\Omega}\mathbf{n}(\sigma \times \mathbf{e}_z) \right)^2 - \frac{\omega(t)^2}{4\Omega^2} \right], \tag{6.1}$$

where the unit vector $\mathbf{n}$ points to the chosen positive direction along the wire, and the characteristic kinetic energy can be found as $\hbar\Omega = \hbar^2/2m^*a^2$ (with a being the relevant length scale, see Fig. 6.1). The length variable (in units of a) along the wire is denoted by s. This term of $\tilde{H}$ which contains the time-dependent strength of the SOI is $\omega(t) = \alpha(t)/a$, where it is the Rashba parameter α that can be tuned by an external gate voltage [69, 60]. According to our assumption, the function $\omega(t)$ can be given by

$$\omega(t) = \omega_0 + \omega_1 \cos(\tilde{\nu}t). \tag{6.2}$$

Note that $\tilde{H}$ is linear in $\omega(t)$ [the compact form given by Eq. (6.1) does not show it explicitly, but the quadratic terms cancel each other]. The time-dependent Schrödinger equation governing the time evolution reads:

$$i\frac{\partial}{\partial\tau}|\psi\rangle(\tau) = H(\tau)|\psi\rangle(\tau), \tag{6.3}$$

where $\tau = \Omega t$ and $H(\tau) = \tilde{H}/\hbar\Omega$. The time-dependent part of the SOI can be written as $\omega_1 \cos(\nu\tau)$, where $\nu = \tilde{\nu}/\Omega$.

Note that for $a = 100$ nm, $m^* = 0.067m_e$ (GaAs), $\omega_0/\Omega \approx 5$ is in an experimentally achievable range, and Ω is of the order of 10^{11} Hz. For larger samples – according to the scaling discussed above – the characteristic frequencies are lower, and therefore the experimentally achievable maximal SOI strength corresponds to lower values of ω_0/Ω.

Since the Hamiltonian appearing in equation (6.3) is periodic in time, $H(\tau) = H(\tau + T)$ with $T = 2\pi/\nu$, Floquet theory [65] can be applied. Using a plane wave basis, the spinors

$$|\gamma^{\pm}\rangle(s) = \frac{e^{iks}}{\sqrt{2}} \begin{pmatrix} 1 \\ \pm ie^{i\gamma} \end{pmatrix}, \tag{6.4}$$

satisfy

$$H(\tau)|\gamma^{\pm}\rangle(s) = \left[k^2 \pm k\frac{\omega(\tau)}{\Omega} \right] |\gamma^{\pm}\rangle(s). \tag{6.5}$$

In this section, we shall focus on our time-periodic and dimensionless Hamiltonian ($H(\tau)$) and the corresponding dimensionless time evolution operator $U(\tau)$. Note that in our case

$$[H(\tau'), H(\tau'')] = 0. \tag{6.6}$$

As a consequence, the time evolution operator can be given by the following expression

$$U(\tau) = \exp\left[-i\int_0^\tau H(\tilde{\tau})\mathrm{d}\tilde{\tau}\right]. \tag{6.7}$$

We have already calculated the matrix elements of $H(\tau)$ in a convenient basis (4.7) and have found

$$H(\tau) = k^2 I + k\frac{\omega(\tau)}{\Omega}\sigma_\gamma = k^2 I + k\frac{\omega_0}{\Omega}\sigma_\gamma + k\frac{\omega_1}{\Omega}\cos(\nu\tau)\sigma_\gamma, \tag{6.8}$$

where I is the 2×2 unit matrix. According to Eq. (6.7) the operator $U(\tau)$ can be written as

$$U(\tau) = \exp\left[-ik^2\tau I\right]\cdot\exp\left[-ik\left(\frac{\omega_0}{\Omega}\tau\sigma_\gamma + \frac{\omega_1}{\nu\Omega}\sin(\nu\tau)\sigma_\gamma\right)\right]. \tag{6.9}$$

In order to obtain a simple form for this operator, we should use the fact that even powers of σ_γ equal to I and obviously the odd ones give σ_γ again. Consequently, the matrix of $U(\tau)$ reads

$$U(\tau) = e^{-ik^2\tau}\begin{pmatrix} \cos\left[k\frac{\omega_0}{\Omega}\tau + k\frac{\omega_1}{\nu\Omega}\sin(\nu\tau)\right] & -e^{-i\gamma}\sin\left[k\frac{\omega_0}{\Omega}\tau + k\frac{\omega_1}{\nu\Omega}\sin(\nu\tau)\right] \\ e^{i\gamma}\sin\left[k\frac{\omega_0}{\Omega}\tau + k\frac{\omega_1}{\nu\Omega}\sin(\nu\tau)\right] & \cos\left[k\frac{\omega_0}{\Omega}\tau + k\frac{\omega_1}{\nu\Omega}\sin(\nu\tau)\right] \end{pmatrix}. \tag{6.10}$$

The time-dependent eigenvalues of the dimensionless evolution operator are

$$\begin{aligned} u_+(\tau) &= \exp\left[-i\left(k^2 + k\tfrac{\omega_0}{\Omega}\right)\tau - ik\tfrac{\omega_1}{\nu\Omega}\sin(\nu\tau)\right] \\ u_-(\tau) &= \exp\left[-i\left(k^2 - k\tfrac{\omega_0}{\Omega}\right)\tau + ik\tfrac{\omega_1}{\nu\Omega}\sin(\nu\tau)\right], \end{aligned} \tag{6.11}$$

and eigenstates are given by

$$U(\tau)|\gamma^\pm\rangle = u_\pm(\tau)|\gamma^\pm\rangle. \tag{6.12}$$

Using the explicit form of the oscillating SOI, and performing the integral in the exponent (Eq. (6.7)), we obtain that the two nonequivalent Floquet quasi-energies for a fixed wavenumber k are given by

$$\varepsilon^\pm(k) = k^2 \pm k\frac{\omega_0}{\Omega}. \tag{6.13}$$

With these energies, the time-dependent eigenvalues $u_{\pm}(\tau)$ can be written as

$$u_{\pm}(\tau) = \exp\left[-i\varepsilon^{\pm}(k)\tau \mp ik\frac{\omega_1}{\nu\Omega}\sin(\nu\tau)\right], \tag{6.14}$$

and the 'time-dependent basis spinors' read

$$|\varphi^{\pm}\rangle(s,\tau) = u_{\pm}(\tau)|\gamma^{\pm}\rangle(s). \tag{6.15}$$

6.3 Generation of high harmonics

The frequencies (dimensionless energies) that appear in the exponent for a given k can be seen most directly by applying an appropriate Jacobi-Anger identity [46], leading to

$$|\varphi^{\pm}\rangle(s,\tau) = e^{-i\varepsilon^{\pm}(k)\tau}\sum_{n=-\infty}^{+\infty} J_n\left(\frac{k\omega_1}{\Omega\nu}\right)e^{\mp in\nu\tau}|\varphi^{\pm}\rangle(s), \tag{6.16}$$

where Bessel functions of the first kind [46] appear in the expansion.

In the followings the global solution of the transport problem is introduced. We assume no SOI in the leads (that are denoted by the horizontal (x direction) black arrows in figure 6.1), and consider a monoenergetic input

$$|\Psi\rangle_{in} = e^{i(k_0 x - k_0^2\tau)}|u\rangle, \tag{6.17}$$

where $|u\rangle$ can be an arbitrary spinor. In order to obtain a time-dependent solution in the whole domain, the spinor valued wavefunctions have to be joined at the junctions. We require the spinor components to be continuous. Additional boundary conditions can be obtained by using the relevant continuity equation (see the beginning of the previous chapter)

$$\frac{\partial}{\partial\tau}\rho(s,\tau) + \frac{\partial}{\partial s}J(s,\tau) = 0, \tag{6.18}$$

where the (unnormalized) electron density can be written as

$$\rho = \langle\Psi|\Psi\rangle(s,\tau), \tag{6.19}$$

while the corresponding current density [96] reads

$$J(s,\tau) = 2\mathrm{Re}\left\langle -i\frac{\partial}{\partial s} + \frac{\omega(\tau)}{2\Omega}\sigma_{\varphi}\right\rangle_{|\Psi\rangle(s,\tau)}. \tag{6.20}$$

$|\Psi\rangle(s,\tau)$ above denotes a solution to the time-dependent Schrödinger equation (6.3) and the inner product and the expectation value appearing in equations (6.19) and (6.20) are understood in the spinor sense, that is, no spatial integration is involved. As usual, the

physical meaning of the continuity equation (6.18) is seen most directly by integrating it over a finite spatial domain. The (unnormalized) probability of finding an electron inside the domain changes as a consequence of the currents flowing in/out at the boundaries. Focusing on a certain junction, we obtain that the current that enters the junction should also leave it – always, i.e. at any time instants. As we shall see, the boundary conditions [80] described above can be handled conveniently in frequency domain.

Let $\varepsilon_0 = k_0^2$ denote the (dimensionless) frequency of the input. A spinor valued wave function with this frequency partially enters the domain of oscillating SOI (and partially gets reflected). According to the previous subsection, whenever a frequency component ε_0 appears in the solution of the time-dependent Schrödinger equation (6.3), an infinite number of additional 'Floquet channels' [22] corresponding to frequencies

$$\varepsilon_n = \varepsilon_0 + n\nu \tag{6.21}$$

open for transmission (with n being an integer). Therefore the frequency components given by equation (6.21) should be taken into account. However, these frequencies are also sufficient for the complete description of the problem. Since the frequency resolved fitting equations are linear and generally non-degenerate, they provide a nonzero result only for nonzero input, i.e., for the set of frequencies given by equation (6.21).

According to equation (6.16), inside a domain with oscillating SOI, the relevant frequencies are members of the set (6.21), if one of the Floquet quasi-energies (6.13) is equal to ε_n, with an arbitrary integer n. The solutions of the equations $\varepsilon^{\pm}(k) = \varepsilon_n$ are

$$k^+_{1,2}(\varepsilon_n) = -\frac{\omega_0}{2\Omega} \pm \sqrt{\frac{\omega_0^2}{4\Omega^2} + \varepsilon_n} \tag{6.22}$$

and

$$k^-_{1,2}(\varepsilon_n) = \frac{\omega_0}{2\Omega} \pm \sqrt{\frac{\omega_0^2}{4\Omega^2} + \varepsilon_n}, \tag{6.23}$$

where the subscripts correspond to the $\pm$ signs in the equations. Using these wavenumbers, a general solution that contains all the frequencies relevant for the description of the problem with the monoenergetic input (6.17) can be written as

$$|\Psi\rangle_{osc} = \sum_{n=-\infty}^{+\infty} \sum_{m=1,2} (a^+_{n,m}|\varphi^+\rangle_{n,m} + a^-_{n,m}|\varphi^-\rangle_{n,m}), \tag{6.24}$$

where $a^+_{n,m}$ are unknown coefficients, the space and time dependence of the spinors have been omitted, and $|\varphi^{\pm}\rangle_{n,m}$ denote $|\varphi^{\pm}\rangle(s,\tau)$ evaluated at $\varepsilon^{\pm}(k) = \varepsilon_n$ and $k = k^{\pm}_m(\varepsilon_n)$. That is,

$$|\varphi^{\pm}\rangle_{n,m}(s,\tau) = e^{-i\varepsilon_n\tau} \sum_{\ell=-\infty}^{+\infty} J_\ell\left(\frac{k^{\pm}_m(\varepsilon_n)\omega_1}{\Omega\nu}\right) e^{\mp i\ell\nu\tau}|\varphi^{\pm}\rangle(s). \tag{6.25}$$

The relevant spinor valued wavefunction in the input lead is the sum of $|\Psi\rangle_{in}$ and the reflected part,

$$|\Psi\rangle_{ref}(s,\tau) = \sum_n e^{-i(k'_n s+\varepsilon_n \tau)}(r_n^{\uparrow}|\uparrow\rangle + r_n^{\downarrow}|\downarrow\rangle), \tag{6.26}$$

where

$$k'_n = \sqrt{\varepsilon_n}, \tag{6.27}$$

while $|\uparrow\rangle$ and $|\downarrow\rangle$ can be arbitrary, provided they are orthogonal in the spinor sense. Note that for negative ε_n, k'_n becomes imaginary; by choosing $k'_n = i\sqrt{-\varepsilon_n}$, we can ensure that the corresponding waves decay exponentially towards $x = -\infty$. These 'evanescent' solutions can play an important role in our description based on Floquet states. (The wavenumbers $k_i^{\pm}(\varepsilon_n)$ given by equations (6.22) and (6.23) can also be purely imaginary, but in such cases both signs of the square root are allowed, since they contribute to the wavefunction in a finite domain.)

The transmitted solution in the output lead is analogous to $|\Psi\rangle_{ref}$, only the signs of the wavenumbers are opposite due to the different propagation directions,

$$|\Psi\rangle_{trans}(x,\tau) = \sum_n e^{i(k'_n x-\varepsilon_n \tau)}(t_n^{\uparrow}|\uparrow\rangle + t_n^{\downarrow}|\downarrow\rangle). \tag{6.28}$$

Equations (6.24), (6.26) and (6.28) describe the spinor valued solutions of the time-dependent Schrödinger equation in all spatial domains. In order to take boundary conditions into account, first one has to evaluate these solutions and their spatial derivatives at the junctions (including the internal ones that are not connected to the input/output leads). As one can see easily, Griffith's boundary conditions [80] mean a system of linear equations for the coefficients appearing in equations (6.24), (6.26) and (6.28). Although in principle we have an infinite number of equations, since the Bessel functions J_n for a given argument decrease as a function of their index, correct numerical solutions can be obtained by limiting ourselves to a finite number of frequencies. The convergence of the Jacobi-Anger expansion, as well as the obtained wave functions, was carefully checked when calculating the results to be presented in the following.

6.4 Oscillation of the spin direction

The simple straight geometry shown by figure 6.1 (a) already shows important consequences of the oscillating SOI. Additionally, it can be used to determine the parameter ranges to focus on. Although the term 'traverse time' is difficult to interpret when the input is an infinite wave, the ratio of the lengths a and $c = E(k)/\hbar k$ with a characteristic

wave vector k can tell us which SOI oscillation frequency domain is quasistatic. Accordingly, when $\nu \ll k$ (in dimensionless units), SOI oscillation related effects are expected to be weak. Furthermore, by inspecting equations (6.22)-(6.24), one can see that the oscillating part of the SOI alone does not induce spin precession. However, when $\omega_0 \neq 0$, the wavenumbers that belong to different eigenspinor directions are not the same, thus the spin directions related to superpositions have a nontrivial spatial dependence.

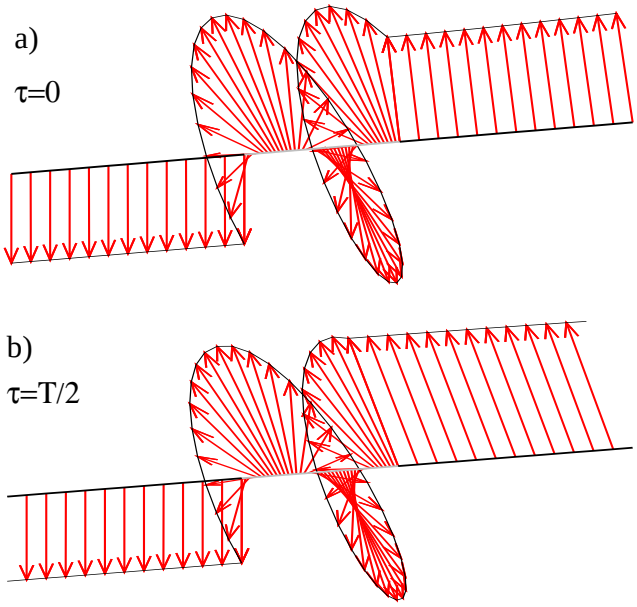

Figure 6.2: Snapshots of the spin direction along a quantum wire. Oscillating SOI is present in the central region (where the color of the wire is gray.) The parameters are $\omega_0/\Omega = \omega_1/\Omega = 9$, $\nu = 1$ and $k_0 a = 1.5$. The top panel corresponds to $\tau = 0$, while $\tau = T/2$ for panel b). The thin black line that connects the arrowheads is plotted in order to guide the eyes [95].

Figure 6.2 demonstrates this effect. In order to focus on the spin direction alone, the solution $|\Psi\rangle(s,\tau)$ (that stands for $|\Psi\rangle_{ref}(s,\tau) + |\Psi\rangle_{in}(s,\tau)$, $|\Psi\rangle_{osc}(s,\tau)$ or $|\Psi\rangle_{trans}(s,\tau)$, depending on the position) has been divided by the space- and time-dependent electron density given by equation (12) (which happens to be nonzero in this case.) The change of the spin direction along the wire is represented by plotting

$$\mathbf{S}(s,\tau) = \frac{\mathbf{P}(s,\tau)}{\rho(s,\tau)} = \frac{1}{\rho(s,\tau)} \begin{pmatrix} \langle\sigma_x\rangle_\Psi \\ \langle\sigma_y\rangle_\Psi \\ \langle\sigma_z\rangle_\Psi \end{pmatrix} (s,\tau), \tag{6.29}$$

where the usual Pauli matrices σ_i appear. More precisely, the arrows shown in figure 6.2 points from $(x,0,0)$ to $(x+S_x, S_y, S_z)$, i.e. they visualize the spin direction in a local

coordinate system. The input spinor valued wavefunction is polarized in the positive z direction in figure 6.2. Note that considering any of the eigenspinors (6.4) as input, the spin direction does not change.

Since any difference of the relevant frequencies (6.21) is an integer multiple of ν, the time evolution is periodic ($T = 2\pi/\nu$). Figure 6.2 corresponds to two different time instants, $\tau = 0$ (panel (a)) and $\tau = T/2$ (panel (b)). As we can see, the spin direction has a strong spatial dependence in the region where SOI is present, and when ω_0 is relatively large, there is also a visible time dependence (see around the output lead).

6.5 Generation of propagating density and spin polarization waves

Although it is difficult to observe in figure 6.2, the oscillating SOI can generate waves that propagate away from the source even in the case of a simple straight wire. The physical reason for the existence of these propagating waves is that SOI oscillations pump energy in the system and populate Floquet states with various frequencies and wavenumbers. Boundary conditions 'transfer' these populations to regions without SOI, and the interference of these states appears as wave propagation.

Figure 6.3 shows snapshots of the time evolution of the electron density given by equation (6.19). The quantum wire is also shown in this figure, and for each point $(x, y, 0)$ of the wire (located in the $z = 0$ plane) ρ is plotted as $(x, y, \rho(x, y))$; see the solid red and blue lines. As we can see, density waves arise and propagate even for moderate SOI strengths.

The figure shows the time evolution of $\rho(s, \tau)$ for both eigenspinors given by equation (6.4). Let us recall that the spin direction is conserved for these input spinors, i.e., in contrast to the case shown in figure (6.2), there are no time-dependent spin rotations. On the other hand, however, the space and time dependence of the probability density is different for the two eigenspinor directions. Let us emphasize that this effect is absent for static SOI, when the (time independent) transmission probability is the same for any input spin direction for a two-terminal device. This remarkable difference—on the level of the equations—can be understood by observing that the wavenumbers (6.22) and (6.23) that correspond to the two input spin directions are different when neither the oscillating nor the static part of the SOI is zero. Consequently, the spatial interference of superpositions of plane waves with these wavenumbers produces different patterns for different input eigenspinors. Note that (as we shall see in the following subsection) this fact can lead to

temporal spin-polarization– which is completely absent for the case of static SOI. The related 'no-go theorem' [97] for the equilibrium spin currents is based on symmetry based considerations, such as the unitarity of the scattering matrix that ensures that the sum of the transmission and reflection probabilities is unity. However, the probability density inside a region with oscillating SOI is generally not constant, thus, due to the continuity equation (6.18), the magnitude of the current that flows out of the domain does not need to be equal to the current that flows in–at least not at any time instants. This is the symmetry related, physical reason for the qualitative difference between the transmission properties of two-terminal devices with static and oscillating SOI.

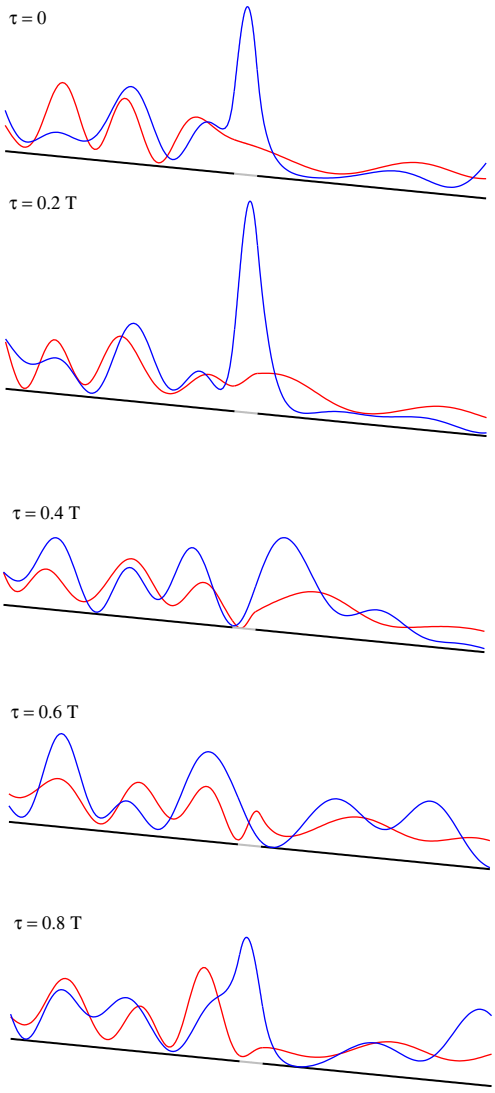

Figure 6.3: Generation of density waves by oscillating SOI in a quantum wire. The solid red and blue lines show electron density $\rho(s,\tau)$ given by equation 6.19 for the $|\gamma^+\rangle(s)$ and $|\gamma^-\rangle(s)$ eigenstate inputs (equation (6.4)), respectively. The parameters are $\omega_0/\Omega = 2.5$, $\omega_1/\Omega = 2.0$, $\nu = 1.0$ and $k_0 a = 1.0$. Time instants when the snapshots were taken are denoted in units of $T = 2\pi/\nu$ [95].

As a final comment on this point, let us add that although the sum of the reflected and transmitted currents does not always need to be equal to the input current, the periodicity of the problem ensures that the average of these quantities over an oscillation period T satisfies the relation

$$\int_0^T J_{trans}\mathrm{d}\tau + \int_0^T J_{ref}\mathrm{d}\tau = \int_0^T J_{in}\mathrm{d}\tau \tag{6.30}$$

The reflected and transmitted current densities appearing in the integrands are to be calculated using equation (6.20) with $|\Psi\rangle = |\Psi\rangle_{ref}$ or $|\Psi\rangle = |\Psi\rangle_{trans}$ (see equations (6.26), (6.28)) evaluated at the input and output junctions, respectively. In practice, we can use these average quantities to check the accuracy of our numerical method: whenever the requirement above is not satisfied within the required numerical precision, more frequency components (6.21) have to be taken into account.

In figure 6.4 we can see the spin direction in the output lead of the geometry shown in figure 6.1(b) for several time instants. The input spin is polarized in the positive z direction (not shown), and the spin direction along the lead is visualized in the same way as in figure 6.1. We can clearly identify propagating patterns in this figure.

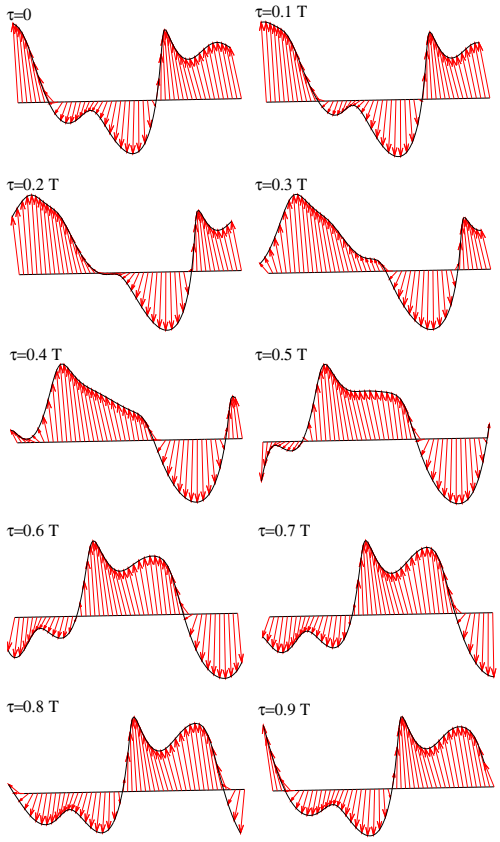

Figure 6.4: Wave-like propagation of the spin direction in the output lead of the loop shown in figure 6.1(b). The parameters are $\omega_0/\Omega = 3.0$, $\omega_1/\Omega = 1.0$, $\nu = 1.0$ and $k_0 a = 1.5$. Time instants when the snapshots were taken are indicated in units of $T = 2\pi/\nu$ [95].

6.6 Time-dependent spin-polarization

In Ref. [95], we considered the realistic situation of totally unpolarized or random incoming electrons. Therefore their spin state can be described by a density operator

$$\varrho_{in} = \frac{1}{2}\left[|\uparrow\rangle\langle\uparrow| + |\downarrow\rangle\langle\downarrow|\right], \tag{6.31}$$

where the spinors $|\uparrow\rangle$ and $|\downarrow\rangle$ correspond to spin-up and spin-down states, respectively. Let us note that ϱ_{in} is constant for a single plane. However, inside the nanostructure, it will be a function of space (s) and time (τ):

$$\varrho(s,\tau) = \frac{1}{2}\left[|\Psi_\uparrow\rangle\langle\Psi_\uparrow|(s,\tau) + |\Psi_\downarrow\rangle\langle\Psi_\downarrow|(s,\tau)\right]. \tag{6.32}$$

Using $\varrho(s,\tau)$, the time-dependent electron density (6.19) can be written as $\rho(s,\tau) = Tr[\varrho(s,\tau)]$, where the difference between ρ and ϱ should be emphasized.

The most interesting result related to $\varrho(s,\tau)$ is that completely polarized states can be realized at the output wire. As we have already pointed out, this phenomenon is in strong contrast with the case of stationary SOI, when a loop rotates the input spin direction - always in the same way, whatever that direction was [98, 97]. The physical reason for temporal spin polarization seen in figure (6.5) becomes most transparent by recalling figure (6.3), where the probability densities had different space- and time-dependent interference patterns for two eigenspinor inputs. In other words, there are space-time points where the interference is completely destructive for one of the eigenspinor directions, but not for the other one. This results in a completely polarized spinor. (This is formally analogous to the case published in [71] for a ring with constant SOI and two output terminals.) The results to be presented in this subsection hold for both geometries shown in figure 6.1, but–due to the increased number of paths that can interfere–the effects are stronger for the triangle loop (figure 6.1(b)). However, let us emphasize that the appearance of the temporal spin-polarization as a physical effect has a weak dependence on the device geometry, e.g., we expect it to be present also for quantum rings (where the technique introduced in the previous section has to be modified) as well as for various polygon geometries [99, 92].

In order to quantify the polarization effects, panel (b) of figure 6.5 shows

$$p(x,\tau) = \frac{Tr[\varrho^2(x,\tau)]}{Tr[\varrho(x,\tau)]^2} \tag{6.33}$$

as a function of time and the x coordinate in the output lead. Note that the division by the square of the electron density is just for normalization. This function measures the

'purity' of the spin state: its range is $\left[\frac{1}{2}, 1\right]$, where the minimum and maximum correspond to completely unpolarized and 100% polarized (i.e. pure) states, respectively. According to figure 6.5, almost perfect polarization can occur in the output lead for moderate SOI strengths. Additionally, taking a look at panel (a) of figure 6.5, we can also see that ρ is not zero when the spin is polarized, i.e. there is a finite probability of finding the spin-polarized electron at that point.

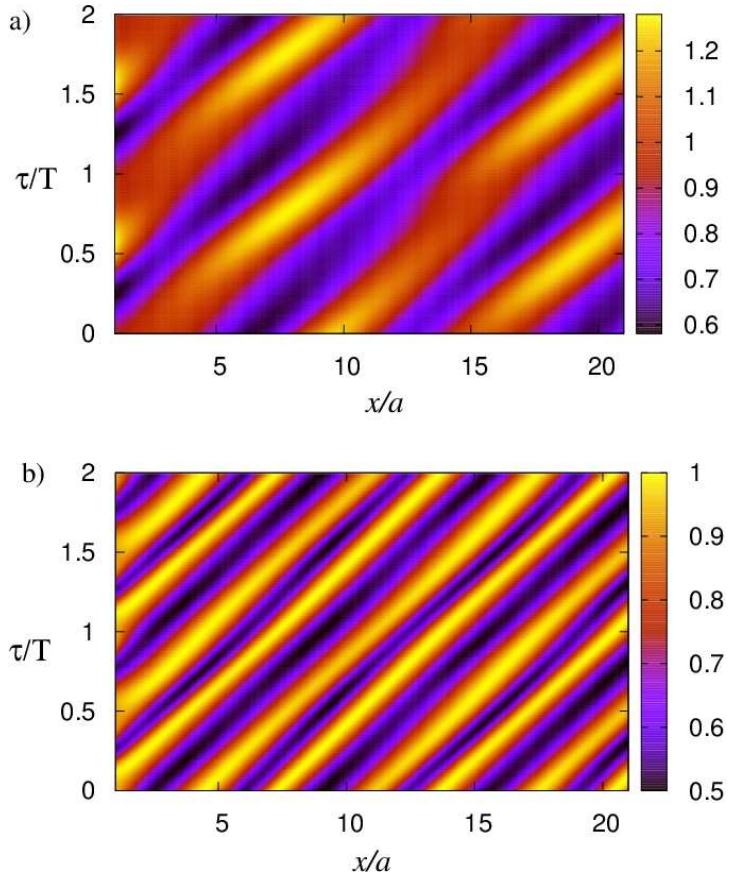

Figure 6.5: The output corresponding to an input whose polarization is random for the triangle loop shown in figure 6.1(b). Panel $a)$ shows the electron density $\rho(x, \tau)$, while the quantity $p(x, \tau)$ (6.33) is shown in panel $b)$. The chosen parameters are $\omega_0/\Omega = 3.0$, $\omega_1/\Omega = 0.3$, $\nu = 1.0$ and $k_0 a = 1.0$. Recall that $\rho(x, \tau)$ is not normalized [95].

6.7 Scatterers in loop geometries

Finally we investigate the question to what extent our findings are modified by the decrease of the mean free path as a consequence of scattering processes. To this end, we

introduce a random potential

$$U_{scatt}(x) = \sum_n U_n(D)\delta(x - x_n), \tag{6.34}$$

where x_n denote uniformly distributed random positions and $U_n(D)$ represents a 2×2 diagonal matrix, with independent random diagonal elements $U_{n1}(D)$ and $U_{n2}(D)$. The argument D is the root-mean-square deviation of the corresponding normal distribution, the mean of which is zero. These Dirac delta peaks represent spin-dependent random scatterers and provide an effective model for magnetic impurities of various concentrations: $D = 0$ corresponds to the ballistic case, while increasing values mean shorter mean free paths.

In order to see the physical consequences of the scattering processes, we perform a sufficiently large number of computational runs with different realizations of the random potentials (6.34) and appropriately average the result (see [85] for more details). The polarization effect predicted by our model can be destroyed by scattering induced decoherence in two ways, depending on the position of the scatterers: in the region with oscillating SOI, the generation of the spin-polarized waves can be hindered, and/or the amplitude of these waves can be decreased by scatterers in the region where they propagate (i.e. where there is no SOI). Note that the input spin state is already completely unpolarized, thus there is no need to consider scatterers in the input lead.

As it is shown by figure 6.6 – according to expectations – the polarization effect gets definitely weaker when we introduce scatterers. Note that $D = 0.6\hbar\Omega$ that corresponds to this figure means a relatively strong influence on the transport properties: it increases the reflection probability by roughly a factor of two. Moreover, figure 6.6 visualizes the 'worst case', since nonmagnetic scatterers (where U is diagonal (this case is not shown in the figure)) decrease the conductance by a similar amount, but their influence on spin polarization is considerably weaker. This fact emphasizes the importance of spin coherence length in our findings.

The most interesting fact we can see in figure 6.6 is that the generation of spin-polarized waves is less sensitive to scattering processes than the propagation of these waves: the same number of scatterers with the same value of D have a weaker effect when they are placed in the region where the SOI oscillates. That is, although spin-dependent random scattering decreases the degree of polarization independently of the position of the scatterers, when this process takes place inside the region with oscillating SOI, spin polarization can still build up, at least partially. This effect can be understood qualitatively: the spin polarization at the output is stronger when the 'interaction region' (where the SOI oscillates and polarization is generated) is longer (with all other parameters being

the same). When the spin coherence length decreases below the extension of this region, it defines a new effective length along which polarization is generated. Thus, realistically, in a sample with long interaction region and disorder, it is the spin coherence length that determines the degree of polarization right at the output, and this is also the length scale that tells us the distance below which the spin-polarized electron waves can be detected in the output lead.

The results of this subsection show that the polarization effect we described earlier in this chapter is not highly sensitive to scattering induced decoherence, thus its experimental observation is possible.

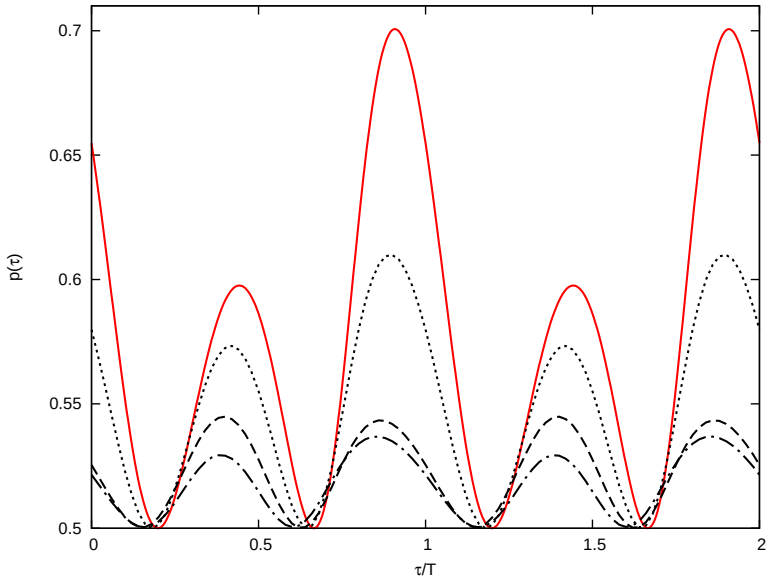

Figure 6.6: The role of spin-dependent scattering mechanisms in the production of spin-polarized currents. $p(\tau)$ (given by equation (6.33)) is shown at $x = 3a$ for the linear geometry shown in figure 6.1(a). The parameters are $\omega_0/\Omega = 5.0$, $\omega_1/\Omega = 0.3$, $\nu = 1.0$ and $k_0 a = 1.0$. The red curve corresponds to the case without scatterers ($D = 0$ in equation (6.34)), while $D = 0.6\hbar\Omega$ for the black curves. This relatively strong scattering is present only in the region with oscillating SOI for the dotted curve, and only in the output lead for the dashed curve, while the dashed-dotted line corresponds to the case when there are scatterers in both spatial domains. Technically, we considered three independent, randomly located scattering centers in both regions [95].

6.8 Conclusions

In this chapter we investigated spin dependent quantum transport through devices in which the spin-orbit interaction (SOI) is time dependent, more precisely, it oscillates. By considering a monoenergetic input, we have shown the emergence of electron density and spin polarization waves propagating away from their source, i.e. the region with oscillating SOI. Additionally, it was demonstrated that simple geometries can produce spin-polarized wavepackets even for completely unpolarized input. According to our calculation, this dynamical spin polarization effect appears for realistic, experimentally achievable parameter ranges and remains observable when moderately intensive scattering processes are also taken into account. In other words, our model suggests a novel source of spin-polarized electrons that can be realized with pure semiconducting materials without the use of external magnetic fields.

Summary

This Ph.D. thesis is devoted to the investigation of certain mesoscopic systems. These objects are material systems having dimensions between the size of atoms, molecules and that of macroscopic structures. Nowadays, the term nanostructure is often used as synonym of a mesoscopic system. The lower limit of the mesoscopic scale can be as low as the size of a small cluster containing only few atoms, but there is no strict definition for mesoscopic physics. As a guideline, we may say typical systems that are studied in this field are in the range between the size of a small virus and the size of a typical bacterium.

Both experimental results and theoretical models have shown that although a mesoscopic sample can contain a large number of atoms, its electronic and magnetic properties can be determined by quantum interference effects. In the case of an ohmic conductor which has macroscopic dimensions, the conductance increases continuously with its width. However, the conductance of a nanowire is quantized, that is, discrete steps appear in the conductance as a function of the gate voltage [30, 31]. This fundamental discovery offers practical opportunities as well, especially when a macroscopic electronic device is miniaturized, which is the general direction of the development in semiconductor electronics.

The current work is strongly related to quantum theory of spin systems. Spintronics (or spin electronics) is a promising field that has a kind of multidisciplinary nature in solid state physics. The aim of the research in this rapidly developing field is the control and manipulation of spin degrees of freedom in various material samples. Spintronics concentrates on the basic physical principles underlying the generation of carrier spin polarization, spin dynamics, and spin-polarized transport in semiconductors and metals. Spin transport differs from charge transport in that spin is a not conserved quantity in solids owing to spin-orbit and hyperfine coupling [2, 100, 3].

The topic of the current dissertation is electron transport in two-dimensional nanostructures in the presence of Rashba-type spin-orbit field.

Stationary SOI controlled properties of 2D superlattices

We have investigated artificial crystal-like (quasi)periodic structures which can modulate the electron current due to the Rashba-type spin-orbit interaction. This model of lateral superlattices, in other words, describes a spintronic crystal. As we have shown, both the energy and spin of the electrons propagating through such a (quasi)periodic structure can be controlled by the properties of the spintronic crystal. The behavior of the electrons in narrow quantum wires (that are building blocks of the superlattices) is determined by an appropriate spin-dependent Hamilton operator. In our case, the Rashba-type spin-orbit interaction term appears as an effective potential in the Hamiltonian, modifying the eigenenergies and eigenstates of the system. The spinor valued wavefunction is created as a linear combination of eigenstates with the appropriate wavenumbers. We provide the correct form of the probability current density which is equal to the expectation value of operator j_γ. It can describe the net spin current in the presence of SOI.

Quantum wire segments are joined together at junctions, that is, the electrons are scattered by the geometry of the nanoscale system. Practically, this means that the wavefunctions have to fulfil appropriate boundary conditions at each junction. In the case of an infinite periodic structure, we look for special waves with their lattice-periodic part being factorized – in accordance with Bloch's theorem. The band structure of an infinite lattice is determined in this way. We have also shown how the band scheme depends on the geometrical parameters of the lattice and the strength of the SOI [III.].

Practically, the boundary conditions at the junctions mean a linear system of equations, the solution of which provides the components of the reflected and transmitted spinors for a given input. For finite networks, we use the Landauer-Büttiker formalism in order to calculate the conductance from the transmission coefficients. We have observed that the positions and widths of the non-conducting regions are sensitive to the strength of the spin-orbit coupling. Comparing the band structure with the conductance properties of finite systems, we found that already for relatively small arrays, forbidden bands are clearly seen in the conductance. We have also investigated various possible spintronic applications that are related to energy filtering and spin-polarization effects [III.].

Finite-temperature conductance of 2D superlattices

Nowadays, experimental technics allow the measurement of the electronic and magnetic properties of various real nano-objects which have been fabricated from, e.g. semiconductor heterostructures [101]. At the same time, the temperature of the sample and its environment is not a negligible factor if we want to study quantum mechanical phenomena. In general, thermal fluctuations as well as any additional dephasing mechanisms eliminate the effects induced by quantum interference.

At finite temperatures electron transport cannot be modelled by assuming monoenergetic electrons. In this case, the incoming and outgoing spinor valued wavefunctions can be described by using density operators. It was demonstrated that the SOI can strongly modulate the finite temperature conductance, and this effect is still present at high temperatures. We investigated how dephasing effects modify this result, and found it to be valid even when conductance is strongly suppressed due to scattering events [II.].

Effects of oscillating SOI

The main goal was to reveal the basic features of quantum transport in the presence of time-dependent Rashba-type spin-orbit coupling. Note that the interaction of alternating external fields and a material system occurs in various fields of physics. Important examples are: high-order harmonic generation in laser-driven atomic and molecular systems and transport in solids manipulated by an external, time-dependent gate voltage. In our case, when a time-periodic Hamiltonian describes the quantum system, Floquet's theory provides solid mathematical background for our studies.

We assumed monoenergetic incoming electrons which can propagate in quantum wire segments of polygon geometries. Our model structures were a single moded straight nanowire and a triangle loop. The Hamiltonian have time-dependence via the SOI term. The approach of this work was to look for appropriate solutions to the time-dependent Schrödinger equation (TDSE). We determined the Floquet quasi-energies and the corresponding time-dependent basis spinors. Due to the generation of harmonics, the reflected and transmitted wavefunctions include integer multiples of the frequency of the oscillating SOI. We mainly focused on spin-dependent currents and time averaged transport properties. The spin direction and electron density show wavelike propagation away the region where SOI is present.

Our main result shows that simple geometries can produce spin-polarized wavepackets even for completely unpolarized input. The polarization effect is not extremely sensitive to scattering induced decoherence, thus its experimental observation may be possible [I.].

Samenvatting

Deze doctoraatsthesis is gewijd aan het onderzoek van bepaalde mesoscopische systemen. Deze objecten zijn materiële systemen met afmetingen tussen die van atomen en moleculen en die van macroscopische systemen. Tegenwoordig wordt de term nanostructuur dikwijls gebruikt als synoniem voor een mesoscopisch systeem. De benedenlimiet van de mesoscopische schaal kan zo laag zijn als de grootte van een kleine cluster die slechts enkele atomen bevat, maar er is geen strikte definitie voor mesoscopische fysica. Als richtlijn kunnen we zeggen dat typische systemen die bestudeerd worden in dit onderzoeksgebied een grootte hebben tussen kleine virussen en typische bacteriën.

Hoewel mesoscopische samples een groot aantal atomen kunnen bevatten hebben zowel experimentele resultaten als theoretische modellen aangetoond dat hun elektronische en magnetische eigenschappen bepaald worden door kwantuminterferentie-effecten. In het geval van een Ohmse geleider die macroscopische afmetingen heeft neemt de geleiding continu toe met de breedte. De geleiding van een nanodraad is daarentegen gekwantiseerd wat willen zeggen dat de geleiding met discrete stapjes verandert als functie van de spanning. Deze fundamentele ontdekking biedt ook praktische mogelijkheden, vooral wanneer een macroscopische elektronisch toestel geminiaturiseerd is, wat de algemene tendens in de ontwikkeling van halfgeleiderelektronica is.

Het huidige werk is sterk verbonden met de kwantumtheorie van spinsystemen. Spintronica (of spinelectronica) is een veelbelovend onderzoeksgebied met een multidisciplinair karakter binnen de vastestoffysica. Het doel van het onderzoek in dit snel evoluerende domein is de controle en manipulatie van de spinvrijheidsgraden in allerlei materialen. Spintronica concentreert zich op de basisprincipes die ten grondslag liggen aan het genereren van spinpolarisatie, spindynamica en spingepolariseerd transport in halfgeleiders en metalen. Spintransport verschilt van ladingstransport in zoverre dat het geen behouden grootheid is in vaste stoffen door de spin-baankoppeling en hyperfijne koppeling [2, 100, 3].

Het onderwerp van de huidige dissertatie is het elektrontransport in tweedimensionale nanostrucutren in de aanwezigheid van Rashba-achtige spin-baanvelden [9].

Stationaire SOI-gecontroleerde eigenschappen van 2D superroosters.

We hebben artificiële kristalachtige (quasi)periodische structuren onderzocht die de elektronenstroom kunnen beïnvloeden door spin-baankoppeling van het Rashba type. Dit model van laterale superroosters beschrijft met andere woorden een spintronisch kristal. Zoals we hebben aangetoond kunnen zowel de energie als de spin van elektronen in dergelijke (quasi)periodische structuren gecontroleerd worden door de eigenschappen van het spintronisch kristal. Het gedrag van de elektronen in dunne kwantumdraden (die de basiseenheden vormen van de supperroosters) wordt bepaald door een geschikte spinafhankelijke hamiltoniaan. In ons geval verschijnt de spin-baaninteractie van het Rashba type als een effectieve potentiaal in de hamiltoniaan die de eigenenergieën en de eigentoestanden van het systeem kan veranderen. De spinorgolffunctie wordt gevormd door een lineaire combinatie van eigentoestanden met geschikte golfgetallen. We leveren de juiste vorm van de waarschijnlijkheidsdichtheidsstroom die gelijk is aan de verwachtingswaarde van de operator j_γ. Deze kan de netto spinstroom beschrijven in de aanwezigheid van SOI.

Verschillende delen van de kwantumdraad zijn aan elkaar gehecht door juncties wat wil zeggen dat de elektronen verstrooid worden door de geometrie van het systeem. In de praktijk betekent dit dat de golffuncties aan geschikte randvoorwaarden moeten voldoen aan de juncties. In het geval van een zich oneindig herhalende structuur zoeken we naar speciale golven waarvan het periodisch-roostergedeelte gefactoriseerd is in overeenstemming met het Bloch-theorema. De bandenstructuur van een oneindig rooster wordt op deze manier bepaald. We hebben ook aangetoond hoe de banden afhangen van de geometrische parameters van het rooster en de sterkte van de SOI [III.].

In de praktijk leiden de randvoorwaarden aan de juncties tot een lineair systeem van vergelijkingen waarvan de oplossing de componenten levert van de teruggekaatste en doorgelaten spinors voor een bepaalde input. Voor eindige systemen gebruiken we het Landauer-Büttiker-formalisme om de geleiding te berekenen met behulp van de transmissiecoëfficiënten. We stelden vast dat de posities en breedtes van de niet-geleidende gebieden afhingen van de sterkte van de spin-baankoppeling. Wanneer we de bandenstructuur met de geleidingseigenschappen vergeleken van de eindige systemen konden we reeds bij relatief kleine rijen verboden banden waarnemen in de geleiding. We hebben ook allerlei mogelijke spintronicatoepassingen onderzocht die verband houden met energiefiltering en spinpolarisatie-effecten [III.].

Geleiding van 2D superroosters bij eindige temperatuur

Tegenwoordig laten experimentele technieken toe om de elektronische en magnetische eigenschappen te meten van verschillende echte nano-objecten die gemaakt worden van bvb. halfgeleider heterostructuren [101]. De temperatuur en de omgeving van het sample zijn ook geen verwaarloosbare factorer als we kwantummechanische fenomenen willen bestuderen. In het algemeen elimineren thermische fluctuaties en bijkomende ontfasingsmechanismen de effecten van kwantuminterferentie.

Bij eindige temperaturen kan het elektrontransport niet gemodelleerd worden in de veronderstelling dat de elektronen dezelfde energie hebben. In dit geval worden de inkomende en uitgaande spinorgolffuncties beschreven door dichtheidsoperatoren. Er werd aangetoond dat de SOI de geleiding bij eindige temperatuur sterk kan beïnvloeden en dat dit effect nog steeds aanwezig is bij hoge temperaturen. We hebben onderzocht hoe ontfasende effecten dit resultaat kunnen beïnvloeden en vonden dat het effect nog optreedt als de geleiding sterk onderdrukt wordt door verstrooiingseffecten [II.].

Effecten van schommelende SOI

Het hoofddoel was om de basiskenmerken van kwantumtransport te onthullen in de aanwezigheid van tijdsafhankelijke spin-baaninteractie van het Rashba type. Merk op dat de interactie van alternerende uitwendige velden met een materieel systeem in verschillende fysicadomeinen voorkomt. Belangrijke voorbeelden zijn: hoge-orde harmonische generatie in lasergedreven atomaire en moleculaire systemen en transport in vaste stoffen die gemanipuleerd worden door uitwendige tijdsafhankelijke spanningen. In ons geval, dus wanneer het systeem beschreven wordt door een tijdsperiodische hamiltoniaan, wordt een stevige wiskundige achtergrond geleverd door de theorie van Floquet.

We gingen ervan uit dat de inkomende elektronen gelijke energieën hadden en dat ze konden propageren in stukken kwantumdraad met de vorm van polygonen. Onze modelstructuren bestonden uit een rechte nanodraad en een driehoekige lus. De hamiltoniaan had een tijdsafhankelijkheid door de SOI-term. De aanpak van dit werk was te kijken naar geschikte oplossingen voor de tijdsafhankelijke Schrödingervergelijking (TDSE). We bepaalden de Floquet quasi-energieën en de overeenkomstige tijdsafhankelijke basisspinors. Door de vorming van harmonieken bevatten de gereflecteerde en doorgelaten golffuncties gehele aantallen van de frequentie van de oscillerende SOI. We hebben hoofdzakelijk gekeken naar spinstromen en tijdsgemiddelde transporteigenschappen. De richting van de spin en de elektronendichtheid toonden golfachtige voortplanting buiten het gebied waar de SOI aanwezig was.

Onze belangrijkste resultaten tonen dat eenvoudige geometrieën spingepolariseerde golfpakketten kunnen veroorzaken, zelfs voor niet-gepolariseerde inputs. Het polarisatie-effect is niet erg gevoelig voor verstrooiing door decoherentie, dus is haar experimentele waarneming misschien mogelijk [I.].

Összefoglalás

Jelen PhD értekezés témája bizonyos mezoszkopikus rendszerek vizsgálata. Ezek az objektumok olyan anyagi rendszerek, melyek nagyságukat tekintve az atomi méretek és a makroszkopikus struktúrák között helyezkednek el. Napjainkban a nanostruktúra kifejezést gyakran a mezoszkopikus rendszer szinonimájaként használjuk. A mezoszkopikus skála alsó határát általában egyetlen atom méretével ($0.1\,\mathrm{nm}$) azonosítjuk, de ez nem tekinthető szigorú értelemben vett definíciónak. A tanulmányozott rendszereinkről azonban összességében elmondható, hogy az $100\,\mathrm{nm}$ (egy vírus jellemző mérete)-$1000\,\mathrm{nm}$ (egy baktérium jellemző mérete) tartományba esnek.

Mind a kísérleti eredmények, mind pedig az elméleti modellek megmutatták, hogy habár egy mezoszkopikus minta nagyszámú atomot tartalmazhat, mégis a kvantumos interferencia jelenségek határozzák meg az elektromos és mágneses tulajdonságait. Abban az esetben, amikor egy makroszkopikus méretű, ohmikus vezetőt tekintünk, azt tapasztaljuk, hogy a vezetőképesség folytonosan növekszik a vezető szélességével. Ez a viselkedés teljes összhangban van az Ohm-törvénnyel. Azonban, egy kvantum drót vezetőképessége kvantált, nevezetesen, diszkrét "lépcsők" jelennek meg a vezetőképesség-kapufeszültség karakterisztikában [30, 31]. Ez az alapvető felfedezés gyakorlati alkalmazásokat is kínál, amikor egy makroszkopikus elektronikus eszközt miniatürizálunk, ami a fejlesztések általános iránya a félvezető elektronikában.

Munkám szorosan kapcsolódik a spin rendszerek kvantumelméletéhez. Spintronika (vagy spin elektronika), mely multidiszciplinárisnak is tekinthető, de a szilárdtestfizika egyik ígéretes szegmenseként is gondolhatunk rá. A kutatások célja ezen az ugrásszerűen fejlődő területen a spin szabadsági fok manipulálása és kontrollja különböző anyagi mintákban. A spintronika olyan alapvető fizikai jelenségekre koncentrál, mint a spin-polarizáció, a spin dinamika és a spin-polarizált transzport félvezetőkben és fémekben. A spin transzport abban különbözik az elektromos töltés transzporttól, hogy a spin nem megmaradó mennyiség a szilárdtestekben a spin-pálya csatolás és a hiperfinom felhasadás miatt [2, 100, 3].

A disszertáció témája az elektron transzport vizsgálata kétdimenziós nanostruktúrákban Rashba-féle spin-pálya kölcsönhatás [9] jelenlétében.

Kétdimenziós szuperrácsok tulajdonságai időben állandó spin-pálya kölcsönhatás jelenlétében

Olyan mesterséges kvázi-periodikus (kristályszerű) struktúrákat vizsgáltunk, amelyek képesek modulálni az elektromos áramot a Rashba spin-pálya csatolás miatt. Azt mondhatjuk, hogy a laterális szuperrácsok modellje egy spintronikus kristályt ír le. Ahogy azt megmutattuk, hogy az elektronok energiája és spinje kontrollálható ebben a kvázi-periodikus struktúrában a spintronikus kristály tulajdonságainak segítségével. Az elektronok viselkedését keskeny kvantum vezetékekben (amelyek építőelemei a szuperrácsoknak) egy megfelelő spinfüggő Hamilton-operátor határozza meg. Esetünkben a Rashba-féle spin-pálya kölcsönhatási tag, mint egy effektív, spinfüggő potenciál jelenik meg a Hamilton-operátorban. Ezek után meg kell keresnünk a rendszer sajátenergiáit és sajátállapotait. Egy adott energiához tartozó spinor értékű hullámfüggvény a sajátállapotok lineáris kombinációjaként áll elő a megfelelő hullámszámokkal. Megadtuk a valószínűségi áramsűrűség helyes alakját, amely megegyezik a megfelelő operátor (j_γ) várható értékével. Ennek segítségével leírható a spinfüggő áram a teljes rácsra nézve spin-pálya csatolás jelenlétében.

A szuperrácsot felépítő kvantum drótok csatlakozási pontokban kapcsolódnak össze, így alakul ki a nanorendszer geometriája, melyen szóródnak az elektronok. Ez azt jelenti, hogy a hullámfüggvényeknek teljesíteni kell a megfelelő határfeltételeket [80] minden csomópontban. Ha végtelen periodikus struktúrát tekintünk, akkor olyan speciális, szorzat alakú hullámokat keresünk, melyek rácsperiodikus függvényeket hordoznak. Ez teljes összhangban van a Bloch-tétellel. A végtelen rács sávszerkezete az előbb vázolt módszerrel meghatározható. Ezentúl megmutattuk, hogyan függ a sávséma a rács geometriai paraméteritől és a spin-pálya kölcsönhatás erősségétől [III.].

Gyakorlatilag, a határfeltételek a csatlakozási pontokban illesztési egyenletek formájában fejeződnek ki, melyek egy lineáris egyenletrendszert építenek fel. Ennek a megoldása szolgáltatja a reflektált és a transzmittált spinorok komponenseit egy adott bemenet esetén. Véges méretű hálózatokra használtuk a Landauer-Büttiker formalizmust abból a célból, hogy kiszámítsuk a vezetőképességet a transzmissziós együtthatókból. Megfigyeltük, hogy a nulla vezetőképességű tartományok helyzetei és kiterjedései érzékenyek a spin-pálya csatolás erősségének változtatására. Összehasonlítva a sávszerkezetet a véges rendszerek vezetési tulajdonságaival, azt találtuk, hogy már a viszonylag kisméretű blokkok esetén is tisztán megfigyelhetőek a tiltott sávok a vezetőképességben. Továbbá vizsgáltuk ezen rendszerek lehetséges spintronikai alkalmazásait különös tekintettel az energia sávszűrésre és a spin-polarizációs effektusokra [III.].

Kétdimenziós szuperrácsok vezetőképessége véges hőmérsékleten

A jelenkor kísérleti technikái megengedik, hogy különböző nanoméretű minták elektromos és mágneses tulajdonságait mérjük. Ezek készülhetnek például félvezető heterostruktúrákból [101]. Azonban nem hagyhatjuk figyelmen kívül a rendszerben uralkodó hőmérsékletet, ha a kvantumos jelenségeket kívánjuk tanulmányozni. Általánosságban, a termális fluktuációk is olyan mechanizmusok, melyek dekoherenciához vezetnek, azaz elfedik a kvantumos effektusokat.

Véges hőmérsékleten az elektronok transzportja nem modellezhető a Fermi-energiához tartozó monoenergiás állapotokkal. Ebben az esetben a bemenő és a kimenő spinorértékű hullámfüggvények leírását a sűrűségoperátorokkal tehetjük meg. Egyik fontos eredményünk, hogy a spin-pálya kölcsönhatás erősen befolyásolja a véges hőmérsékletű vezetőképességet, és ez az effektus magas hőmérsékletek esetén is érzékelhető marad. Tanulmányoztuk, hogy a koherenciát elrontó effektusok hogyan módosítják az előbbieket és azt kaptuk, hogy az állításunk igaz marad abban az esetben is, amikor a vezetőképesség erősen csökken a szórási folyamatok miatt [II.].

Az oszcilláló spin-pálya kölcsönhatással kapcsolatos jelenségek

A fő célkitűzésünk az volt, hogy feltárjuk a kvantumos transzportjelenségek alaptulajdonságait időfüggő Rashba típusú spin-pálya kölcsönhatás jelenlétében. Megjegyezzük, hogy az anyagi rendszerek kölcsönhatása valamilyen külső alternáló térrel a fizika különböző területein előkerülhet. Fontos példák: magas harmonikusok keltése lézertérrel atomi és molekuláris rendszerekben, transzportfolyamatok manipulálása külső, időfüggő kapufeszültséggel szilárdtestekben. Az általunk vizsgált kvantumrendszert egy időben periodikus Hamilton-operátor jellemezi. A probléma megoldásához a Floquet elmélet [65] nyújt alkalmas matematikai hátteret.

Olyan bemenő elektronokat tételeztünk fel, melyeket monoenergiás hullámfüggvények írnak le és az egyszerű poligon geometriákat felépítő kvantum drótokban mozoghatnak. Modellünknek egymódusú, egyenes kvantum vezetéket és háromszög alakú hurokgeometriát választottunk. A Hamilton-operátor időfüggése a spin-pálya csatolási tagon keresztül érvényesül. Így a probléma egy időfüggő Schrödinger-egyenlet megoldására vezet. Meghatároztuk a Floquet-féle kvázi-energiákat és a hozzájuk tartozó időfüggő, spinorértékű bázisállapotokat. Megmutattuk, hogy a reflektált és a transzmittált hullámfüggvényekben megjelennek az oszcilláló spin-pálya csatolás frekvenciájának egész számú többszörösei, a felharmonikusok. Munkánk során külön figyelmet szenteltünk a spin áramok és az idő szerint átlagolt transzport tulajdonságok vizsgálatának. A spin

iránya és az elektronsűrűség hullámszerű terjedést mutatnak azon tartományokban, ahol jelen van a spin-pálya csatolás, és ott is, ahol az elektronok szabadon terjedhetnek.

Megállapítottuk, hogy az ilyen egyszerű geometriák is képesek spin-polarizált hullámcsomagokat előállítani teljesen polarizálatlan bemenet esetén is. Ezen effektus kevéssé érzékeny a szóródási folyamatokból adódó dekoherenciára, így kísérleti megfigyelésre is lehetőségünk nyílhat [I.].

Hasonló effektusokat találtunk laterális szuperrácsokban is [IV.].

List of publications

Used for the dissertation:

[I.] **V. Szaszkó-Bogár**, P. Földi, F. M. Peeters,
Oscillating spin-orbit interaction as a source of spin-polarized wavepackets in two-terminal nanoscale devices,
J. Phys.: Cond. Matt. **26**, 135302 (2014).

[II.] P. Földi, **V. Szaszkó-Bogár**, F. M. Peeters,
High-temperature conductance of a two-dimensional superlattice controlled by spin-orbit interaction,
Phys. Rev. B **83**, 115313 (2011).

[III.] P. Földi, **V. Szaszkó-Bogár**, F. M. Peeters,
Spin-orbit interaction controlled properties of two-dimensional superlattices,
Phys. Rev. B **82**, 115302 (2010).

Additional work:

[IV.] **V. Szaszkó-Bogár**, F. M. Peeters, P. Földi,
Oscillating spin-orbit interaction in two-dimensional superlattices: sharp transmission resonances and time-dependent spin-polarized currents,
arXiv:1502.05798 [cond-mat.mes-hall] (2015).
(submitted to Physical Review B).

Acknowledgement

First of all, I would like to render thanks to my co-supervisor at the University of Szeged, Dr. Péter Földi for his guidance throughout my years as a PhD student at the University of Szeged. I also want to express my gratitude to my co-supervisor at the University of Antwerp, Prof. Dr. François M. Peeters for giving me the great opportunity of being part of the Condensed Matter Theory (CMT) Group at the University of Antwerp. I am thankful for their encouragement, constructive criticism and corrections, but particularly for their patience and continuous support.

The great and motivating atmosphere of the Department of Theoretical Physics has impressed me for several years. It is a pleasure for me to thank to all the members of the Department for their help and encouragement throughout the years. I will always remember the condensed matter theory lectures from Dr. György Papp. I think that these lectures and his character played an important role in the fact that my scientific interest has radically changed. I am grateful to Vera and Erika, our officers, for handling the paperwork with such an incredible efficiency and for the enjoyable talkings. I am much obliged to the CMT group for being a member of a professional research team.

I am very thankful for the measureless loveing and support of my lovely family. You always stand foremost in my heart and my soul as well. My parents, Mom and Dad, who showed me the real values of life as loving, steadiness, diligence and honour. You teached me that I should always fight for my dreams. There are nothing like whatever glitter and richness. My sister, Niki, although we have variant personality but I can not and do not want to wish a better sister than you. Thank you very much for being my sister. My wife, Bernadett, you always gave me huge incitement with limitless love and patience.

I thank to my friends for the unforgettable and gladsome moments through my years in Szeged.

My scientific work was supported by the Hungarian Scientific Research Fund (OTKA) under Contract No. T81364, the Flemish Science Foundation (FWO-V1), the Belgian Science Policy (AIP) as well as by the projects TÁMOP-4.2.2.A-11/1/KONV-2012-0060, TÁMOP-4.2.2/B-10/1-2010-0012 and TÁMOP-4.2.2.C-11/1/KONV-2012-0010 supported by the European Union and cofinanced by the European Social Fund.

Bibliography

[1] N. G. van Kampen, Statistical Physics, Proc. of Int. Conf. (1976).

[2] I. Žutić, J. Fabian, and S. D. Sarma, Rev. Mod. Phys. **76**, 323 (2004).

[3] D. D. Awschalom, D. Loss, and N. Samarth, *Semiconductor Spintronics and Quantum Computation* (Springer, Berlin, 2002).

[4] S. Datta and B. Das, Appl. Phys. Lett. **56**, 665 (1990).

[5] E. I. Rashba, Phys. Rev. B **62**, R16267 (2000).

[6] D. D. Awschalom and M. E. Flatté, Nat. Phys. **3**, 153 (2007).

[7] H. Ohno *et al.*, Appl. Phys. Lett. **69**, 363 (1996).

[8] M. I. D'Yakonov and V. I. Perel', Sov. Phys. JETP Lett. **13**, 467 (1971).

[9] E. I. Rashba, Sov. Phys. Solid State **2**, 1109 (1960).

[10] G. Dresselhaus, Phys. Rev. **100**, 580 (1955).

[11] P. Yu and M. Cardona, *Fundamentals of Semiconductors*, 4 ed. (Springer-Verlag, Berlin, 2010).

[12] E. O. Göbel *et al.*, Phys. Rev. Lett. **64**, 1801 (1990).

[13] K. Toyama, T. Nishioka, K. Sawano, Y. Shiraki, and T. Okamoto, Phys. Rev. Lett. **101**, 016805 (2008).

[14] B. E. A. Saleh and M. C. Teich, *Fundamentals of Photonics*, 2 ed. (Wiley, New York, 2007).

[15] T. Ihn, *Semiconductor Nanostructures* (Oxford University Press, New York, 2010).

[16] G. Thorgilsson, J. C. Egues, D. Loss, and S. I. Erlingsson, Phys. Rev. B **85**, 045306 (2012).

[17] Y. Aharonov and D. Bohm, Phys. Rev. **115**, 485 (1959).

[18] S. Datta and S. Bandyopadhyay, Phys. Rev. Lett. **58**, 717 (1987).

[19] Y. Aharonov and A. Casher, Phys. Rev. Lett. **53**, 319 (1984).

[20] S. Souma and B. K. Nikolić, Phys. Rev. B **70**, 195346 (2004).

[21] T. Bergsten, T. Kobayashi, Y. Sekine, and J. Nitta, Phys. Rev. Lett. **97**, 196803 (2006).

[22] B. H. Wu and J. C. Cao, Phys. Rev. B **75**, 113303 (2007).

[23] F. Nagasawa, J. Takagi, Y. Kunihashi, M. Kohda, and J. Nitta, Phys. Rev. Lett. **108**, 086801 (2012).

[24] F. Nagasawa, D. Frustaglia, H. Saarikoski, K. Richter, and J. Nitta, Nature Comm. **4** (2013).

[25] M. Governale, Phys. Rev. Lett. **89**, 206802 (2002).

[26] R. Landauer, IBM J. Res. and Dev. **1**, 223 (1957).

[27] M. Büttiker, Y. Imry, R. Landauer, and S. Pinhas, Phys. Rev. B **31**, 6207 (1985).

[28] S. Datta, *Electronic transport in mesoscopic systems* (Cambridge University Press, Cambridge, 1995).

[29] K. v. Klitzing, G. Dorda, and M. Pepper, Phys. Rev. Lett. **45**, 494 (1980).

[30] B. J. van Wees *et al.*, Phys. Rev. Lett. **60**, 848 (1988).

[31] D. A. Wharam *et al.*, J. Phys. C: Solid State Physics **21**, L209 (1988).

[32] D. K. Ferry, S. M. Goodnick, and J. Bird, *Transport in Nanostructures*, 2 ed. (Cambridge University Press, Cambridge, 2009).

[33] K. J. Thomas *et al.*, Phys. Rev. Lett. **77**, 135 (1996).

[34] O. Kálmán, *Quantum Interference in Semiconductor Rings*, PhD thesis, University of Szeged, 2009.

[35] D. Bercioux, Spin-orbit interactions in semiconductor nanostructures, `http://tfp1.physik.uni-freiburg.de/teaching/Nanoelectronics/`.

[36] W. Walukiewicz, H. E. Ruda, J. Lagowski, and H. C. Gatos, Phys. Rev. B **30**, 4571 (1984).

[37] J. Sólyom, *A modern szilárdtestfizika alapjai* (ELTE Eötvös kiadó, Budapest, 2003).

[38] Y. Murayama, *Mesoscopic Systems: Fundamentals and Applications* (Wiley-VCH, New York, 2001).

[39] G. H. Wannier, Phys. Rev. **52**, 191 (1937).

[40] R. Peierls, Z. Phys. **80** (1933).

[41] D. R. Hofstadter, Phys. Rev. B **14**, 2239 (1976).

[42] K. Jiménez-García *et al.*, Phys. Rev. Lett. **108**, 225303 (2012).

[43] J. Kong *et al.*, Phys. Rev. Lett. **87**, 106801 (2001).

[44] C. C. Eugster and J. A. del Alamo, Phys. Rev. Lett. **67**, 3586 (1991).

[45] C. Cohen-Tannoudji, B. Diu, and F. Laloë*Quantum Mechanics* Vol. 1, 2 ed. (Wiley, New York, 1977).

[46] M. Abramowitz and I. Stegun, editors, *Handbook of mathematical functions* (Dover Publications, New York, 1965).

[47] S. A. Sequoia, G. E. Stillman, and C. M. Wolfe, Thin Solid Films **31** (1976).

[48] P. A. M. Dirac, *The principles of quantum mechanics.*, 4 ed. (Clarendon Press, Oxford, 1989).

[49] W. Pauli, *General Principles of Quantum Mechanics* (Springer-Verlag, Berlin, Heidelberg, New York, 1980).

[50] A. S. Davydov, *Quantum Mechanics* (Pergamon Press, Oxford, 1965).

[51] W. Pauli, Zeitschrift für Physik **43**, 601 (1927).

[52] V. B. Berestetskii, E. M. Lifshitz, and L. P. Pitaevskii, *Quantum Electrodynamics*, 2 ed. (Pergamon Press, Oxford, London, New York, Edinburgh, Paris, Frankfurt, 1982).

[53] R. Winkler, *Spin-Orbit Coupling Effects in Two-Dimensional Electron and Hole Systems* (Springer-Verlag, Berlin Heidelberg, 2003).

[54] Y. A. Bychkov and E. I. Rashba, J. Phys. C: Solid State Phys. **17**, 6039 (1984).

[55] Y. A. Bychkov and E. I. Rashba, JETP Lett. **39**, 78 (1984).

[56] E. A. de Andrada e Silva, G. C. L. Rocca, and F. Bassani, Phys. Rev. B **55**, 16293 (1997).

[57] X. Zhang, Q. Liu, J.-W. Luo, A. J. Freeman, and A. Zunger, Nature Phys. **10**, 387 (2014).

[58] B. Partoens, Nature Phys. **10** (2014).

[59] J. Nitta, T. Akazaki, H. Takayanagi, and T. Enoki, Phys. Rev. Lett. **78**, 1335 (1997).

[60] D. Grundler, Phys. Rev. Lett. **84**, 6074 (2000).

[61] J. L. Cheng, M. W. Wu, and I. C. da Cunha Lima, Phys. Rev. B **75**, 205328 (2007).

[62] S. D. Ganichev *et al.*, Phys. Rev. Lett. **92**, 256601 (2004).

[63] B. H. Bransden and C. J. Joachain, *Quantum Mechanics*, 2 ed. (Pearson, New York, 2000).

[64] L. D. Landau and E. M. Lifshitz, *Quantum Mechanics, Nonrelativistic Theory* (Pergamon Press, Oxford, 1965).

[65] G. Floquet, Ann. École Norm. Sup. **12**, 46 (1883).

[66] F. J. Dyson, Phys. Rev. **75**, 486 (1949).

[67] T. Koga, J. Nitta, T. Akazaki, and H. Takayanagi, Phys. Rev. Lett. **89**, 046801 (2002).

[68] M. König *et al.*, Phys. Rev. Lett. **96**, 076804 (2006).

[69] J. Nitta, T. Akazaki, H. Takayanagi, and T. Enoki, Phys. Rev. Lett. **78**, 1335 (1997).

[70] Z. Zhu, Y. Wang, K. Xia, X. Xie, and Z. Ma, Phys. Rev. B **76**, 125311 (2007).

[71] O. Kálmán, P. Földi, M. G. Benedict, and F. M. Peeters, Physica E **40**, 567 (2008).

[72] O. Kálmán, T. Kiss, and P. Földi, Phys. Rev. B **80**, 035327 (2009).

[73] P. Földi, O. Kálmán, M. G. Benedict, and F. M. Peeters, Nano. Lett. **8**, 2556 (2008).

[74] D. Bercioux, M. Governale, V. Cataudella, and V. Ramaglia, Phys. Rev. B **72**, 075305 (2005).

[75] M. Kohda *et al.*, Nature Comm. **3** (2012).

[76] L. W. Molenkamp, G. Schmidt, and G. E. W. Bauer, Phys. Rev. B **64**, 121202 (2001).

[77] C. Kittel, *Introduction to solid state physics*, 8 ed. (Wiley, New York, 2005).

[78] P. Földi, V. Szaszkó-Bogár, and F. M. Peeters, Phys. Rev. B **82**, 115302 (2010).

[79] F. E. Meijer, A. F. Morpurgo, and T. M. Klapwijk, Phys. Rev. B **66**, 033107 (2002).

[80] S. Griffith, Trans. Faraday Soc. **49**, 345 (1953).

[81] C. Kittel, *Quantum Theory of Solids*, 2 ed. (Wiley, New York, 1987).

[82] U. Aeberhard, Phys. Rev. B **87**, 081302 (2013).

[83] J. Nitta, T. Akazaki, H. Takayanagi, and K. Arai, Phys. Rev. B **46**, 14286 (1992).

[84] O. Kálmán, P. Földi, M. G. Benedict, and F. M. Peeters, Phys. Rev. B **78**, 125306 (2008).

[85] P. Földi, O. Kálmán, and F. M. Peeters, Phys. Rev. B **80**, 125324 (2009).

[86] P. Földi, V. Szaszkó-Bogár, and F. M. Peeters, Phys. Rev. B **83**, 115313 (2011).

[87] S. I. Chu and D. A. Telnov, Phys. Rep. **390**, 1 (2004).

[88] H. Rabitz, R. de Vivie-Riedle, M. Motzkus, and K. Kompa, Science **288**, 824 (2000).

[89] M. P. Nowak, B. Szafran, and F. M. Peeters, Phys. Rev. B **86**, 125428 (2012).

[90] W. Li and L. E. Reichl, Phys. Rev. B **60**, 15732 (1999).

[91] M. J. van Veenhuizen, T. Koga, and J. Nitta, Phys. Rev. B **73**, 235315 (2006).

[92] T. Koga, Y. Sekine, and J. Nitta, Phys. Rev. B **74**, 041302 (2006).

[93] T. Koga, J. Nitta, and M. J. van Veenhuizen, Phys. Rev. B **70**, 161302 (2004).

[94] D. Bercioux, D. Frustaglia, and M. Governale, Phys. Rev. B **72**, 113310 (2005).

[95] V. Szaszkó-Bogár, P. Földi, and F. M. Peeters, J. Phys.: Cond. Matt. **26**, 135302 (2014).

[96] B. Molnár, F. M. Peeters, and P. Vasilopoulos, Phys. Rev. B **69**, 155335 (2004).

[97] A. A. Kiselev and K. W. Kim, Phys. Rev. B **71**, 153315 (2005).

[98] P. Földi, B. Molnár, M. G. Benedict, and F. M. Peeters, Phys. Rev. B **71**, 033309 (2005).

[99] T. Koga, J. Nitta, and M. van Veenhuizen, Phys. Rev. B **70**, 161302(R) (2004).

[100] A. Fert, Rev. Mod. Phys. **80**, 1517 (2008).

[101] X. R. Li *et al.*, J. Appl. Phys. **116**, 223701 (2014).